Fabrication of Graphene via Catalytic Graphitisation of Solid Carbon Sources

A Thesis Submitted to

The University of Manchester

For the degree of

Doctor of Philosophy

In the Faculty of Science and Engineering

2021

Zhiying Xin

School of Natural Sciences

Department of Material

List of contents

List of figures

List of Tables

List of Abbreviations

2D	2-dimensional
3D	3-dimensional
AFM	Atomic force microscopy
BE	Binding energy
BET	Brunauer-Emmett-Teller
BJH	Barrett-Joyner-Halenda
CVD	Chemical vapour deposition
DFT	Density functional theory
DMF	N,N-dimethylformamide
EDS	Energy dispersive X-ray spectroscopy
FTIR	Fourier-transform infrared spectroscopy
GO	Graphene oxide
HOPG	Highly oriented pyrolytic graphite
ISO	International Organization of Standardization
KBr	Potassium bromide
KE	Kinetic energy
LFP	Lithium iron phosphate
LIG	Laser-induced graphene
LPE	Liquid-phase exfoliation
MMA	Methyl methacrylate
Mpa	Megapascal
NBD	4-nitrobenzene-diazonium-tetrafluoroborate
NMP	N-methyl-2-pyrrolidinone
NPL	National Physical Laboratory

ODCB	Ortho-dichlorobenzene
PAN	Polyacrylonitrile
PECVD	Plasma-enhanced chemical vapour deposition
PMMA	Poly(methyl methacrylate)
PTFE	Polytetrafluoroethylene
rGO	Reduced graphene oxide
rpm	Revolutions per minute
sccm	Standard cubic centimetres per minute
SEM	Scanning electron microscope
STM	Scanning tunnelling microscope
TEM	Transmission electron microscope
Tg	Glass transition temperature
XPS	X-ray photoelectron spectroscopy
XRD	X-ray diffraction

List of Symbols

q	Heating/cooling rate
Δh*	Activation enthalpy
R	Universal gas constant
n	Whole number
λ	Wavelength of incident X-ray
d	Lattice spacing
θ	Angle between crystal plane and incident X-ray
h	Planck's constant
ν	Frequency of incident photons
ϕ	Work function of instrument
V_a	Absorbed gas volume under standard conditions
P/P_0	Relative pressure of the adsorbate gas
V_m	Volume of gas needed to cover all solid surfaces
C	Dimensionless constant

Abstract

This work has suggested two feasible routes for both 2-dimensional (2D) and 3-dimensional (3D) graphene fabrications on the basis of catalytic graphitisation of solid carbon sources, with proposed mechanisms.

Graphene growth with ferric chloride ($FeCl_3$) and glucose ($C_6H_{12}O_6$) was explored in aspects of uniform liquid layer formation, appropriate heat treatment methods and sufficient sample cleaning. The 2D graphene on silicon (Si) wafer, as well as foam-structured 3D graphene, were both obtained through straightforward heat treatment of $FeCl_3$ and glucose mixture at a low temperature of 750 °C. The graphene produced was further characterised by its morphological and chemical properties. Crystal structure and structural information were also obtained with X-ray diffraction (XRD) and Raman spectroscopy. Graphene synthesised through this route has comparable defect density with typical graphene oxide (rGO) products. The defect formation mechanism was studied and proposed with regard to a possible excess of carbon source in the material.

To avoid forming excessive graphene layers, $FeCl_3$ was replaced by copper (Cu) particles in pursuit of self-limited growth. The solid carbon source was changed to Polyacrylonitrile (PAN) since it can be pre-oxidised to a more rigid form and protect 3D graphene foam from collapse by enhancing its structural strength and toughness. Interconnected 3D mesoporous graphene foam consisting of 7-8 graphene layers and a large specific surface area of 610 m^2/g was successfully synthesised. X-ray photoelectron spectroscopy (XPS) results confirmed the transformation of sp^3 C to sp^2 C. The defects detected via Raman spectroscopy are believed to be related to the nano-sized domain observed in between graphene 'patches'. A correspondent 3D graphene domain developing mechanism was proposed, which hopefully will give an insight into graphene growth on 3D 'Cu-system' substrates.

Declaration

No portion of the work referred to in the thesis has been submitted in support of an application for another degree or qualification of this or any other university or other institute of learning.

Copyright Statement

i) The author of this thesis (including any appendices and/or schedules to this thesis) owns certain copyright or related rights in it (the “Copyright”) and s/he has given The University of Manchester certain rights to use such Copyright, including for administrative purposes.

ii) Copies of this thesis, either in full or in extracts and whether in hard or electronic copy, may be made only in accordance with the Copyright, Designs and Patents Act 1988 (as amended) and regulations issued under it or, where appropriate, in accordance with licensing agreements which the University has from time to time. This page must form part of any such copies made.

iii) The ownership of certain Copyright, patents, designs, trademarks and other intellectual property (the “Intellectual Property”) and any reproductions of copyright works in the thesis, for example graphs and tables (“Reproductions”), which may be described in this thesis, may not be owned by the author and may be owned by third parties. Such Intellectual Property and Reproductions cannot and must not be made available for use without the prior written permission of the owner(s) of the relevant Intellectual Property and/or Reproductions.

iv) Further information on the conditions under which disclosure, publication and commercialisation of this thesis, the Copyright and any Intellectual Property and/or Reproductions described in it may take place is available in the University IP Policy (see http://documents.manchester.ac.uk/DocuInfo.aspx?DocID=24420), in any relevant Thesis restriction declarations deposited in the University Library, The University Library’s regulations (see http://www.library.manchester.ac.uk/about/regulations/) and in The

University’s policy on Presentation of Theses.

http://www.library.manchester.ac.uk/about/regulations/) and in The University’s policy on Presentation of Theses

Acknowledgements

First, I would like to express my sincere gratitude to my supervisors Dr. Jiashen Li and Professor Ping Xiao, who have always been supportive, patient and encouraging throughout my 4.5 years of study. I'd like to thank them both for offering me the opportunity to begin my study at the University of Manchester. Also, the constructive comments and invaluable advice they provided will always be valued.

Second, I would like to thank my friends and colleagues Dr. Lijing Lin, Jie Sun, Jinmin Meng, Zihan Lu, Yangyang Fan, Jinxin Yang, Niting Zeng, Hui Ding, Dr. Kewen Pan, Muhammad Tauseef and Muhammad Umar, who had made my PhD life more enjoyable and colourful. There are also some doctor-to-bes in this list, I sincerely wish them all the best.

I also appreciate Dr. Teruo Hashimoto, Dr. Duc-The Ngo and Mr. Matthew Smith for always being helpful and patient when I needed technical assistance on those intricate equipment for materials characterisations. Special thanks to Mr. David Strong, who, for me, had been a difficult person to work with at the beginning stage of my work. But later, I found that he is actually a very nice and reasonable guy, who is always ready to help us out.

I am extremely grateful to my close friend Ying Lu, who has been keeping me company, always, through my highs and lows. Good luck with your thesis too! And also, Dr. Qinmeng Luan, has been not only a good friend but also an inspiration in my life. You are talented and beautiful. Be confident in yourself!

Finally, I would like to express my love and gratitude towards my mom, Ying Huang, and all my family members. They have taught me the power and meaning of unconditional love and made me the person I am today.

Chapter 1 Introduction

1.1 Research background

The design and fabrication of graphene-based materials have attracted extensive attention among materials scientists and physicists. Different strategies have been adopted to achieve high-performance graphene with economic friendly procedures.

According to global graphene market report, a market size of 78.7 million U.S. dollars was estimated in 2019 [1]. This value is still expected to increase. On the one hand, researchers are fascinated by graphene's extraordinary mechanical [2], thermal [3], electrical [4] and electronic [5] properties. On the other hand, they are often refrained from fully exploiting this material by its low yield and low scalability. Moreover, the fabrication of graphene should not be developed at the expense of the environment. The key challenge is balancing various factors and finding a feasible way to produce high-quality graphene with relatively low cost and eco-friendly raw materials.

In a roadmap for graphene [6], Chemical vapour deposition (CVD) was rated one of the cheapest methods to produce graphene of competitive quality. Sun's group [7] took a step further and replaced the gaseous reactant involved in CVD with a solid-state polymer, Poly(methyl methacrylate) (PMMA). With deliberate control of the reaction conditions, high-quality single-layer graphene was successfully synthesised. That has opened the door for a whole wide range of polymers. Graphene fabrication methods based on biomass [8, 9] and waste materials [10, 11] have been increasingly investigated since then. Apart from the non-polluting carbon sources, by-products of such reactions are also mostly environment-friendly.

Considering all these factors, graphene fabrication from green solid carbon sources was chosen to be the main subject of our study. And in this project, two different types of graphene growth mechanisms utilizing different types of carbon sources and metal

catalysts were explored.

1.2 Aim and objectives

The overall aim of this research is to fabricate high-quality graphene in a simple and inexpensive way with a good combination of appropriate starting materials and suitable treatment. The mechanisms behind the reactions involved in graphene growth are also to be studied.

There has been no globally agreed standard for graphene yet. Therefore, graphene products of various thicknesses and levels of disorders can be found in the market.

In March 2021, the National Physical Laboratory (NPL), in collaboration with the International Organization of Standardization (ISO), released ISO/TS 21356-1:2021, in which the definition and structural properties of graphene are specified [12]. Based on this standard and the general experimental results published in related researches, 'high-quality graphene' in this study will mainly be regarded as 2D material with one to ten stacked graphene layers and a low level of disorder (Raman peak intensity ratio I_D/I_G <1).

Objectives are:

i) Finding suitable starting materials for graphene synthesis

There are plenty of solid carbon sources and metal or metal salt catalysts available as the starting materials for graphene synthesis. Among these, materials that are cheap, non-hazardous, and with easy access are preferred.

Solvents may also be involved. Therefore, the solubility, viscosity, as well as chemical properties of these solvents should all be taken into consideration in this case.

ii) Investigating the factors that may affect the reactions

The whole process of 2D/3D graphene synthesis involves several stages. And in each stage, usually, more than one parameter can be altered and adjusted. Each may affect the reaction and thus affect the quality of the graphene produced. The factors can be: 1) metal to carbon ratio; 2) temperature and time for heat treatment; 3) gas flow rate; 4) heating and cooling rate, etc.

iii) Producing 2D/3D graphene from a solid carbon source

After determining factors that affect the reactions and determining proper parameter values, the next task is to grow a homogeneous, high-quality, low-vacancy 2D graphene sheet on silicon wafers or on other substrates. Meanwhile, grow 3D graphene foams with the aid of low-cost pore formers such as sodium chloride.

iv) Studying the mechanisms of the reactions

The mechanisms that need to be studied are: pyrolysis of carbon sources; reduction of metal salts with the presence of reducing gas and carbon; dissolution and precipitation of carbon on the surface of the metal; nucleation of graphene nano-islands, and the coalescence of graphene domains.

v) Optimising the process

After the entire graphene fabrication process is fully understood and controlled, try to improve the efficiency while reducing the cost of fabrication by using cheaper chemicals, lower reacting temperatures and shorter reacting time.

1.3 Thesis layout

This thesis begins with a brief introduction to the research background, followed by an illustrated aim and objectives of the work in Chapter 1.

Chapter 2 is a review of literature which is divided into three parts: 1) Basic knowledge about graphene's history, material structure and its extraordinary properties; 2) popular graphene fabrication techniques demonstrated in detail; and 3) graphene synthesis approaches, based explicitly on catalytic graphitisation of solid carbon sources.

Chapter 3 first introduces all the materials used in the experiment, followed by an illustration of material characterisation methods adopted in terms of their working principles, applications and how the techniques are utilised in this work.

Chapter 4 introduces the first graphene fabrication route adopted in this study. Different processes and procedures are followed in 2D graphene synthesis and 3D graphene synthesis. The fabrication and characterisation routes are demonstrated step by step. The results and findings are discussed at the end of this chapter. A conclusion and proposed mechanism are also given at the end.

Chapter 5 begins with an evaluation of the findings and problems raised in the previous study. Adjustments are made accordingly, followed by another step by step introduction of the second graphene fabrication route. Results from various materials characterisations are presented and discussed, followed by a proposed mechanism and conclusion of this new route.

A conclusion of this whole thesis and work is given in the last chapter. Future work for this study is also proposed.

References

[1] Size, G. M., 2020. Share & Trends Analysis Report By Application (Electronics, Composites, Energy), By Product (Graphene Nanoplatelets, Graphene Oxide), By Region, And Segment Forecasts, 2020–2027. *Accesed from https://www. grandviewresearch. com/industry-analysis/graphene-industry#:~: text= The% 20global% 20graphene% 20market% 20s ize, to% 20drive% 20the% 20product% 20demand. On*, *28*.

[2] Lee, C., Wei, X., Kysar, J. W., & Hone, J., 2008. Measurement of the elastic properties and intrinsic strength of monolayer graphene. *Science*, *321*(5887), 385-388.

[3] Balandin, A. A., Ghosh, S., Bao, W., Calizo, I., Teweldebrhan, D., Miao, F., & Lau, C. N., 2008. Superior thermal conductivity of single-layer graphene. *Nano Letters*, *8*(3), 902-907.

[4] Chen, J. H., Jang, C., Xiao, S., Ishigami, M., & Fuhrer, M. S., 2008. Intrinsic and extrinsic performance limits of graphene devices on SiO 2. *Nature Nanotechnology*, *3*(4), 206-209.

[5] Rudrapati, R., 2020. Graphene: Fabrication Methods, Properties, and Applications in Modern Industries. In *Graphene Production and Application*. IntechOpen.

[6] Novoselov, K. S., Fal, V. I., Colombo, L., Gellert, P. R., Schwab, M. G., & Kim, K., 2012. A roadmap for graphene. *Nature*, *490*(7419), 192-200.

[7] Sun, Z., Yan, Z., Yao, J., Beitler, E., Zhu, Y., & Tour, J. M., 2010. Growth of graphene from solid carbon sources. *Nature*, *468*(7323), 549-552.

[8] Sun, L., Tian, C., Li, M., Meng, X., Wang, L., Wang, R., ... & Fu, H., 2013. From coconut shell to porous graphene-like nanosheets for high-power supercapacitors. *Journal of Materials Chemistry A*, *1*(21), 6462-6470.

[9] Primo, A., Atienzar, P., Sanchez, E., Delgado, J. M., & García, H., 2012. From biomass wastes to large-area, high-quality, N-doped graphene: catalyst-free carbonization of chitosan coatings on arbitrary substrates. *Chemical Communications*, *48*(74), 9254-9256.

[10] Ruan, G., Sun, Z., Peng, Z., & Tour, J. M., 2011. Growth of graphene from food, insects, and waste. *ACS Nano*, *5*(9), 7601-7607.

[11] Zhou, H., Zhang, J., Amiinu, I. S., Zhang, C., Liu, X., Tu, W., ... & Mu, S., 2016. Transforming waste biomass with an intrinsically porous network structure into porous nitrogen-doped graphene for highly efficient oxygen reduction. *Physical Chemistry Chemical Physics*, *18*(15), 10392-10399.

[12] ISO. 2021. ISO/TS 21356-1:2021 Nanotechnologies — Structural characterization of graphene — Part 1: Graphene from powders and dispersions. [online] Available at: <https://www.iso.org/standard/70757.html>

Chapter 2 Literature Review

This review can mainly be divided into two sections: fundamentals of graphene are introduced in Section 2.1. Synthesis approaches that have been developed to fabricate 2D and 3D graphene are demonstrated in detail and compared in Section 2.2 and Section 2.3, respectively.

In the first section, the inspiring story of graphene's discovery is told in chronological order, with an introduction to the famous debate upon graphene's existence. The unique structure of graphene is then reviewed in answering the question raised in Section 2.1.1. Unique properties of graphene and graphene's performance in practical use are also introduced.

Section 2.2 begins with an overview of the most popular techniques for graphene production. The principles behind these techniques are explained and compared. Since most techniques are developed for 2D graphene production, in Section 2.2.2, 3D graphene fabrication is specifically reviewed.

The last part of this literature review focuses on the understanding of catalytic graphitisation on the basis of well-established mechanisms in CVD graphene growth. How the techniques developed for 2D graphene synthesis are adapted for the fabrication of 3D graphene is also demonstrated, followed by a summary of key factors to consider when fabricating graphene.

2.1 Introduction to graphene

2.1.1 History of graphene

Graphene was first successfully isolated by Professor A.K. Geim and K.S. Novoselov using a technique now known as the 'scotch tape method' at the University of Manchester in 2004 [1]. However, the first discussion of graphene and predictions of its properties on a theoretical level can be traced back to the 1930s.

Graphene has already been utilized as the basic unit for graphite and nanotubes when carrying out theoretical calculations for a long time. In 1934, R.E. Peierls [2] and L.D. Landau [3] pointed out that 2D crystals should not exist under normal pressure and temperature due to their thermodynamic instability. Many scientists back then believed graphene is more of a conceptual structure than a material that exists in the real world. Nevertheless, it has never hindered physicists' investigation of this conceptual material.

Twenty years later, Nobel Prize winner L.C. Pauling proposed that single-layer graphene should be an insulator because of the strong electron-electron interactions [4]. However, around the same time, P. R. Wallace published his findings in the band theory of graphite, stating that electrical conductivity parallel to graphite's carbon plane is about 100 times greater than that across the planes [5]. And Wallace's theory was based on an opposite assumption to Peirels and Landau’s, where electron-electron interaction was not taken into account at all.

N.D. Mermin and H.A. Wagner established the Mermin-Wagner theorem in 1966 [6]. Like Peierl and Landau, Mermin also questioned crystals' existence in less than three dimensions over long ranges by stating that long-wave density fluctuations will grow logarithmically in 2D systems and destroy the crystalline order over long ranges [7].

In a word, although graphene was no stranger to theoretical physicists and materials scientists as its conductivity and existence have been controversial topics widely discussed in the 20th century, not many of them were pinning their hopes on this material.

Meanwhile, not liking to be bound by theory, experimental physicists were inching closer to discovering graphene from various angles.

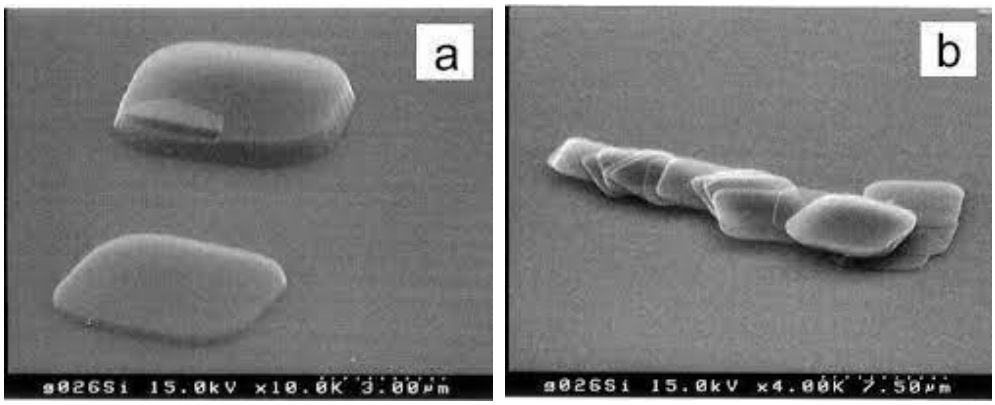

Figure 2.1. SEM images of graphite plates transferred onto Si(001) substrate. a) A HOPG island with an original height of 6 µm. b) The graphite island was then delaminated into several thinner flakes in the process of transfer through rubbing [8].

In 1999, X. Lu published a paper on tailoring graphite through oxygen plasma etching to get thin plates of graphite as building blocks for carbon nanotubes [8]. When they transferred the graphite islands to other substrates, it was done by rubbing the surface of highly oriented pyrolytic graphite (HOPG) against the target substrate's surface since they believed graphite could easily be cleaved along its basal planes (**Figure 2.1**). The paper even suggested that with more extensive rubbing of the graphite surface against other flat surfaces, it might be possible to achieve multiple or single atomic layers of graphite plates. However, Lu did not carry out further checks for his thought.

Also, in the process of manipulating the geometry of graphite sheets so as to control their properties, T. W. Ebbesen and H. Hiura managed to visualize a 'few-nm-thick'

tearing of graphitic sheet on a surface of HOPG through atomic force microscopy (AFM) [9].

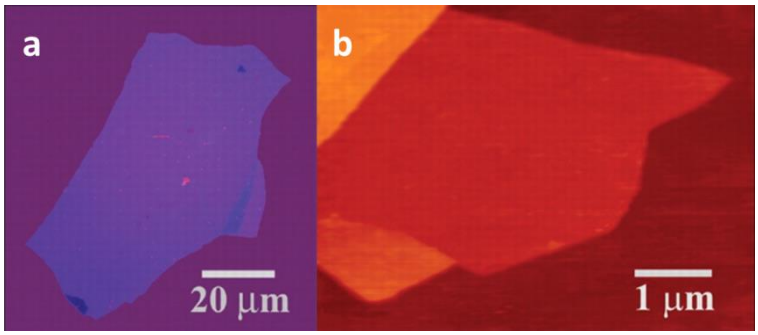

Figure 2.2. a) Image of a few-layer graphene flake (~3 nm thick) taken by an optical microscope. b) Image of single-layer graphene (central area) mixed with multi-layer graphene (upper left corner and lower-left corner) obtained through AFM [1].

Before Geim successfully isolated graphene, he had tried a lot of advanced instruments and methods, but none of them had been as effective. Unexpectedly, the so-called "mechanical exfoliation method", which finally realized his dream, is simply to peel the surface of HOPG off with a widely used Scotch tape repeatedly until single-layer graphene is achieved [1]. At the time, Scotch tape was the most effective and simplest tool for cleaning and collecting graphite scraps. Geim and Novoselov applied it to the body of graphite crystal, and after a few trials, in a mass of graphite fragments they peeled off, graphene was found [10]. In the video they later uploaded to demonstrate this method, colourful graphene sheets with different thicknesses can be observed under an optical microscope after being transferred from the tape to a silicon substrate (**Figure 2.2**).

If you rub two pieces of graphite against each other or rub a piece of graphite with any layer-structured crystal, you might as well find some single-layer graphene among the scraps [11]. Just as Geim addressed in his review of graphene's prehistory [12], 'graphene has literally been before our eyes and under our noses for many centuries but was never recognized for what it really is.' And today, graphene has already been

made visible under a magnifying glass as the mechanical exfoliation method can currently produce defect-free graphene with a lateral size up to 1 mm [13].

Geim also acknowledged some early work from the 1970s on few-layer graphite at the Nobel Prize award ceremony in 2010. Even if the discovery of graphene seemed accidental, the success was not instant. It was an inevitable product of a series of scientific inquiries.

2.1.2 Structure of Graphene

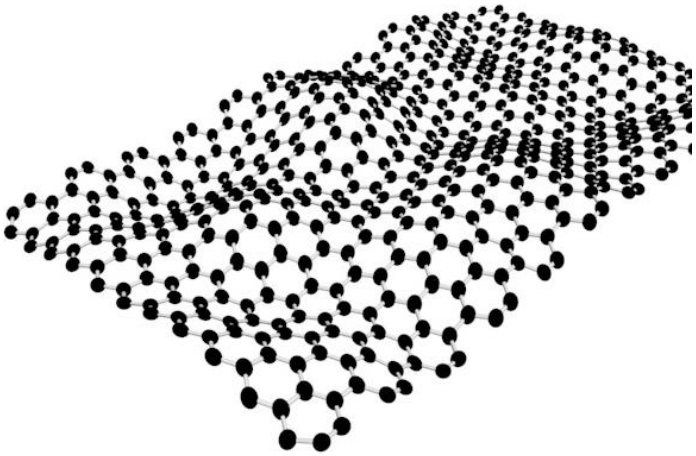

Figure 2.3. Schematic model of a single-layer graphene sheet.

The structure of a 'perfect' graphene sheet entirely made up of hexagonal units is illustrated in **Figure 2.3**. In essence, graphene refers to a single-layer graphite sheet with only one atom thick (~0.335nm [14]).

The sp^2 hybridized carbon atoms are closely packed in a honeycomb-structured plane. Each carbon atom is bonded to 3 adjacent carbon atoms via δ bonds resulting from the overlap of sp hybrid orbitals [15]. These strong covalent bonds have a short interatomic length of 0.142nm, which can effectively reinforce graphene's hexagon structure [4].

On the other hand, the weaker π bonds perpendicular to the plane are conjugated to form valence and conduction bands. As is illustrated in **Figure 2.4**, valence and conduction bands touch at the first Brillouin zone boundary, where the atoms are located. Therefore, the π electrons are delocalized and free to move from one edge to the other. That has given rise to some of graphene's peculiar electronic properties [16].

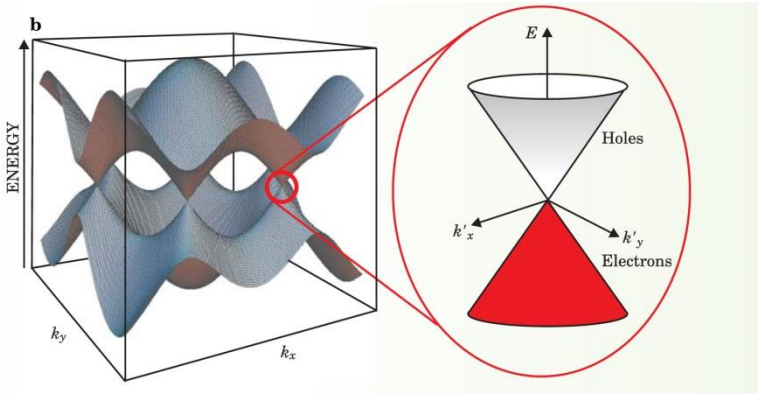

Figure 2.4. Three-dimensional band structure of graphene [15].

As previously mentioned, many theorems proposed by theoretical physicists seem to be against the existence of such 2D materials. Then how could we still manage to isolate graphene sheets?

With regard to Peirels and Mermin's theorems, their arguments about the logarithmically growing displacements of atoms over long ranges have been proved to be valid by experiments. But the consequent hypothesis that any 2D crystals would quickly fall apart did not apply to graphene in practice. In the case of graphene, the effect of thermal fluctuation can be counterbalanced by minuscule rippling, wrinkling or crumpling. As the images in **Figure 2.5** present, the graphene sheet is not entirely flat. In fact, the existence of these ripples, wrinkles and crumples can effectively protect graphene from decomposing and is always observed.

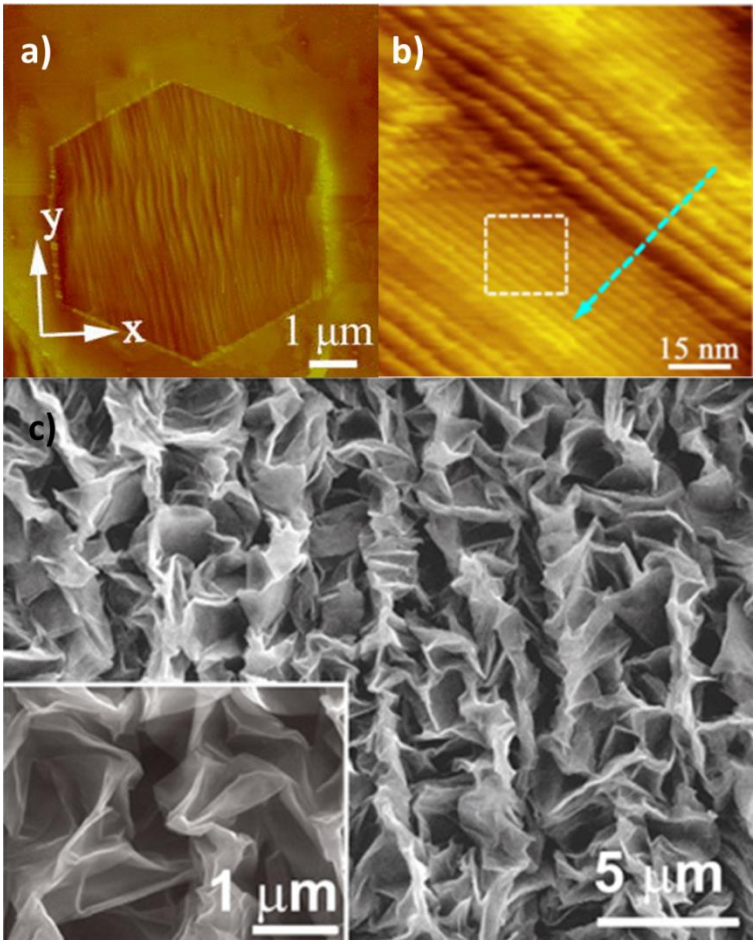

Figure 2.5. a) AFM image of a wrinkled hexagonal graphene flake grown on Cu surface by CVD [17]. b) Scanning tunnelling microscope (STM) image of periodic nanoripples in a graphene monolayer grown on Cu surface [18]. c) Scanning electron microscope (SEM) image of crumples formed at the surface of a deformed single-layer graphene flake [19].

Sir A.K. Geim and Sir K.S. Novoselov also proposed that since graphene can be wrapped into 0-dimensional buckyballs, rolled into 1-dimensional nanotubes and stacked into 3-dimensional graphite, graphene can be regarded as a basic unit for building graphitic materials of all other dimensionalities [20].

2.1.3 Properties of Graphene

2.1.3.1 Chemical properties

Structural distortions [21] or chemical defects [22] are essential to chemical modifications of graphene since flat defect-free graphene is inert. Reactions with various functional groups (most commonly with oxygen and nitrogen [23-25]) will take place favourably at irregular sites such as the surface near winkles, defects and edges.

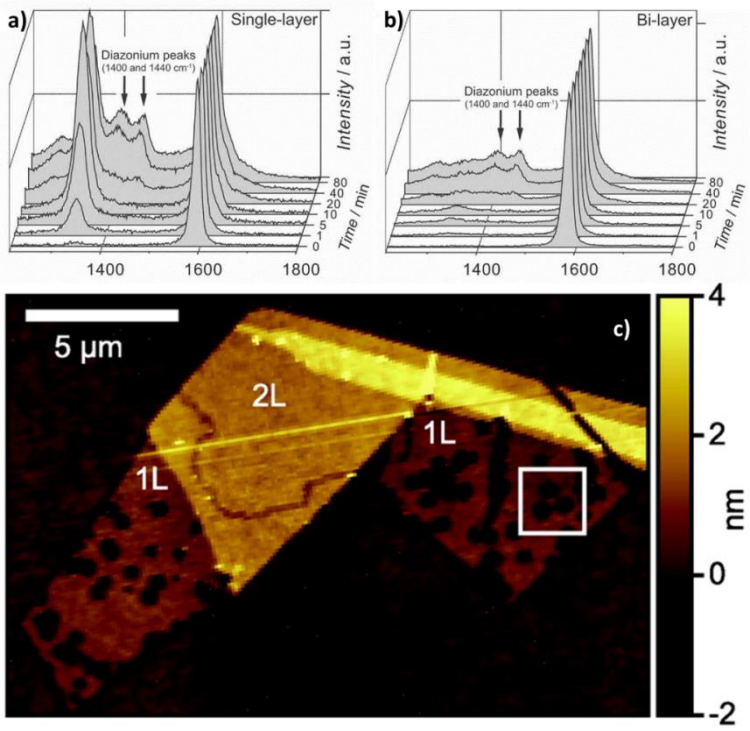

Figure 2.6. Raman spectra of functionalized a) single-layer graphene and b) bi-layer graphene respectively over time [26]. After being immersed in 4-nitrobenzene-diazonium-tetrafluoroborate (NBD) for around 5 minutes, diazonium peaks started to show up in the spectrum of single-layer graphene. Moreover, it took ten times longer for the peaks to show up in the spectrum of bi-layer graphene. c) AFM image of a folded graphene sheet after 10 min of hydrogen plasma treatment. The overlapped (bi-layer) region was relatively intact compared with the uncovered (single-layer) region [27].

Studies also found that compared with bi-layer or few-layer graphene, single-layer graphene exhibited a significantly higher reactivity [26-28]. In **Figure 2.6**, both the

Raman spectra taken over time and the image of plasma-treated graphene surface demonstrated that single-layer graphene reacts more rapidly and vigorously towards chemical modifications than bi-layer graphene. Just as the root of different behaviours between a piece of paper and a stack of paper, in double-/few-layer graphene, the formation of wrinkles might have been suppressed, so the plane is more flattened out than in single-layer graphene. That will reduce the number of irregular sites in bi-layer graphene and make it more chemically stable than single-layer graphene in practice.

2.1.3.2 Mechanical properties

Graphene is both light and thin, with a density of 2.267 g/cm^3 and a thickness of 0.34nm. Namely, if we pave 1 gram of graphene sheet on the floor, it will take up an area of 2,630 m^2, and 1 m^2 of graphene weighs only 0.77 milligrams.

The strong δ bonds between atoms grant graphene a high intrinsic tensile strength (the maximum stress a material can bear before failing when being pulled) of 130 Gigapascal (GPa), making it one of the most robust materials in the world [29]. Graphene also exhibits a high stiffness (the extent of resistance to deformation) with an estimated Young's modulus of 1.0 Terapascal (TPa) [30] to 2.4 TPa [31] for the same reason. Even though graphene is highly resistant to deformation, it is the most stretchable crystal at the same time as it can perform an elastic deformation until elongated up to 20% of its original dimension [29].

P. Zhang conducted an in-situ tensile test on pre-cracked graphene, believing that it is the fracture toughness (the ability of a material to resist crack propagation under an applied force) rather than the intrinsic strength that determines the actual behaviour of graphene in practical applications [32]. In the test, graphene experienced a rapid brittle fracture as ceramic materials do at considerably lower stress levels of only a few GPa. The result suggested that while perfect graphene sheets are strong and highly

stretchable, defected or cracked graphene sheets may exhibit significantly different characteristics. One should bear such differences in mind when putting graphene into practical use.

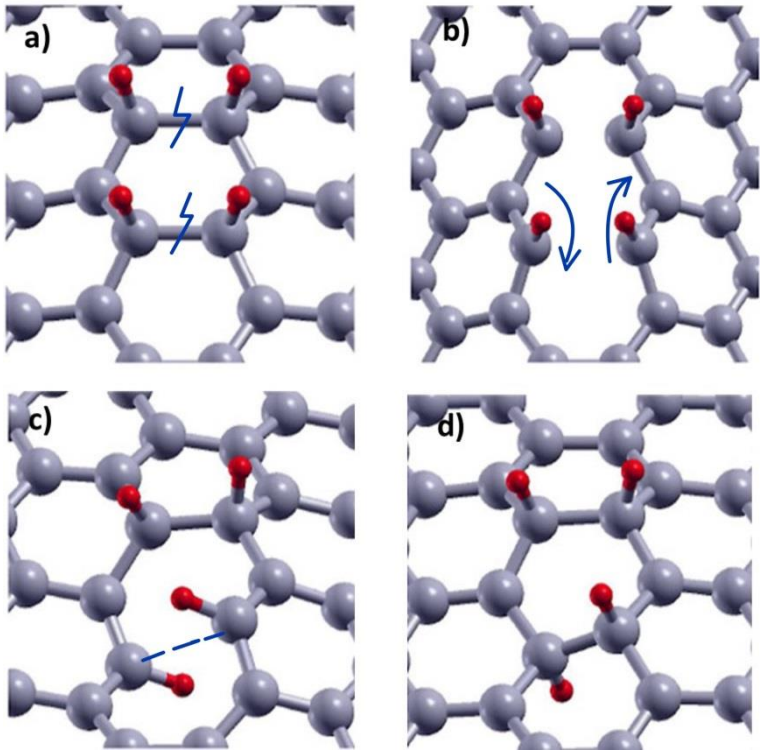

Figure 2.7. Schematic diagram of hydrogen chemisorption and flipping on the graphene surface. a) Some carbon atoms cut their bonds with other neighbouring carbon atoms and formed temporary bonds with hydrogen atoms instead. b) The dangling bonds began to twist. c) One of the hydrogen atoms flipped to the other side of the surface. d) Temporary bonds broke, and the original covalent bonds between carbon atoms were restored; the flipping of hydrogen was completed [37].

Finally, graphene is highly impermeable, even for helium (He) molecules [33, 34]. However, it was found that defect-free graphene membranes are permeable to hydrogen (H_2) gas molecules even though they are larger than helium molecules [35]. Geim's group proposed that this peculiar phenomenon may be associated with the ripples in graphene planes [36]. **Figure 2.7** depicts a possible mechanism behind it. Some bonds in H_2 molecules broke near the surface of a catalytically active graphene ripple. Individual hydrogen atoms then bonded temporarily with the carbon atoms

(this step is also called the chemisorption of hydrogen atoms). Following a flip, hydrogen atoms appeared on the other side of the graphene membrane and bonded to form H_2 molecules again. The hypothesis indicated that curved monolayer graphene surface is more catalytically active. Therefore, instead of single-layer graphene, using bi-layer graphene may help in hydrogen storage. This finding is also in accordance with graphene's chemical properties discussed in the previous section.

2.1.3.3 Electrical and electronic properties

Graphene's peculiar band structure leads to a high current density of 0.1~1.0 $\times 10^8$ A/cm^2 [38, 39] (at least 100 times that of copper [40]) and also ultrahigh carrier mobility of 200,000 cm^2/V·s at room temperature[41] (double that of carbon nanotubes [42] and 200 times that of crystalline silicon [43]).

The high speed and efficiency in electron conduction make graphene an excellent conductor. However, materials for transistors must have a band gap so we can switch the current on by exciting electrons in the non-conductive valence band to conduction band with a moderate amount of energy input as well as switch the current off by terminating the energy input. The gap has to be wide enough, so there is a stark contrast between on and off states. Since graphene has no band gap, it cannot be directly used to make transistors. Techniques have been developed to overcome this problem by 1) introducing boron nitride or molybdenum disulfide as the transport barrier [44-46]; 2) fluorination of graphene [47, 48]; or 3) taking advantage of the substrates [49-51] in order to open the band gap.

2.1.3.4 Thermal properties

Graphene can isotropically conduct heat at a remarkable rate of 5300 W/m·K. That is five times higher than the thermal conductivity of diamond. Even though this ideal

value is yet to be achieved as the actual thermal conductivities reported by researchers are usually between 600 W/m·K to 2000 W/m·K [52-54] for graphene membranes and 30 W/m·K to 200 W/m·K for graphene composites [55, 56]. Nevertheless, the improvements are evident, and graphene is still a promising material in the field of thermal conducting.

2.1.3.5 Optical properties

Graphene has a relatively constant opacity regardless of any variance in its in-plane dimensions, reported by Geim's group in 2008 [57]. Monolayer graphene in the vacuum can absorb 2.3% of the incident light, which is a reasonably large fraction for 2D materials but still not large enough to make it visible to naked eyes. With graphene's exceptional electronic and mechanical properties, graphene has become an excellent candidate for transparent, stretchable electrodes [58-60], wearable electronic devices and sensors [61-63].

2.2 Synthesis of 2D/3D graphene

2.2.1 Overview of graphene production techniques

2.2.1.1 Mechanical exfoliation

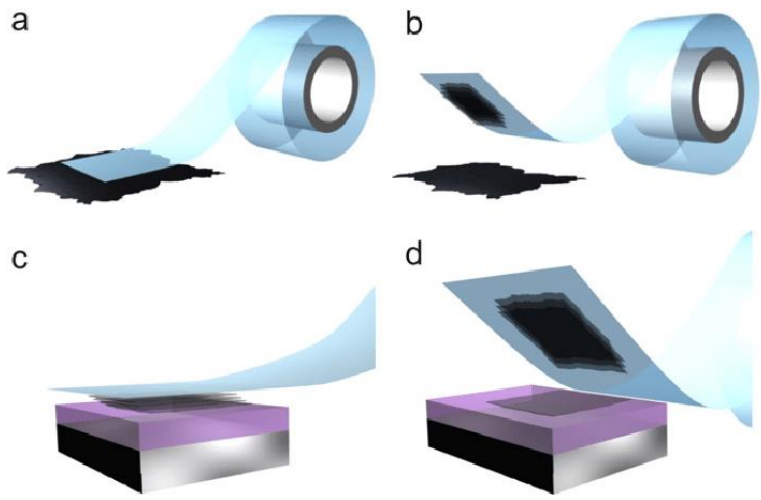

Figure 2.8. Steps of mechanical exfoliation and transfer of graphene. a) Place adhesive tape against the surface of graphite. b) Lift the tape and peel the top carbon layers off. c) Press the tape against a desired substrate. d) Lift the tape again to leave the bottom mono- or few-layer graphene on the substrate [64].

As was described in section 2.1.1, mechanical exfoliation was the first method ever adopted that has successfully isolated graphene from graphite. **Figure 2.8** can give us a picture of how this technique works. To obtain single-layer graphene, the exfoliation steps are usually repeated several times on tape before the transfer of graphene to substrate illustrated in **Figure 2.8** c) and d) is carried out.

Graphene produced by mechanical exfoliation possesses high qualities. Therefore, it is still widely used in fundamental studies of graphene up to now [64-66] even though the yield of this method is meagre, and the products are usually mixtures of graphene flakes with various numbers of layers.

2.2.1.2 Liquid-phase exfoliation (LPE)

This method involves exfoliating graphite in a liquid environment. Graphite is first immersed in suitable solvents such as N-methyl-2-pyrrolidinone (NMP) [67, 68], N,N-dimethylformamide (DMF) [69] or ortho-dichlorobenzene (ODCB) [70, 71]. These solvents typically have comparable surface tensions to graphene. Together with the assistance of graphite-solvent interaction, ultrasonication will help overcome the weak Van der Waals forces between graphite layers and exfoliate graphite into thinner chips. The solution will then be left aside for a period of time, which is long enough for thicker and heavier flakes to settle. Over time, it will separate into layers with fewer-layer graphene floating at the surface and larger chunks sinking at the bottom.

Graphene produced via LPE is also defect-free and of high quality. The exfoliation process is affordable, flexible and up-scalable, but the costs of solvents and removal of solvents can be very high.

2.2.1.3 Chemical reduction of graphene oxide

Mass-production of graphene is mainly realised by reducing graphene oxide (GO) to rGO at present. Its outstanding yield, low cost, scalability, and flexibility for functionalisation have drawn numerous researchers' attention.

Before reduction takes place, GO is usually prepared following the Hummers' method in advance [72]. This method was developed by William S. Hummers and Richard E. Offeman back in 1958. It has stood the test of time and remained an efficient and well-recognised protocol for GO preparation up to now.

This procedure begins with the addition of graphite and sodium nitrate mixture to sulfuric acid. In this step, graphite is preliminarily intercalated and oxidised by sulfuric acid. The mixture is kept in an ice bath since the temperature will rise as the reaction

progresses. Potassium permanganate is then added to the suspension to form a strong oxidant with sulfuric acid. The oxidant can further intercalate into graphene layers and even destroy the covalent bonds in graphene's basal plane while attaching hydroxyl (-OH), epoxide (C-O-C), carboxylic (-COOH) and carbonyl (C=O) groups to the graphene surface [73, 74]. The attached groups, primarily hydrophilic, will turn the intrinsically hydrophobic graphene into graphene oxide and disperse it in water. After the reaction completes, the mixture is poured into a great amount of water and residue of potassium permanganate is removed by repeated cleansing and filtering with aqueous preoxide hydrogen.

The reduction of graphene oxide can be realised through a) chemical reduction with the aid of reductants such as acetic acid [75], hydrazine [76] and hydroiodic acid [77]; b) thermal treatment at high temperatures to induce decomposition of oxygen-containing functional groups [78]; c) photothermal reduction via infrared radiations [80], d) electrochemical reduction [81]; e) hydrothermal dehydration [82]; and solution deposition [83]. Defects introduced in the oxidation stage can be partly fixed through reduction. The mechanical, electrical performance exhibited by rGO is usually intermediate between that of pure graphene and graphene oxide [84, 85].

The benefits and drawbacks of this approach are both distinct. The cost is low while the yield is incomparably high. Also, multi-step chemical reactions offer possibilities to modify and control graphene's properties by functionalisation or structure alterations. However, throughout the manufacturing process, the reactions need either toxic reagents or high temperatures, which will pose risks to people’s health as well as the environment. Besides, since the defects induced cannot be fully fixed via reduction, the quality of the obtained products is relatively poor.

2.2.1.4 Epitaxial growth of graphene

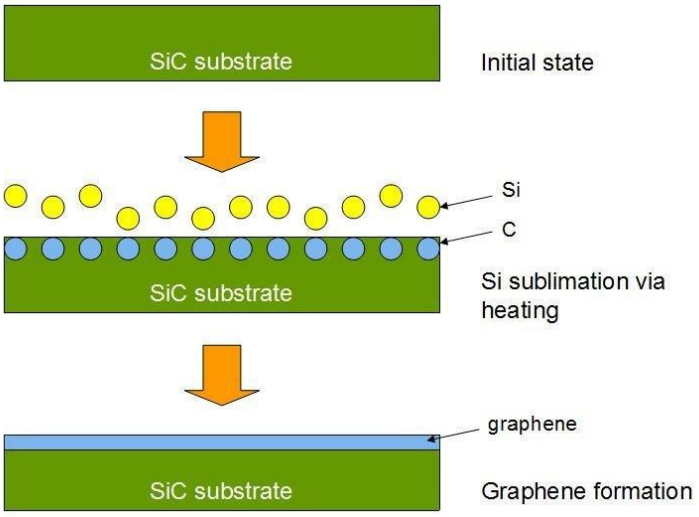

Figure 2.9. Schematic diagram of epitaxial growth of graphene on silicon carbide (SiC) substrate. Silicon sublimates and escapes from the substrate at high temperatures, leaving surplus carbon exposed at the surface to form graphene [86].

Epitaxy refers to a technique of growing graphene on a substrate of choice directly. **Figure 2.9** illustrates the formation of graphene on top of a flat silicon carbide (SiC) substrate. SiC sublimation growth usually occurs at high temperatures above 2800 °C [87]. However, this temperature can be reduced to around 800 °C in an ultra-high vacuum [88] or 1650 °C in an Ar environment [89]. Silicon near the surface sublimates at high temperatures, leaving carbon atoms exposed at the surface. These carbon atoms will then rearrange themselves and form bonds with each other above. Other than Si, single crystal metals such as Platinum (Pt) [90], Ruthenium (Ru) [91, 92], Cobalt (Co) [93] and Copper (Cu) [94] also support epitaxial growth of graphene on their surfaces.

Growing graphene on a substrate has wholly avoided any defect induced during the transfer process. Thus, researchers can proceed to characterise its properties or fabricate transistors and electronic devices on the wafer straightaway [95, 96]. On the other hand, the dimensions of such products are limited by the size of their substrates.

It also requires significant energy inputs for the high-temperature treatment. Moreover, high-quality monolayer graphene is only achievable through precise control over temperature, growth time, environment and substrate quality.

2.2.1.5 Chemical vapour deposition (CVD)

Conventionally, CVD involves exposing a proper substrate to a flow of gaseous carbon sources in a reactor chamber. Decomposition of the gaseous carbon source and deposition of carbon onto the substrate will occur at elevated temperatures. The redundant carbon sources and gaseous by-products will be removed from the chamber by the gas flow.

Further details will be discussed in the next section of this review.

2.2.1.6 Others

While the above sections have covered some of the most mainstream graphene production methods, others such as electrochemical exfoliation [97, 98], unzipping carbon nanotubes [99], flame synthesis [100] and Laser-Induced Graphene (LIG) [101, 102], are also under development.

Aiming to fully exploit graphene's extraordinary properties and bring this material to market in the near future, the number and impact of researches on graphene-related materials have increased dramatically since its discovery [103]. As a result, the list of graphene fabrication methods is still increasing.

2.2.2 Synthesis of 3D graphene

Not to be confused with graphite, 3D graphene here refers to single- or few-layer graphene built into 3D structures. Such material should exhibit similar properties to 2D graphene and differ from graphite materials with considerably larger surface areas and higher electron mobility.

The approaches to realise this design are developed on the basis of studies of 2D graphene growth to a great extent. The most popular techniques in 3D graphene synthesis are mainly derived from the reduction of GO and graphitisation or graphenesation of hydrocarbons.

The top-trending graphene 3D fabrication technique should go to 3D printing. Due to graphene's poor dispersal ability, the ink synthesised for printing mainly comprises GO instead of graphene. This technology allows us to build a 3D graphene scaffold of any complex shape as long as its solid model is provided. After a layer-by-layer ink deposition on the substrate, the GO framework is thermally [104] or chemically [105] reduced to rGO before being put to use.

Other techniques based on GO such as hydrothermal reduction of self-assembled GO [106, 107], freeze-casting of GO aerogels [108, 109] and photocatalytic reduction of GO [110] are also extensively adopted in 3D graphene synthesis.

The advantages of rGO-related methods are: fast design; moderate cost; and potential for scale-ups. However, just as in 2D rGO, a significant number of in-plane and cross-plane defects are often observed in 3D graphene derived from GO. Besides, as reduction goes on, the excellent dispersal ability of GO is also gradually lost [111]. As a result, rGO will again tend to agglomerate, sacrificing its thermal and electrical conductivities.

Apart from GO, hydrocarbons can also act as suppliers of carbon atoms in 3D graphene fabrication. Gaseous hydrocarbons are generally decomposed and constructed into three dimensions via CVD [112, 113] or plasma-enhanced chemical vapour deposition (PECVD) [114, 115], while the conversion from liquid and solid hydrocarbons are usually laser-induced [116, 117] or heat-induced [118, 119], similar to CVD.

When it comes to hydrocarbons, a pre-prepared 3D structure made of metal catalysts or polymerised carbon sources are often involved, through which graphene can be built into modifiable shapes. Using solid hydrocarbons rather than gaseous hydrocarbons in the fabrication offered more options as there are plentiful kinds of amorphous carbon and polymers accessible. In pursuit of high-quality 3D graphene production, a good deal of factors should be deliberately controlled, such as reaction temperature, heating and cooling rates, time of graphene growth, selection of carbon source as well as metal catalyst and condition of substrates, etc.

The technique adopted in this project for 3D graphene fabrication is under the category of thermally treating hydrocarbons with the aid of metal catalysts. The principles, representative cases, challenges and progress of this method will be discussed in the following section.

2.3 Synthesis of graphene via catalytic graphitisation of solid carbon sources

2.3.1 2D graphene growth via catalytic graphitisation of solid carbon sources

Catalytic graphitisation in graphene synthesis greatly resembles CVD in the sense of their mechanisms. The major difference is the state of the carbon source chosen in these two techniques. Gaseous volatile precursors are more frequently used in CVD, while catalytic graphitisation usually involves using amorphous carbon, hydrocarbons or polymers. Since CVD is more well-established compared with catalytic graphitisation, this chapter will begin with an introduction to the working principles behind CVD before we jump to catalytic graphitisation from solid carbon sources.

The mechanisms of CVD graphene growth generally fall into two categories, depending on the interaction between graphene and the transition metal substrates.

2.3.1.1 CVD on substrates that strongly interact with graphene

Nickel (Ni) is a typical example of transition metals that will strongly interact with graphene. That reflects on the excellent solubility of carbon in Ni. Ni also has a matching lattice index with graphene [120]. These features enable carbon atoms to better align with the ordered nickel surface and diffuse in a nickel substrate during and after the growth, thus producing neat and ordered graphene sheets [121].

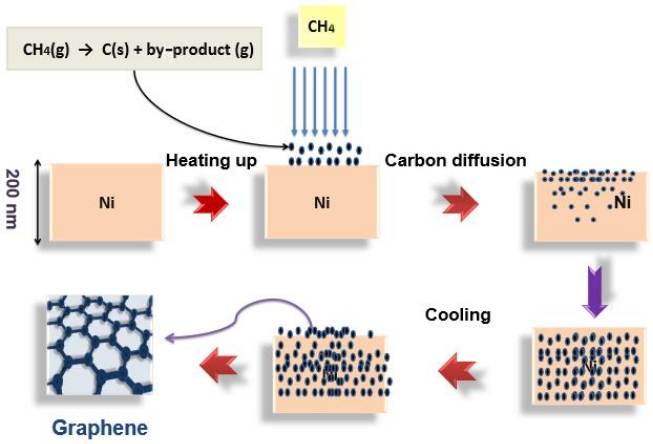

Figure 2.10. Schematic diagram illustrating the mechanism of CVD graphene growth on a Ni foil. Methane (CH_4) was decomposed to carbon at Ni surface upon heating. An enormous amount of carbon atoms diffused into Ni substrate due to its good solubility. Upon cooling, carbon atoms near the surface precipitated and rearranged to form graphene [122].

As illustrated in **Figure 2.10**, the CVD growth of graphene on Ni followed these steps: (1) when the temperature of the reactor chamber is in the range 700 °C to 1300 °C, the gaseous carbon source, methane (CH_4) in this case, decomposed into carbon and hydrogen at the nickel surface following the chemical reaction:

$$CH_4(g) \rightarrow C(s) + 2H_2;$$

(2) on account of the excellent solubility of carbon in Ni, the carbon atoms diffused deeper into the foil until the point of saturation was reached; (3) upon the cooling process, carbon atoms precipitated on the metal surface due to the decrease in its solubility with decreasing temperature.

The great quantity of dissolved carbon and the ease of carbon atoms diffusing freely in Ni implied that the amount of carbon precipitated onto the surface should also be significant. As a result, graphene produced with such substrates is inclined to have a multi-layer structure instead of a monolayer structure.

Other transition metals which interact with carbon in a similar way as Ni, including Ru

[123], Rhenium (Re) [124] and Rhodium (Rh) [125], are also frequently chosen to be the substrate for CVD graphene growth.

2.3.1.2 CVD on substrates that weakly interact with graphene

Another system is represented by Cu, whose interaction with graphene is very weak. Since copper hardly dissolves or interacts with carbon atoms, the growth of graphene on a copper foil is regarded as a surface reaction. No dissolving-precipitating process is involved.

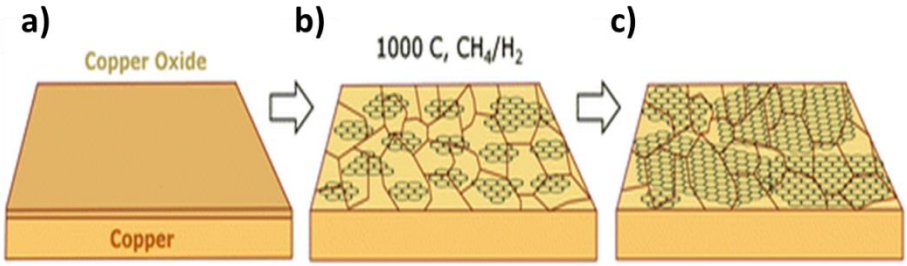

Figure 2.11. Schematic diagram illustrating the mechanism of CVD graphene growth on copper foil [126]. a) Cu substrate was initially covered with a protective oxide layer. b) Oxide layer was reduced around 1000 °C in an atmosphere filled with CH_4 as the gaseous carbon source and hydrogen as the reducing agent as well as a carrier gas. Tiny graphene islands showed up at grain boundaries. c) Graphene islands grew in size and met each other to form a continuous graphene film on the Cu surface.

As described in **Figure 2.11**, the growth of graphene on a Cu foil has also taken a few steps: (1) as a result of annealing at high temperature, the copper oxide layer was reduced to Cu. In the meanwhile, the Cu foil went through recrystallization. Grains oriented differently were formed at the surface; (2) at this high temperature (~1000 °C), the gaseous carbon source decomposed near the active Cu surface while graphene islands nucleated preferably at the grain boundaries since it consumes less nucleation energy [126]; (3) along with the decomposition of CH_4, graphene islands continued to grow and eventually merged into one thin film from different directions.

Unlike Ni foils, graphene grown on Cu foils is typically limited to be one-atom-thick as

the layer initially formed on the surface will shield the Cu from redundant carbon atoms. However, structural defects related to the boundaries formed between coalescing graphene islands can also impair graphene's quality and electronic performance [127]. Other transition metal substrates under this category can be Iridium (Ir) [128] and gold (Au) [129].

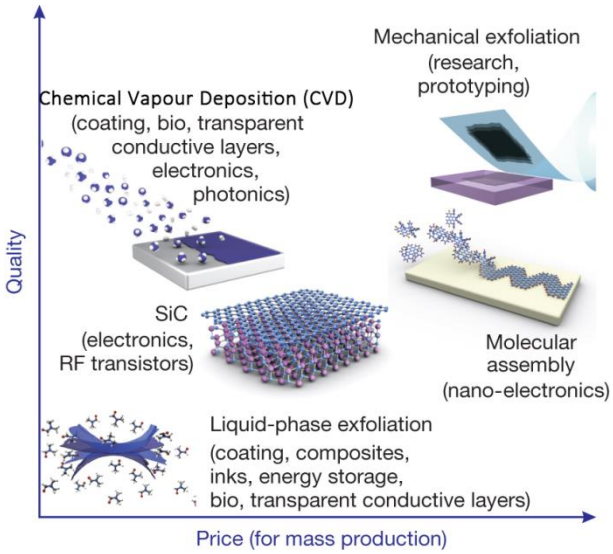

Figure 2.12. Diagram comparing the applications, qualities and prices of various graphene production methods [130].

Five typical industrial production methods are compared in **Figure 2.12**. It is evident that CVD (Chemical Vapour Deposition) is one of the cheapest methods to produce high-quality graphene. Besides, it can be adapted to meet the needs of multiple applications [131-133]. Therefore, the CVD technique was chosen as the main subject of our study.

Despite CVD's advantages, it is not easy to precisely control the temperature for growing high-quality monolayer graphene either with Ni system metal catalysts or Cu system metal catalysts. Also, the reacting temperature is usually above 1000 °C, and the options for the gaseous carbon sources are limited.

2.3.1.3 Approach of 2D graphene preparation with solid carbon sources inspired by CVD

Inspired by the CVD method, Sun's group first developed the technique for growing monolayer graphene from solid carbon sources instead of gaseous carbon sources [134].

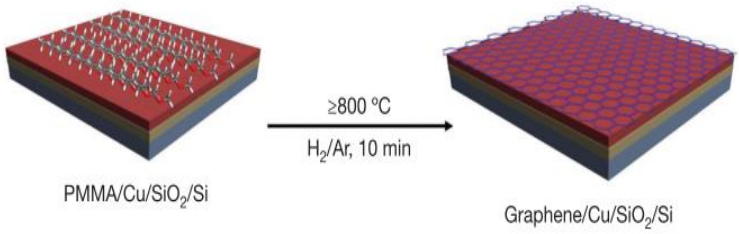

Figure 2.13. A schematic diagram of growing monolayer graphene from solid PMMA film on a Cu foil. Spin-coated PMMA film on Cu and SiO_2/Si substrate was annealed above 800 °C in a mixture of H_2 and Argon (Ar) gases for 10 minutes and converted to graphene [134].

As illustrated in **Figure 2.13**, a thin film (~100 nm) of PMMA was first spin-coated onto a Cu foil. Then, a uniform graphene sheet was produced on the Cu foil after exposing the foil to a H_2/Ar atmosphere under low pressure at a temperature as low as 800 °C for 10 minutes. By controlling the gas flow rate, graphene of different number of layers was successfully obtained.

2.3.2 Growth of 3D graphene from solid carbon sources

2.3.2.1 3D graphene prepared with solid carbon source and pure metal catalyst

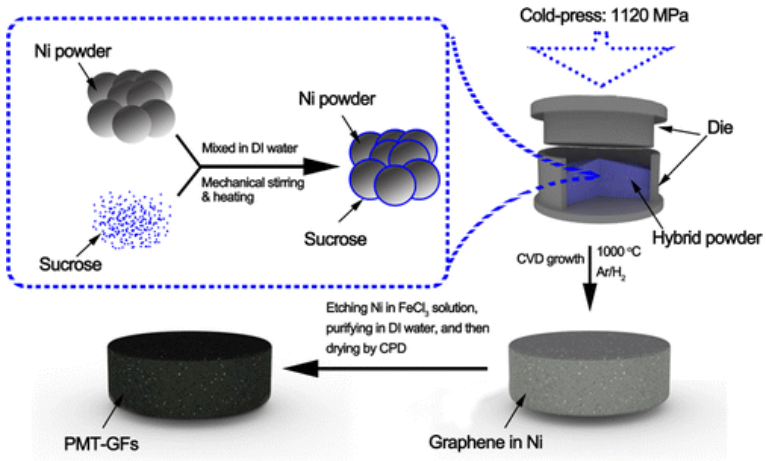

Figure 2.14. Schematics diagram of preparing 3D graphene foam with powder-form sucrose as carbon source and Ni powder as catalytic template [135]. Ni powder and sucrose were mixed in deionised water with stirring and heating. Ni powder covered with sucrose was then cold-pressed into pellets. After annealing at 1000 °C in H_2/Ar atmosphere, sucrose turned into graphene on the Ni template. The removal of Ni was carried out through etching and cleansing with $FeCl_3$ and deionised water.

Sha's group took a step further and adapted this technique of fabricating graphene from solid carbon sources into growing 3D graphene foams [135].

Figure 2.14 demonstrates the entire process of a templated 3D graphene foam synthesis. Nickel powder was used as the metal catalyst, template, and pore former, while sucrose (also known as table sugar) was used as the solid carbon source. The two kinds of powders were mixed in deionised water under mechanical stirring at elevated temperatures. In this step, since sucrose is soluble in water, it can be well dispersed. Meanwhile, as Ni has poor solubility in water, it will stay in its solid form and may cause agglomeration due to poor dispersion. After the mixing, Ni particles were all wrapped by tiny sucrose particles. The vacuum dried mixture was then cold-

pressed into pellets before being sent for heat treatment. During the heat treatment, the temperature was raised to 1000 °C at a rate of 10 °C /min. The annealing was also carried out in a H_2/Ar atmosphere. After 30 min, carbon atoms in PMMA were converted to graphene, which further wrapped the Ni template. Eventually, after removing Ni particles through etching in $FeCl_3$ solutions and repeated washing in deionised water, 3D graphene foam was achieved.

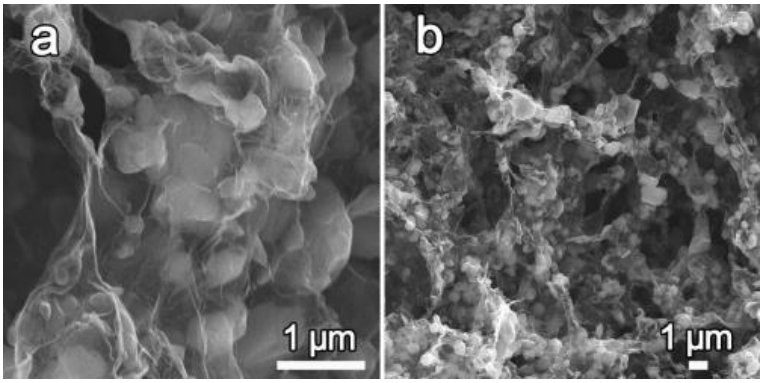

Figure 2.15. a, b) SEM images of the graphene foam prepared by Sha's group [135].

SEM images of graphene foam's internal structure are shown in **Figure 2.15**. Since Ni powder stayed in its solid state during the mixing process, the ultimate structure was not entirely uniform as Ni clusters can easily be spotted. Besides, removing Ni particles was a challenging task. Even though the $FeCl_3$ aqueous solution was refilled and changed every day, some Ni particles remained wrapped in thin graphene membranes after seven days of treatment. It could result from graphene's impermeability, as water molecules and ions may not reach Ni through the intact graphene surface. However, some molecules and ions can still get to Ni particles through pores and cracks in the graphene plane or gaps between different membrane layers.

By making use of different moulding strategies, free-standing 3D graphene foams of various structures and shapes can be synthesized through this approach. The method is easy to deploy and cost-saving given the relatively good yield with extremely cheap solid carbon source and catalyst. The key challenges here are 1) to reduce clustering

of fine nickel particles for a more uniform 3D structure and 2) to improve the efficiency and effectiveness of removing catalyst particles after graphene growth.

2.3.2.1 3D graphene prepared with solid carbon source and ionic metal catalyst

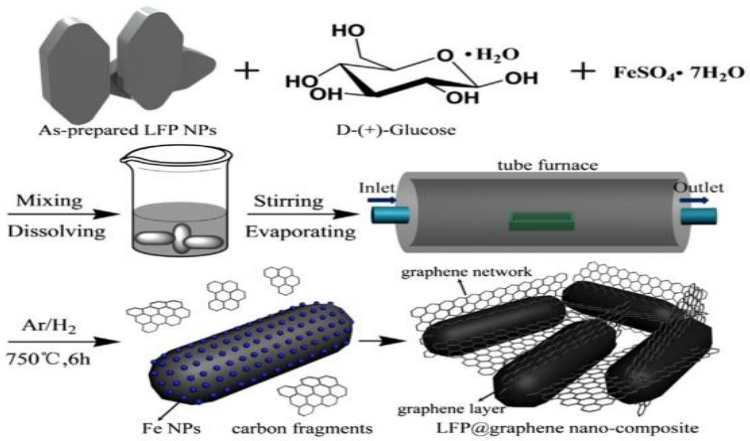

Figure 2.16. Schematic diagram of growing graphene onto Lithium iron phosphate (LFP) particles with glucose and iron (II) sulfate ($FeSO_4$) [136]. All chemicals were homogeneously mixed in deionised water. After water evaporated, the mixture was placed in a quartz boat at the centre of a tube furnace. Graphene was grown on the LFP surface in an atmosphere filled with H_2/Ar for six hours at 750 °C.

In Zhang's work illustrated in **Figure 2.16**, graphene was grown around Lithium Iron Phosphate (LFP) battery particles to enhance the supercapacitor's electrochemical property.

Instead of using iron metal particles as the catalyst, iron (II) sulfate ($FeSO_4$) was used and mixed with a water-soluble solid carbon source – glucose – in deionised water. The LFP particles were also added to the solution to be wrapped by the ions. After water evaporation and drying, the mixture was sent for heat treatment in a tube furnace. During the heat treatment at 750 °C with Ar/H_2 gases, $FeSO_4$ was reduced to iron (Fe) nanoparticles while carbon was produced from pyrolysis of glucose. Fe further acted as the catalyst to stimulate graphene growth on the LFP surface.

Aiming to improve the electrochemical properties of LFP cathode in supercapacitors instead of fabricating pure graphene foam, the LFP and Fe particles were not removed and left in the final product as they were. Therefore, we can hardly evaluate the feasibility of metal particle removal in this research. Nevertheless, this article has provided insight into overcoming the first challenge in graphene synthesis with a solid carbon source: avoiding clustering of the metal catalysts by using catalysts in their ionic states at the mixing stage. Unlike pure metals, which intend to be insoluble and settle at the bottom of containers during the mixing, ionic catalysts can be homogeneously mixed with the carbon sources in a proper solvent that is soluble for both.

2.3.3 Factors to consider in catalytic graphitisation of solid carbon sources

Multiple parameters can be modified in each stage of the 2D/3D graphene fabrication process. Each parameter may affect the reaction and thus, affect the quality of the final product. Therefore, it is crucial to find a suitable range of values for each parameter and a proper combination of multiple parameters. The factors to be investigated for producing graphene will be discussed in this section.

2.3.3.1 Heat treatment temperature

It was reported that the growth of graphene from PMMA on a copper foil has a lower temperature limit of 800 °C, below which it is difficult for high-quality graphene to grow [131].

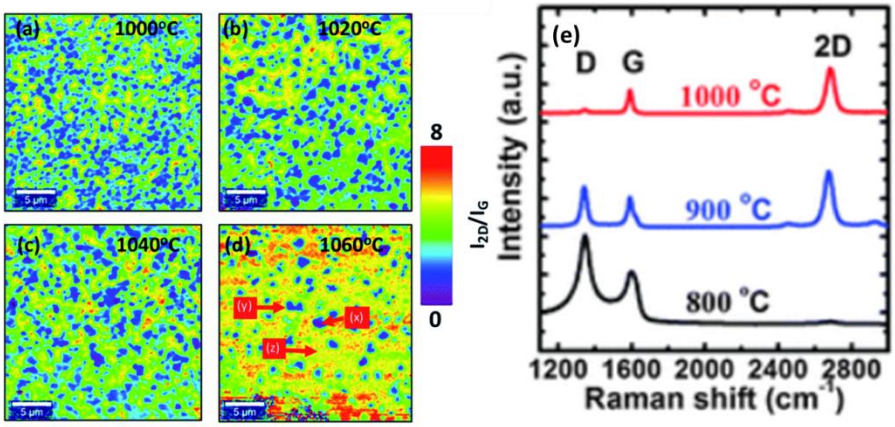

Figure 2.17. Raman maps of intensity ratio I_{2D}/I_G in different CVD synthesised graphene flakes on Cu substrates at (a) 1000 °C, (b) 1020 °C, (c) 1040 °C, (d) 1060 °C [137] and Raman spectra of graphene synthesised with solid-state carbon source PMMA on Cu substrates at different temperatures (800 °C, 900 °C and 1000 °C) [138].

The effect of heat treatment temperature on the quality of graphene synthesised either with gaseous carbon sources or solid carbon sources was also studied in multiple research. Raman maps in **Figure 2.17** (a)-(d) compared the ratios of I_{2D}/I_G peak

intensities detected in CVD grown graphene at temperatures from 1000 °C to 1060 °C [137]. In simple terms, an $I_{2D}/_{IG}$ ratio greater than two generally indicates the existence of good quality monolayer graphene [139]. By increasing heat treatment temperature, the average number of graphene layers in most synthesised graphene flakes were decreased. **Figure 2.17** (e) displayed the typical Raman spectra obtained from graphene synthesised with PMMA on Cu substrate at temperatures from 800 °C to 1000 °C [138]. As the temperature increased, the defect-related D peak around 1350 cm^{-1} was weakened while the 2D peak around 2690 cm^{-1} was strengthened, again indicating more monolayer graphene, rather than multi-layer graphene, in the product. The reduced I_D/I_G ratio with rising temperature also suggested improved graphene quality with reduced defects [140].

Essentially, better-quality graphene can be obtained at higher reaction temperatures with either a gaseous or solid carbon source. That might have resulted from the decomposition of carbon sources to a greater extent as a more considerable amount of thermal energy input is employed. More bonds between carbon and hydrogen/oxygen can be broken, thus reducing potential structural and chemical defects caused by these atoms or groups attached to the carbon surface. However, higher heat treatment temperature will also lead to increased electrical energy consumption and a higher cost for graphene synthesis. Therefore, quality and cost should be balanced in the process of fabrication.

2.3.3.2 Heating rate

In Kwak's work, they also investigated the influence of heating rate in graphene synthesis with PMMA on Cu [138]. Rates of 3.3 °C/s, 8.3 °C/s and 33.3 °C/s were examined, and a conclusion was drawn that rapid heating will contribute to the formation of single-layer graphene with fewer defects.

Meanwhile, it was observed that with an increased heating rate, the temperature at which PMMA starts to decompose into monomer methyl methacrylate (MMA) and release gases, is also raised. According to the kinetic and thermodynamic model proposed by C. T. Moynihan, the glass transition temperature is proportional to the logarithm of heating and cooling rate [141]. The following equation approximated the dependence:

$$\frac{d(ln\,|q|)}{d(\frac{1}{T_g})} \approx -\frac{\Delta h*}{R}$$

In the equation, q is the heating or cooling rate; T_g is the glass transition temperature; Δh* is the activation enthalpy (the minimal amount of energy that must be supplied for a reaction to take place), and R is the universal gas constant.

The results in Kwak's research showed that higher heating rates could help produce higher-quality graphene. However, Moynihan's model suggested that by adopting a higher heating rate, the heat treatment temperature required is also increased, which will lead to higher energy consumption. Besides, rapid heating can be demanding for some equipment, while the sudden, violent release of gases may even destroy the templated structure, leaving holes and cracks inside the 3D scaffold and impairing graphene's mechanical and electronic performance. Thus, multiple trade-offs regarding the energy input and the graphene quality are involved.

2.3.3.3 Ratio of carbon to metal

The ratio of the number of carbon atoms to the number of metal atoms is another crucial factor to be considered.

If a metal catalyst is chosen from the "Ni system", then carbon will have good solubility in such metal. In that case, more attention should be paid to the under-coverage issue

as well as the over-coverage of carbon. A high carbon/metal ratio will perhaps result in multi-layer graphene rather than single-layer graphene. In contrast, a low carbon/metal ratio may cause insufficiency of carbon in the formation of graphene, leaving vacancy-type defects at the graphene surface [136].

Otherwise, if the metal catalyst is categorised under the “Cu system”, which means only a surface reaction is involved, theoretically, over-coverage should not occur since the initially grown graphene monolayer will shield the metal catalyst from excessive carbon atoms. However, in practice, due to the presence of impurities in such substrates, bi-/multi-layer graphene can also be formed when carbon atoms take surfaces of these impurities to be the nucleation sites [142]. On the other hand, it is also crucial to ensure an abundant carbon supply so the under-coverage issue can be avoided.

2.3.3.4 Others

Soaking time: soaking time refers to the period of time material is held at the desired temperature. The time required for growing graphene on different templates can vary from a few seconds [143] to several hours [136]. Generally, a lower pressure in the reactor chamber and a higher heat treatment temperature can shorten the time required to complete the reactions.

Gas flow rate: gas flow rate may affect the concentration of carbon-containing molecules in the reactor chamber, thus altering the carbon to metal ratio from time to time. With deliberate control of the gas flow rate, graphene with different number of layers can be produced [134].

Cooling rate: cooling rate is another crucial factor to control, especially in ‘Ni system’ substrates. It mainly affects the precipitation process in the way that: if the cooling is too fast, carbon atoms dissolved in metal will not have sufficient time to diffuse to or

precipitate at the surface, causing carbon shortage in forming a full graphene layer; and if the cooling is too slow, carbon atoms dissolved can all precipitate and engage in the graphene growth, causing a formation of multi-layer graphene instead of forming mono-layer graphene.

References

[1] Novoselov, K.S., Geim, A.K., Morozov, S.V., Jiang, D., Zhang, Y., Dubonos, S.V., Grigorieva, I.V. and Firsov, A.A., 2004. Electric field effect in atomically thin carbon films. *Science*, *306*(5696), pp.666-669.

[2] Peierls, R., 1935. Quelques propriétés typiques des corps solides. In *Annales de l'institut Henri Poincaré* (Vol. 5, No. 3, pp. 177-222).

[3] Landau, L.D., 1937. Zur Theorie der phasenumwandlungen II. *Phys. Z. Sowjetunion*, *11*(545), pp.26-35.

[4] Pauling, L., 1960. *The Nature of the Chemical Bond.* (Vol. 260, pp. 3175-3187). Ithaca, NY: Cornell university press.

[5] Wallace, P.R., 1947. The band theory of graphite. *Physical Review*, *71*(9), p.622.

[6] Mermin, N.D. and Wagner, H., 1966. Absence of ferromagnetism or antiferromagnetism in one-or two-dimensional isotropic Heisenberg models. *Physical Review Letters*, *17*(22), p.1133.

[7] Mermin, N.D., 1968. Crystalline order in two dimensions. *Physical Review*, *176*(1), p.250.

[8] Lu, X., Yu, M., Huang, H. and Ruoff, R.S., 1999. Tailoring graphite with the goal of achieving single sheets. *Nanotechnology*, *10*(3), p.269.

[9] Ebbesen, T.W. and Hiura, H., 1995. Graphene in 3‐dimensions: Towards graphite origami.

[10] NobelPrize.org. 2010. Andre Geim Nobel Lecture. [online] Available at: https://www.nobelprize.org/prizes/physics/2010/geim/lecture/

[11] Novoselov, K.S., Jiang, D., Schedin, F., Booth, T.J., Khotkevich, V.V., Morozov, S.V. and Geim, A.K., 2005. Two-dimensional atomic crystals. *Proceedings of the National Academy of Sciences*, *102*(30), pp.10451-10453.

[12] Geim, A.K., 2012. Graphene prehistory. *Physica Scripta*, *2012*(T146), p.014003.

[13] Moon, J.Y., Kim, M., Kim, S.I., Xu, S., Choi, J.H., Whang, D., Watanabe, K., Taniguchi, T., Park, D.S., Seo, J. and Cho, S.H., 2020. Layer-engineered large-area exfoliation of graphene. *Science Advances*, *6*(44), p.eabc6601.

[14] Ni, Z.H., Wang, H.M., Kasim, J., Fan, H.M., Yu, T., Wu, Y.H., Feng, Y.P. and Shen, Z.X., 2007. Graphene thickness determination using reflection and contrast spectroscopy. *Nano Letters*, *7*(9), pp.2758-2763.

[15] Wilson, M., 2006. Electrons in atomically thin carbon sheets behave like massless particles. *Physics Today*, *59*(1), p.21.

[16] Zhang, Y., Tan, Y.W., Stormer, H.L. and Kim, P., 2005. Experimental observation of the quantum Hall effect and Berry's phase in graphene. *Nature*, *438*(7065), pp.201-204.

[17] Meng, L., Su, Y., Geng, D., Yu, G., Liu, Y., Dou, R. F., ... & He, L. (2013). Hierarchy of graphene wrinkles induced by thermal strain engineering. *Applied Physics Letters*, *103*(25), 251610.

[18] Bai, K. K., Zhou, Y., Zheng, H., Meng, L., Peng, H., Liu, Z., ... & He, L. (2014). Creating one-dimensional nanoscale periodic ripples in a continuous mosaic graphene monolayer. *Physical Review Letters*, *113*(8), 086102.

[19] Zang, J., Ryu, S., Pugno, N., Wang, Q., Tu, Q., Buehler, M. J., & Zhao, X. (2013). Multifunctionality and control of the crumpling and unfolding of large-area graphene. *Nature Materials*, *12*(4), 321-325.

[20] Geim, A.K. and Novoselov, K.S., 2010. The rise of graphene. *Nanoscience and Technology: a Collection of Reviews from Nature Journals*, pp. 11-19.

[21] Eftekhari, A., & Garcia, H., 2017. The necessity of structural irregularities for the chemical applications of graphene. *Materials Today Chemistry*, *4*, 1-16.

[22] Liu, J., Tang, J., & Gooding, J. J., 2012. Strategies for chemical modification of graphene and applications of chemically modified graphene. *Journal of Materials Chemistry*, *22*(25), 12435-12452.

[23] Zhang, H., Fonseca, A. F., & Cho, K., 2014. Tailoring thermal transport property of graphene through oxygen functionalization. *The Journal of Physical Chemistry C*, *118*(3), 1436-1442.

[24] Hsiao, M. C., Liao, S. H., Yen, M. Y., Liu, P. I., Pu, N. W., Wang, C. A., & Ma, C. C. M., 2010. Preparation of covalently functionalized graphene using residual oxygen-containing functional groups. *ACS Applied Materials & Interfaces*, *2*(11), 3092-3099.

[25] Boukhvalov, D. W., & Katsnelson, M. I., 2009. Chemical functionalization of graphene. *Journal of Physics: Condensed Matter*, *21*(34), 344205.

[26] Koehler, F. M., Jacobsen, A., Ensslin, K., Stampfer, C., & Stark, W. J., 2010. Selective chemical modification of graphene surfaces: distinction between single‐and bilayer graphene. *Small*, *6*(10), 1125-1130.

[27] Diankov, G., Neumann, M., & Goldhaber-Gordon, D., 2013. Extreme monolayer-selectivity of hydrogen-plasma reactions with graphene. *ACS Nano*, *7*(2), 1324-1332.

[28] Sharma, R., Baik, J. H., Perera, C. J., & Strano, M. S., 2010. Anomalously large reactivity of single graphene layers and edges toward electron transfer chemistries. *Nano Letters*, *10*(2), 398-405.

[29] Lee, C., Wei, X., Kysar, J.W. and Hone, J., 2008. Measurement of the elastic properties and intrinsic strength of monolayer graphene. *Science*, *321*(5887), pp.385-388.

[30] Shokrieh, M. and Rafiee, R., 2010. Prediction of Young's modulus of graphene sheets and carbon nanotubes using nanoscale continuum mechanics approach. *Materials & Design, 31*(2), 790-795.

[31] Lee, J. U., Yoon, D., & Cheong, H., 2012. Estimation of Young's modulus of graphene by Raman spectroscopy. *Nano Letters, 12*(9), 4444-4448.

[32] Zhang, P., Ma, L., Fan, F., Zeng, Z., Peng, C., Loya, P. E., ... & Lou, J., 2014. Fracture toughness of graphene. *Nature Communications, 5*(1), 1-7.

[33] Tsetseris, L., & Pantelides, S. T., 2014. Graphene: An impermeable or selectively

permeable membrane for atomic species?. *Carbon, 67,* 58-63.

[34] Bunch, J. S., Verbridge, S. S., Alden, J. S., Van Der Zande, A. M., Parpia, J. M., Craighead, H. G., & McEuen, P. L., 2008. Impermeable atomic membranes from graphene sheets. *Nano Letters, 8*(8), 2458-2462.

[35] Miao, M., Nardelli, M. B., Wang, Q., & Liu, Y., 2013. First principles study of the permeability of graphene to hydrogen atoms. *Physical Chemistry Chemical Physics, 15*(38), 16132-16137.

[36] Sun, P. Z., Yang, Q., Kuang, W. J., Stebunov, Y. V., Xiong, W. Q., Yu, J., ... & Geim, A. K., 2020. Limits on gas impermeability of graphene. *Nature, 579*(7798), 229-232.

[37] Bartolomei, M., Hernández, M. I., Campos-Martínez, J., Lamoneda, R. H., & Giorgi, G., 2021. Permeation of chemisorbed hydrogen through graphene: a flipping mechanism elucidated. *Carbon*.

[38] Murali, R., Yang, Y., Brenner, K., Beck, T., & Meindl, J. D., 2009. Breakdown current density of graphene nanoribbons. *Applied Physics Letters*, *94*(24), 243114.

[39] Moser, J., Barreiro, A., & Bachtold, A., 2007. Current-induced cleaning of graphene. *Applied Physics Letters*, *91*(16), 163513.

[40] Bares, J. A., Argibay, N., Mauntler, N., Dudder, G. J., Perry, S. S., Bourne, G. R., & Sawyer, W. G., 2009. High current density copper-on-copper sliding electrical contacts at low sliding velocities. *Wear*, *267*(1-4), 417-424.

[41] Bolotin, K. I., Sikes, K. J., Jiang, Z., Klima, M., Fudenberg, G., Hone, J. E., ... & Stormer, H. L., 2008. Ultrahigh electron mobility in suspended graphene. *Solid State Communications*, *146*(9-10), 351-355.

[42] Dürkop, T., Getty, S. A., Cobas, E., & Fuhrer, M. S., 2004. Extraordinary mobility in semiconducting carbon nanotubes. *Nano Letters*, *4*(1), 35-39.

[43] Chen, X. Y., Shen, W. Z., & He, Y. L., 2005. Enhancement of electron mobility in nanocrystalline silicon⁄ crystalline silicon heterostructures. *Journal of Applied Physics*, *97*(2), 024305.

[44] Dean, C. R., Young, A. F., Meric, I., Lee, C., Wang, L., Sorgenfrei, S., ... & Hone, J.， 2010. Boron nitride substrates for high-quality graphene electronics. *Nature Nanotechnology*, *5*(10), 722-726.

[45] Lee, G. H., Yu, Y. J., Cui, X., Petrone, N., Lee, C. H., Choi, M. S., ... & Hone, J.， 2013. Flexible and transparent MoS2 field-effect transistors on hexagonal boron nitride-graphene heterostructures. *ACS Nano*, *7*(9), 7931-7936.

[46] Britnell, L., Gorbachev, R. V., Jalil, R., Belle, B. D., Schedin, F., Mishchenko, A., ... & Ponomarenko, L. A., 2012. Field-effect tunneling transistor based on vertical graphene heterostructures. *Science*, *335*(6071), 947-950.

[47] Cheng, S. H., Zou, K., Okino, F., Gutierrez, H. R., Gupta, A., Shen, N., ... & Zhu, J., 2010. Reversible fluorination of graphene: Evidence of a two-dimensional wide bandgap semiconductor. *Physical Review B*, *81*(20), 205435.

[48] Withers, F., Dubois, M., & Savchenko, A. K., 2010. Electron properties of fluorinated single-layer graphene transistors. *Physical Review B*, *82*(7), 073403.

[49] Zhou, S. Y., Gweon, G. H., Fedorov, A. V., First, P. D., De Heer, W. A., Lee, D. H., ... &

Lanzara, A., 2007. Substrate-induced bandgap opening in epitaxial graphene. *Nature Materials*, *6*(10), 770-775.

[50] Shemella, P., & Nayak, S. K., 2009. Electronic structure and band-gap modulation of graphene via substrate surface chemistry. *Applied Physics Letters*, *94*(3), 032101.

[51] Lee, J. K., Yamazaki, S., Yun, H., Park, J., Kennedy, G. P., Kim, G. T., ... & Roth, S., 2013. Modification of electrical properties of graphene by substrate-induced nanomodulation. *Nano letters*, *13*(8), 3494-3500.

[52] Peng, L., Xu, Z., Liu, Z., Guo, Y., Li, P., & Gao, C., 2017. Ultrahigh thermal conductive yet superflexible graphene films. *Advanced Materials*, *29*(27), 1700589.

[53] Faugeras, C., Faugeras, B., Orlita, M., Potemski, M., Nair, R. R., & Geim, A. K., 2010. Thermal conductivity of graphene in corbino membrane geometry. *ACS Nano*, *4*(4), 1889-1892.

[54] Shahil, K. M., & Balandin, A. A., 2012. Thermal properties of graphene and multilayer graphene: Applications in thermal interface materials. *Solid State Communications*, *152*(15), 1331-1340.

[55] Jagannadham, K., 2012. Thermal conductivity of copper-graphene composite films synthesized by electrochemical deposition with exfoliated graphene platelets. *Metallurgical and Materials Transactions B*, *43*(2), 316-324.

[56] Zhang, Y., & Pan, C., 2011. TiO 2/graphene composite from thermal reaction of graphene oxide and its photocatalytic activity in visible light. *Journal of Materials Science*, *46*(8), 2622-2626.

[57] Nair, R. R., Blake, P., Grigorenko, A. N., Novoselov, K. S., Booth, T. J., Stauber, T., ... & Geim, A. K., 2008. Fine structure constant defines visual transparency of graphene. *Science*, *320*(5881), 1308-1308.

[58] Kim, K. S., Zhao, Y., Jang, H., Lee, S. Y., Kim, J. M., Kim, K. S., ... & Hong, B. H., 2009. Large-scale pattern growth of graphene films for stretchable transparent electrodes. *Nature*, *457*(7230), 706-710.

[59] Hecht, D. S., Hu, L., & Irvin, G., 2011. Emerging transparent electrodes based on thin films of carbon nanotubes, graphene, and metallic nanostructures. *Advanced Materials*, *23*(13), 1482-1513.

[60] Wu, J., Becerril, H. A., Bao, Z., Liu, Z., Chen, Y., & Peumans, P., 2008. Organic solar cells with solution-processed graphene transparent electrodes. *Applied Physics Letters*, *92*(26), 237.

[61] Meng, Y., Zhao, Y., Hu, C., Cheng, H., Hu, Y., Zhang, Z., ... & Qu, L., 2013. All‐graphene core‐sheath microfibers for all‐solid‐state, stretchable fibriform supercapacitors and wearable electronic textiles. *Advanced Materials*, *25*(16), 2326-2331.

[62] Singh, E., Meyyappan, M., & Nalwa, H. S., 2017. Flexible graphene-based wearable gas and chemical sensors. *ACS Applied Materials & Interfaces*, *9*(40), 34544-34586.

[63] Karim, N., Afroj, S., Tan, S., He, P., Fernando, A., Carr, C., & Novoselov, K. S., 2017. Scalable production of graphene-based wearable e-textiles. *ACS Nano*, *11*(12), 12266-12275.

[64] Novoselov, K. S., & Neto, A. C., 2012. Two-dimensional crystals-based heterostructures:

materials with tailored properties. *Physica Scripta*, *2012*(T146), 014006.

[65] Huang, Y., Sutter, E., Shi, N. N., Zheng, J., Yang, T., Englund, D., ... & Sutter, P., 2015. Reliable exfoliation of large-area high-quality flakes of graphene and other two-dimensional materials. *ACS Nano*, *9*(11), 10612-10620.

[66] Ćirić, L., Sienkiewicz, A., Nafradi, B., Mionić, M., Magrez, A., & Forro, L., 2009. Towards electron spin resonance of mechanically exfoliated graphene. *Physica Status Solidi (b)*, *246*(11‐12), 2558-2561.

[67] Coleman, J. N., Lotya, M., O'Neill, A., Bergin, S. D., King, P. J., Khan, U., ... & Nicolosi, V., 2011. Two-dimensional nanosheets produced by liquid exfoliation of layered materials. *Science*, *331*(6017), 568-571.

[68] Coleman, J. N., 2013. Liquid exfoliation of defect-free graphene. *Accounts of Chemical Research*, *46*(1), 14-22.

[69] Keeley, G. P., O'Neill, A., McEvoy, N., Peltekis, N., Coleman, J. N., & Duesberg, G. S., 2010. Electrochemical ascorbic acid sensor based on DMF-exfoliated graphene. *Journal of Materials Chemistry*, *20*(36), 7864-7869.

[70] Sahoo, S., Hatui, G., Bhattacharya, P., Dhibar, S., & Das, C. K., 2013. One pot synthesis of graphene by exfoliation of graphite in ODCB. *Graphene*, *2*(01), 42.

[71] Xu, J., Dang, D. K., Liu, X., Chung, J. S., Hur, S. H., Choi, W. M., ... & Kohl, P. A., 2014. Liquid-phase exfoliation of graphene in organic solvents with addition of naphthalene. *Journal of Colloid and Interface Science*, *418*, 37-42.

[72] Hummers Jr, W. S., & Offeman, R. E., 1958. Preparation of graphitic oxide. *Journal of the American Chemical Society*, *80*(6), 1339-1339.

[73] Lerf, A., He, H., Forster, M., & Klinowski, J., 1998. Structure of graphite oxide revisited. *The Journal of Physical Chemistry B*, *102*(23), 4477-4482.

[74] Szabó, T., Berkesi, O., Forgó, P., Josepovits, K., Sanakis, Y., Petridis, D., & Dékány, I., 2006. Evolution of surface functional groups in a series of progressively oxidized graphite oxides. *Chemistry of Materials*, *18*(11), 2740-2749.

[75] Moon, I. K., Lee, J., Ruoff, R. S., & Lee, H., 2010. Reduced graphene oxide by chemical graphitization. *Nature Communications*, *1*(1), 1-6.

[76] De Silva, K. K. H., Huang, H. H., Joshi, R. K., & Yoshimura, M., 2017. Chemical reduction of graphene oxide using green reductants. *Carbon*, *119*, 190-199.

[77] Riley, R. F., 1963. Handbook of Preparative Inorganic Chemistry.

[78] Kaniyoor, A., Baby, T. T., Arockiadoss, T., Rajalakshmi, N., & Ramaprabhu, S., 2011. Wrinkled graphenes: a study on the effects of synthesis parameters on exfoliation-reduction of graphite oxide. *The Journal of Physical Chemistry C*, *115*(36), 17660-17669.

[79] Guo, H., Peng, M., Zhu, Z., & Sun, L., 2013. Preparation of reduced graphene oxide by infrared irradiation induced photothermal reduction. *Nanoscale*, *5*(19), 9040-9048.

[80] Mukherjee, R., Thomas, A. V., Krishnamurthy, A., & Koratkar, N., 2012. Photothermally reduced graphene as high-power anodes for lithium-ion batteries. *ACS Nano*, *6*(9), 7867-7878.

[81] Zhou, M., Wang, Y., Zhai, Y., Zhai, J., Ren, W., Wang, F., & Dong, S., 2009. Controlled synthesis of large‐area and patterned electrochemically reduced graphene oxide

films. *Chemistry–A European Journal*, *15*(25), 6116-6120.

[82] Zhou, Y., Bao, Q., Tang, L. A. L., Zhong, Y., & Loh, K. P., 2009. Hydrothermal dehydration for the “green” reduction of exfoliated graphene oxide to graphene and demonstration of tunable optical limiting properties. *Chemistry of Materials*, *21*(13), 2950-2956.

[83] Eda, G., Fanchini, G., & Chhowalla, M., 2008. Large-area ultrathin films of reduced graphene oxide as a transparent and flexible electronic material. *Nature Nanotechnology*, *3*(5), 270-274.

[84] Rowley-Neale, S. J., Randviir, E. P., Dena, A. S. A., & Banks, C. E., 2018. An overview of recent applications of reduced graphene oxide as a basis of electroanalytical sensing platforms. *Applied Materials Today*, *10*, 218-226.

[85] Smith, A. T., LaChance, A. M., Zeng, S., Liu, B., & Sun, L., 2019. Synthesis, properties, and applications of graphene oxide/reduced graphene oxide and their nanocomposites. *Nano Materials Science*, *1*(1), 31-47.

[86] Hass, J., Varchon, F., Millan-Otoya, J. E., Sprinkle, M., Sharma, N., de Heer, W. A., ... & Conrad, E. H., 2008. Why multilayer graphene on 4 H− SiC (000 1) behaves like a single sheet of graphene. *Physical Review Letters*, *100*(12), 125504.

[87] Kleykamp, H., & Schumacher, G., 1993. The constitution of the silicon-carbon system. *Berichte der Bunsengesellschaft fur Physikalische Chemie*, *97*(6), 799-804.

[88] Badami, D. V., 1965. X-Ray studies of graphite formed by decomposing silicon carbide. *Carbon*, *3*(1), 53-57.

[89] Emtsev, K. V., Bostwick, A., Horn, K., Jobst, J., Kellogg, G. L., Ley, L., ... & Seyller, T., 2009. Towards wafer-size graphene layers by atmospheric pressure graphitization of silicon carbide. *Nature Materials*, *8*(3), 203-207.

[90] Gao, M., Pan, Y., Huang, L., Hu, H., Zhang, L. Z., Guo, H. M., ... & Gao, H. J., 2011. Epitaxial growth and structural property of graphene on Pt (111). *Applied Physics Letters*, *98*(3), 033101.

[91] Sutter, P. W., Flege, J. I., & Sutter, E. A., 2008. Epitaxial graphene on ruthenium. *Nature Materials*, *7*(5), 406-411.

[92] Sutter, P., Hybertsen, M. S., Sadowski, J. T., & Sutter, E., 2009. Electronic structure of few-layer epitaxial graphene on Ru (0001). *Nano Letters*, *9*(7), 2654-2660.

[93] Eom, D., Prezzi, D., Rim, K. T., Zhou, H., Lefenfeld, M., Xiao, S., ... & Flynn, G. W., 2009. Structure and electronic properties of graphene nanoislands on Co (0001). *Nano Letters*, *9*(8), 2844-2848.

[94] Gao, L., Guest, J. R., & Guisinger, N. P., 2010. Epitaxial graphene on Cu (111). *Nano Letters*, *10*(9), 3512-3516.

[95] Kedzierski, J., Hsu, P. L., Healey, P., Wyatt, P. W., Keast, C. L., Sprinkle, M., ... & De Heer, W. A., 2008. Epitaxial graphene transistors on SiC substrates. *IEEE Transactions on Electron Devices*, *55*(8), 2078-2085.

[96] Lin, Y. M., Dimitrakopoulos, C., Jenkins, K. A., Farmer, D. B., Chiu, H. Y., Grill, A., & Avouris, P., 2010. 100-GHz transistors from wafer-scale epitaxial graphene. *Science*, *327*(5966), 662-662.

[97] Su, C. Y., Lu, A. Y., Xu, Y., Chen, F. R., Khlobystov, A. N., & Li, L. J., 2011. High-quality thin

graphene films from fast electrochemical exfoliation. *ACS Nano*, *5*(3), 2332-2339.

[98] Abdelkader, A. M., Cooper, A. J., Dryfe, R. A. W., & Kinloch, I. A., 2015. How to get between the sheets: a review of recent works on the electrochemical exfoliation of graphene materials from bulk graphite. *Nanoscale*, *7*(16), 6944-6956.

[99] Hirsch, A., 2009. Unzipping carbon nanotubes: a peeling method for the formation of graphene nanoribbons. *Angewandte Chemie International Edition*, *48*(36), 6594-6596.

[100] Memon, N. K., Stephen, D. T., Al-Sharab, J. F., Yamaguchi, H., Goncalves, A. M. B., Kear, B. H., ... & Chhowalla, M., 2011. Flame synthesis of graphene films in open environments. *Carbon*, *49*(15), 5064-5070.

[101] Peng, Z., Ye, R., Mann, J. A., Zakhidov, D., Li, Y., Smalley, P. R., ... & Tour, J. M., 2015. Flexible boron-doped laser-induced graphene microsupercapacitors. *ACS Nano*, *9*(6), 5868-5875.

[102] Peng, Z., Lin, J., Ye, R., Samuel, E. L., & Tour, J. M., 2015. Flexible and stackable laser-induced graphene supercapacitors. *ACS Applied Materials & Interfaces*, *7*(5), 3414-3419.

[103] Tiwari, S. K., Sahoo, S., Wang, N., & Huczko, A., 2020. Graphene research and their outputs: Status and prospect. *Journal of Science: Advanced Materials and Devices*, *5*(1), 10-29.

[104] Le, L. T., Ervin, M. H., Qiu, H., Fuchs, B. E., & Lee, W. Y., 2011. Graphene supercapacitor electrodes fabricated by inkjet printing and thermal reduction of graphene oxide. *Electrochemistry Communications*, *13*(4), 355-358.

[105] Wei, X., Li, D., Jiang, W., Gu, Z., Wang, X., Zhang, Z., & Sun, Z., 2015. 3D printable graphene composite. *Scientific Reports*, *5*(1), 1-7.

[106] Shi, J. L., Du, W. C., Yin, Y. X., Guo, Y. G., & Wan, L. J., 2014. Hydrothermal reduction of three-dimensional graphene oxide for binder-free flexible supercapacitors. *Journal of Materials Chemistry A*, *2*(28), 10830-10834.

[107] Xu, Y., Sheng, K., Li, C., & Shi, G., 2010. Self-assembled graphene hydrogel via a one-step hydrothermal process. *ACS Nano*, *4*(7), 4324-4330.

[108] Wicklein, B., Kocjan, A., Salazar-Alvarez, G., Carosio, F., Camino, G., Antonietti, M., & Bergström, L., 2015. Thermally insulating and fire-retardant lightweight anisotropic foams based on nanocellulose and graphene oxide. *Nature Nanotechnology*, *10*(3), 277-283.

[109] Vickery, J. L., Patil, A. J., & Mann, S., 2009. fabrication of graphene–polymer nanocomposites with higher‐order three‐dimensional architectures. *Advanced Materials*, *21*(21), 2180-2184.

[110] Li, Y., Cui, W., Liu, L., Zong, R., Yao, W., Liang, Y., & Zhu, Y., 2016. Removal of Cr (VI) by 3D TiO2-graphene hydrogel via adsorption enriched with photocatalytic reduction. *Applied Catalysis B: Environmental*, *199*, 412-423.

[111] Stankovich, S., Dikin, D. A., Piner, R. D., Kohlhaas, K. A., Kleinhammes, A., Jia, Y., ... & Ruoff, R. S., 2007. Synthesis of graphene-based nanosheets via chemical reduction of exfoliated graphite oxide. *Carbon*, *45*(7), 1558-1565.

[112] Chen, Z., Ren, W., Gao, L., Liu, B., Pei, S., & Cheng, H. M., 2011. Three-dimensional flexible and conductive interconnected graphene networks grown by chemical vapour deposition. *Nature Materials*, *10*(6), 424-428.

[113] Shi, J. L., Tang, C., Peng, H. J., Zhu, L., Cheng, X. B., Huang, J. Q., ... & Zhang, Q., 2015. 3D Mesoporous Graphene: CVD Self-Assembly on Porous Oxide Templates and Applications in High‐Stable Li‐S Batteries. *Small*, *11*(39), 5243-5252.

[114] Yang, C., Bi, H., Wan, D., Huang, F., Xie, X., & Jiang, M., 2013. Direct PECVD growth of vertically erected graphene walls on dielectric substrates as excellent multifunctional electrodes. *Journal of Materials Chemistry A*, *1*(3), 770-775.

[115] Chen, K., Shi, L., Zhang, Y., & Liu, Z. 2018. Scalable chemical-vapour-deposition growth of three-dimensional graphene materials towards energy-related applications. *Chemical Society Reviews*, *47*(9), 3018-3036.

[116] Lin, J., Peng, Z., Liu, Y., Ruiz-Zepeda, F., Ye, R., Samuel, E. L., ... & Tour, J. M., 2014. Laser-induced porous graphene films from commercial polymers. *Nature Communications*, *5*(1), 1-8.

[117] Song, W., Zhu, J., Gan, B., Zhao, S., Wang, H., Li, C., & Wang, J., 2018. Flexible, stretchable, and transparent planar microsupercapacitors based on 3D porous laser‐induced graphene. *Small*, *14*(1), 1702249.

[118] Shan, C., Tang, H., Wong, T., He, L., & Lee, S. T., 2012. Facile synthesis of a large quantity of graphene by chemical vapor deposition: an advanced catalyst carrier. *Advanced Materials*, *24*(18), 2491-2495.

[119] Yoon, J. C., Lee, J. S., Kim, S. I., Kim, K. H., & Jang, J. H., 2013. Three-dimensional graphene nano-networks with high quality and mass production capability via precursor-assisted chemical vapor deposition. *Scientific Reports*, *3*(1), 1-8.

[120] Gong, C., Lee, G., Shan, B., Vogel, E. M., Wallace, R. M., & Cho, K., 2010. First-principles study of metal–graphene interfaces. *Journal of Applied Physics*, *108*(12), 123711.

[121] Batzill, M., 2012. The surface science of graphene: Metal interfaces, CVD synthesis, nanoribbons, chemical modifications, and defects. *Surface Science Reports*, *67*(3-4), 83-115.

[122] Al-Shurman, K. M., & Naseem, H., 2014. CVD Graphene growth mechanism on nickel thin films. In *Proceedings of the 2014 COMSOL Conference, Boston, MA* (p. 7).

[123] Pan, Y., Zhang, H., Shi, D., Sun, J., Du, S., Liu, F., & Gao, H. J., 2009. Highly ordered, millimeter‐scale, continuous, single‐crystalline graphene monolayer formed on Ru (0001). *Advanced Materials*, *21*(27), 2777-2780.

[124] Miniussi, E., Pozzo, M., Baraldi, A., Vesselli, E., Zhan, R.R., Comelli, G., Menteş, T.O., Niño, M.A., Locatelli, A., Lizzit, S. and Alfè, D., 2011. Thermal stability of corrugated epitaxial graphene grown on Re (0001). *Physical Review Letters*, *106*(21), p.216101.

[125] Sicot, M., Bouvron, S., Zander, O., Rüdiger, U., Dedkov, Y. S., & Fonin, M., 2010. Nucleation and growth of nickel nanoclusters on graphene Moiré on Rh (111). *Applied Physics Letters*, *96*(9), 093115.

[126] Mattevi, C., Kim, H., & Chhowalla, M., 2011. A review of chemical vapour deposition of graphene on copper. *Journal of Materials Chemistry*, *21*(10), 3324-3334.

[127] Yu, Q., Jauregui, L. A., Wu, W., Colby, R., Tian, J., Su, Z., ... & Chen, Y. P., 2011. Control and characterization of individual grains and grain boundaries in graphene grown by chemical vapour deposition. *Nature Materials*, *10*(6), 443-449.

[128] Coraux, J., Engler, M., Busse, C., Wall, D., Buckanie, N., Zu Heringdorf, F. J. M., ... & Michely, T., 2009. Growth of graphene on Ir (111). *New Journal of Physics*, *11*(2), 023006.

[129] Wofford, J. M., Starodub, E., Walter, A. L., Nie, S., Bostwick, A., Bartelt, N. C., ... & Dubon, O. D., 2012. Extraordinary epitaxial alignment of graphene islands on Au (111). *New Journal of Physics*, *14*(5), 053008.

[130] Novoselov, K. S., Fal, V. I., Colombo, L., Gellert, P. R., Schwab, M. G., & Kim, K., 2012. A roadmap for graphene. *Nature*, *490*(7419), 192-200.

[131] Chen, T. Y., Loan, P. T. K., Hsu, C. L., Lee, Y. H., Wang, J. T. W., Wei, K. H., ... & Li, L. J., 2013. Label-free detection of DNA hybridization using transistors based on CVD grown graphene. *Biosensors and Bioelectronics*, *41*, 103-109.

[132] Valmorra, F., Scalari, G., Maissen, C., Fu, W., Schönenberger, C., Choi, J. W., ... & Faist, J., 2013. Low-bias active control of terahertz waves by coupling large-area CVD graphene to a terahertz metamaterial. *Nano Letters*, *13*(7), 3193-3198.

[133] Schwierz, F., 2011. Industry-compatible graphene transistors. *Nature*, *472*(7341), 41-42.

[134] Sun, Z., Yan, Z., Yao, J., Beitler, E., Zhu, Y., & Tour, J. M., 2010. Growth of graphene from solid carbon sources. *Nature*, *468*(7323), 549-552.

[135] Sha, J., Gao, C., Lee, S. K., Li, Y., Zhao, N., & Tour, J. M., 2016. Preparation of three-dimensional graphene foams using powder metallurgy templates. *ACS Nano*, *10*(1), 1411-1416.

[136] Li, J., Zhang, L., Zhang, L., Hao, W., Wang, H., Qu, Q., & Zheng, H., 2014. In-situ growth of graphene decorations for high-performance $LiFePO_4$ cathode through solid-state reaction. *Journal of Power Sources*, *249*, 311-319.

[137] Alnuaimi, A., Almansouri, I., Saadat, I., & Nayfeh, A., 2017. Toward fast growth of large area high quality graphene using a cold-wall CVD reactor. *RSC Advances*, *7*(82), 51951-51957.

[138] Kwak, J., Kwon, T. Y., Chu, J. H., Choi, J. K., Lee, M. S., Kim, S. Y., ... & Kwon, S. Y., 2013. In situ observations of gas phase dynamics during graphene growth using solid-state carbon sources. *Physical Chemistry Chemical Physics*, *15*(25), 10446-10452.

[139] Malard, L. M., Pimenta, M. A., Dresselhaus, G., & Dresselhaus, M. S., 2009. Raman spectroscopy in graphene. *Physics Reports*, *473*(5-6), 51-87.

[140] Cançado, L. G., Jorio, A., Ferreira, E. M., Stavale, F., Achete, C. A., Capaz, R. B., ... & Ferrari, A. C., 2011. Quantifying defects in graphene via Raman spectroscopy at different excitation energies. *Nano Letters*, *11*(8), 3190-3196.

[141] Moynihan, C. T., Easteal, A. J., Wilder, J., & Tucker, J., 1974. Dependence of the glass transition temperature on heating and cooling rate. *The Journal of Physical Chemistry*, *78*(26), 2673-2677.

[142] Kasap, S., Khaksaran, H., Çelik, S., Özkaya, H., Yanık, C., & Kaya, I. I., 2015. Controlled growth of large area multilayer graphene on copper by chemical vapour deposition. *Physical Chemistry Chemical Physics*, *17*(35), 23081-23087.

[143] Lin, T., Wang, Y., Bi, H., Wan, D., Huang, F., Xie, X., & Jiang, M., 2012. Hydrogen flame synthesis of few-layer graphene from a solid carbon source on hexagonal boron nitride. *Journal of Materials Chemistry*, *22*(7), 2859-2862.

Chapter 3 Materials and methods

3.1 Materials selection

Solid carbon sources chosen in this study are glucose (Sigma-Aldrich, Gillingham, UK) and polyacrylonitrile (PAN, average molecular weight: 150,000, Sigma-Aldrich, Gillingham, UK). The key parameters and purity levels are summarised in **Table 3.1**.

Table 3.1. Solid carbon sources investigated in the preparation of graphene growth.

Name	Molecular Formula	Key parameters	Purity
D–(+)-Glucose	$C_6H_{12}O_6$	Decomposes at about 300 °C	≥ 99.50%
Polyacrylonitrile (PAN)	$(C_3H_3N)_n$	Tg: 85 °C, Melting temperature: 317 °C	

Iron-based salts have been chosen to be the metal precursors in the first experiment, as their salts are usually inexpensive and available in many laboratories. Besides, the by-products of the reactions are more predictable, and they are easier to remove than other metals, such as the nickel used in Sha's group [1]. Furthermore, iron is also metal in the "nickel system", as carbon has a high solubility in iron.

Table 3.2. Iron salts as metal catalysts investigated in the preparation of graphene growth.

Name	Molecular Formula	Key parameters	Purity
Iron(II) chloride	$FeCl_2$	Decomposes at about 500 °C	98.00%
Iron(III) chloride	$FeCl_3$	Boiling point: 315 °C	97%
Iron(II) sulfate heptahydrate	$FeSO_4 \cdot 7H_2O$	Decomposes at about 680 °C	>99.9%

Details of the metal catalysts tested in this study, including Iron (II) chloride, Iron (III)

chloride and Iron (II) sulfate heptahydrate (all bought from Sigma-Aldrich, Gillingham, UK), are listed in **Table 3.2**.

Deionised water was the solvent chosen in 2D/3D graphene syntheses with glucose and $FeCl_3$ as these two starting materials are both water-soluble. However, when it comes to PAN, it has negligible solubility in water, and thus an organic solvent is required to mix PAN with the catalysts. Since PAN usually has better solubility in the organic solvent than in water, a solubility test was performed in the second study to find the suitable organic solvent for PAN. In fact, the choice of organic solvents can provide more options for this graphene fabrication technique since there is a wide range of polymers that exhibit various characteristics. With appropriate structures and chemical properties, some of them can be good candidates for the solid carbon sources in the catalytic graphitisation technique. All solvents that have been tested, including acetone (Fisher Scientific UK Ltd), chloroform (Sigma-Aldrich, Gillingham, UK), anisole (Sigma-Aldrich, Gillingham, UK) and DMF (Fisher Scientific UK Ltd), are listed in **Table 3.3**.

Table 3.3. Solvents for carbon sources and metal catalysts investigated in the preparation of graphene growth.

Name	Molecular Formula	Key parameters	Purity
Acetone	C_3H_6O	Boiling point: 56.05°C	99.00%
Chloroform	$CHCl_3$	Boiling point: 61.2 °C	>99.5%
Anisole	C_7H_8O	Boiling point: 153.8 °C	99.00%
Dimethylformamide (DMF)	$HCON(CH_3)_2$	Boiling point: 153 °C	99.00%

3.2 Characterisation and sample preparation methods

This section will review the characterisation methods adopted in this research and introduce the working principles for each method in detail. Morphological information of the samples was gathered through microscopy, including Scanning electron microscope (SEM) and Transmission electron microscope (TEM). Structural and chemical properties of the products were examined using techniques that mainly employ the loss or shift of energy in incident beams, such as Energy-dispersive X-ray spectroscopy (EDS), Fourier-transform infrared spectroscopy (FTIR), Raman spectroscopy and X-ray photoelectron spectroscopy (XPS). Other than these, X-ray diffraction (XRD) was used to characterise the crystal structure of the synthesised graphene, and Brunauer-Emmett-Teller (BET) surface area analysis was also carried out to measure the surface areas of the porous graphene foams.

Different techniques may have different requirements for their sample preparation, which will also be discussed in this section. It is also worth noticing that both 2D and 3D graphene were synthesised in our work. That has made more characterisation methods applicable to our samples. For instance, FTIR and BET analyses are not usually applicable to thin 2D graphene films grown on silicon wafers since they both require a sufficient amount of powdered samples, preferably. Nevertheless, 2D graphene is more suitable for characterisation techniques that prefer flat surfaces like Raman spectroscopy and SEM. Furthermore, 2D graphene is also a suitable medium through which the internal structure of 3D graphene can be studied.

3.2.1 Scanning electron microscopy (SEM)

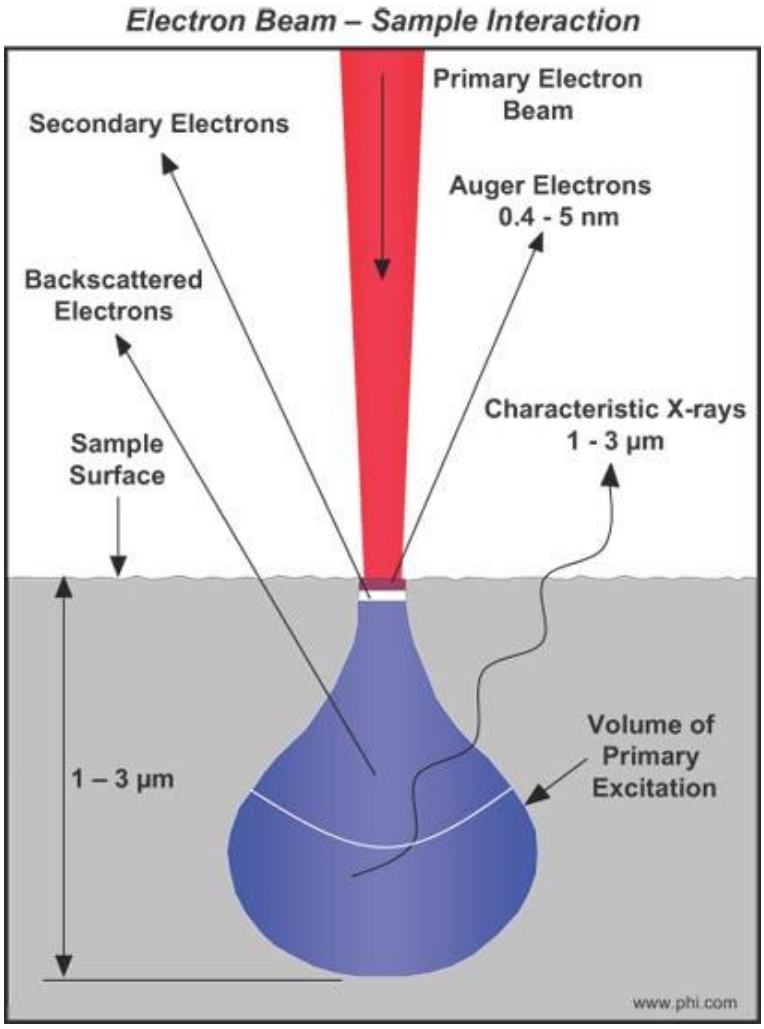

Figure 3.1. Types of electrons generated from different depths from sample surface by scanning electron beam [2].

SEM is a useful technique to examine the morphology and chemical composition of solid samples. It provides high-resolution images of samples by scanning a focused electron beam across the sample surfaces and collecting signals mainly of the bounced back secondary electrons and backscattered electrons 5nm - 300nm away from the sample surfaces, as illustrated in **Figure 3.1**.

The secondary electrons generated right at the sample surfaces exhibit low energy but high resolution. The intensity depends on the curvature as more electrons will be

emitted at prominent locations with increased reaction volume. As a result, edges will appear brighter than the flat surfaces, providing a 3-dimensional presentation of the sample surface. Therefore, signals of secondary electrons are mainly used in surface topography imaging.

In the meanwhile, backscattered electrons are mainly used in chemical analysis. Backscattered electron signals are generated from incident electrons reflected straight back after elastic scattering reaction with the specimen atoms at a deeper region. Heavier specimen atoms can reflect more electrons than lighter atoms, thus contrasting regions with different chemical compositions.

In this project, Zeiss Ultra 55 SEM (Germany) and FEI/Philips XL30 SEM (U.S.A) were used to characterise the surface structures of metal catalysts, spin-coated reactant layers, 2D graphene grown on the silicon substrates before and after being washed with acids, and 3D graphene scaffold fabricated before and after cleansing. The working distance was set to be around 8-10 mm, with the electron high tension voltage set to be between 1.5 kV - 3 kV for Ultra 55 and 8 kV - 10 kV for FEI/Philips XL30.

The sample preparation procedures differed a little for 2D graphene and 3D graphene.

2D graphene layers were grown on a flat silicon wafer. Together with the wafer, the products were fixed to SEM specimen stubs via conductive carbon tapes and sent for a first-round SEM analysis without further treatment. Residues of metal catalysts were spotted in the images. Since SEM analysis is non-destructive, the tested samples were taken off the conductive tapes and cleaned in an ultrasonic cleaner with 20 ml of 20% hydrochloric acid for an hour. Some thin graphene films had fallen off the silicon wafer and had dispersed in the solution during the cleaning, exposing a larger surface to the acid, resulting in a more efficient purification. The acidic solution was then replaced by deionised water in the process of filtering. A droplet of the graphene-water solution was deposited onto a new piece of silicon wafer, followed by evaporation of liquid in

an oven kept at 60 °C. After the removal of metal residues, samples were sent for a second-round SEM analysis.

In the first-round SEM analysis for 3D graphene, the foams and some scraps falling off the foams were directly stuck onto the carbon adhesive tapes before metal catalysts or salts were removed. No coating with gold or platinum was needed as the graphene foams exhibited excellent conductivity. Unlike graphene films, Ultrasonication cannot always be performed with 3D graphene foams during the washing step since some of the 3D structures obtained were pretty fragile and would break when external forces are applied. So instead, the foams were soaked in acidic solutions (details are to be presented in the next chapter). After further cleaning with deionised water and drying in the oven, samples were ready for the second-round SEM analysis.

3.2.2 Transmission electron microscopy (TEM)

TEM is a powerful analytical tool in which a high energy electron beam transmits through a thin sample, whose thickness is typically below 100 nm, in order to capture high-resolution images.

TEM is similar to SEM in the way that they both make use of high energy electrons instead of light to attain high-resolution images. The main difference between these two techniques is that TEM collects signals of electrons transmitted through specimens while SEM creates images by collecting reflected electrons. TEM mainly supports investigation of material's inner structure and crystallinity while information on surface topography and composition is generally obtained via SEM.

In this work, morphology and inner structures of 2D/3D graphene were characterised by Philips CM20 TEM (U.S.A), FEI/ Tecnai F20 TEM (U.S.A) and FEI/ Tecnai F20 TEM (U.S.A). CM 20 and Tecnai F20 are both installed with 200kV field emission electron guns, while a 300kV electron gun is installed inside Tecnai F30. A 300 kV high tension offers better coherence and higher brightness, thus delivering higher resolution. However, such an intense electron beam may deteriorate the structure in the thin specimen due to electron irradiation [3].

Metal residues were removed before the TEM sample preparation. For 2D graphene flakes, after ultrasonicated and washed with deionised water, graphene suspensions were deposited onto silicon wafers for SEM sample preparations. The suspensions were also deposited onto lacey carbon films on 400 mesh copper grids, which were bought from Agar Scientific (UK) for TEM sample preparations at the same time.

In the case of 3D graphene foams, since their dimensions did not meet the requirement for TEM specimen preparation, scraps that naturally fell off the foams were collected and washed with acid before being deposited on copper grids.

All the grids were oven-dried at 60 °C before TEM tests were carried out.

3.2.3 Energy-dispersive X-ray spectroscopy (EDS)

EDS is an elemental analysis technique widely used to identify a material's chemical composition in a scanned area. The principle is illustrated in **Figure 3.2**. The focused electron beam scanning across the area may hit an electron in the inner shell of an atom, knocking the electron off from its shell, leaving a hole behind. Electrons in an outer shell will tend to fill the hole in the inner shell to achieve a lower-energy state, releasing an X-ray which will then be collected and measured by the EDS detector. Such X-ray reflects the energy difference between the two shells and has a unique value for each element. By calculation, EDS can also provide users with the weight and atomic percentages of each element detected in the scanned region. [4]

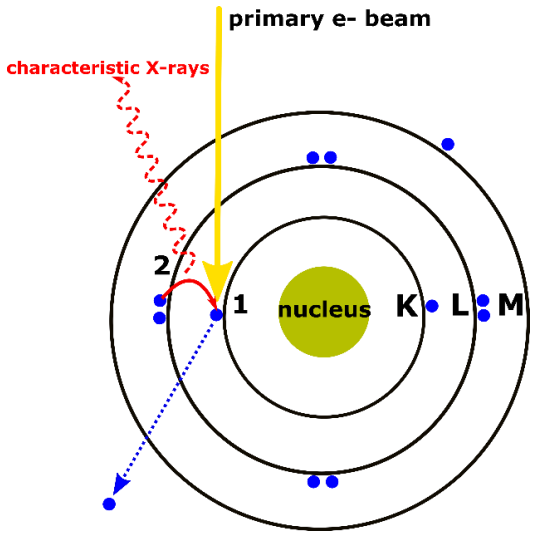

Figure 3.2. Principle of EDS spectroscopy [5]. The primary electron beam ejects the low-energy state electron 1 in the inner shell of an atom. The high-energy state electron 2 fills the hole left by electron 1 and releases characteristic rays.

The EDS system used in our work is integrated into the Zeiss Ultra 55 SEM instrument. Thus, the EDS analysis can be conducted along with the SEM analysis, and it needs no further sample preparation. The sensitive X-ray detector is mounted in the SEM sample chamber with continuous liquid nitrogen cooling.

It is worth noticing that EDS is also regarded as a non-destructive analytical technique since it only affects a small number of atoms compared to the bulk. Therefore, the same sample can be analysed repeatedly and used for further treatments or other tests after EDS analysis.

3.2.4 Fourier-transform infrared spectroscopy (FTIR)

FTIR is a technique used to detect the chemical functional groups in materials by recording an infrared spectrum of radiation absorbed or emitted by materials in any state.

Chemical bonds in materials will extend, contract or vibrate when the infrared light interacts with the samples. In addition, different bonds will absorb infrared radiation at different wavenumber ranges. As a result, this technique can be used to identify the chemical bonds in samples [6].

The equipment used for FTIR characterisation in this work is Thermo Fisher Scientific Nicolet 5700 spectrophotometer (UK).

Since the samples are all black, infrared light can hardly penetrate them. Therefore, almost no signal can be detected when the powdered samples are directly measured. Therefore, the potassium bromide (KBr) pellet method was adopted. Around 0.1mg of graphene powder sample was well mixed with 300mg of dried KBr. The powder mixture was then finely pulverised and cold-pressed into a pellet under a force of approximately 7 tons for around 5 minutes. The pellet was then placed in the centre of the infrared chamber and scanned over a range from 400 to 4000 cm^{-1}. A spectral resolution of 4 cm^{-1} was achieved by averaging 64 scans. However, KBr tends to absorb water from the atmosphere promptly. Hence, it would give rise to a broad band for O-H, which will interfere with the peaks of interest.

3.2.5 Raman Spectroscopy

Raman spectroscopy is another powerful non-destructive analytical technique that is widely utilised in the characterisation of graphene-related materials. The laser beam used as the light source in Raman spectroscopy is intense and exhibits monochromatism, so it can strongly interact with specimen molecules. The incident laser beam will interact with lattice phonons and molecular vibrations in a material, causing a shift of laser photon energy to the left or to the right in spectra. The shifts are characteristic and can provide various kinds of information about graphene in terms of structures [7, 8], defects [9, 10], crystallographic disorders [11, 12] and states of oxidation [13, 14], etc.

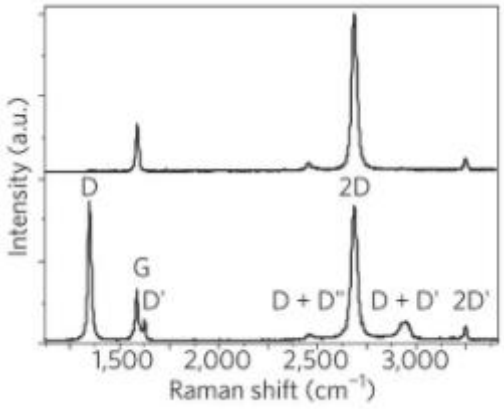

Figure 3.3. Typical Raman spectra of observed defect-free single-layer graphene (top) and defected graphene (bottom) [15].

Spectra in **Figure 3.3** displayed the typical bands generally observed in pristine and defected single-layer graphene. From left to right:

D band around 1350 cm^{-1} corresponds to the breathing mode of sp^2 aromatic rings. It only appears with the presence of defects (e.g. vacancies or impurity atoms) or edges (e.g. grain boundaries or the edges of graphene flakes) [16]. The D band in graphene oxide, for instance, rises from its oxidative functional groups,

while the presence of the D band in reduced graphene oxide is primarily due to vacancies left in the plane after the removal of oxidative functional groups. The intensities of the D band and the intensity ratio I_D/I_G are extensively used to measure graphene quality. In pristine graphene, the ideal value for I_D should be 0. The ratio I_D/I_G increases when the defect density in graphene increases.

G band around 1580 cm^{-1} is related to in-plane vibrations of sp^2 carbons. The G peak corresponds with a high-frequency E_{2g} mode, where carbon atoms move within the graphene plane.

D' band around 1620 cm^{-1} appears when intra-valley double resonance occurs. The peak is relatively weak and will merge with the G band when defect density is high.

2D band around 2700 cm^{-1} is a D peak overtone. This peak is generated in two-phonon processes where two phonons of opposite wave vectors are involved in conserving the total momentum in an isolated system [17]. Usually, a sharp 2D peak can be used to identify the stacking order in graphitic materials [18] and the number of layers in graphene [17]. **Figure 3.4** compared the Raman spectra obtained from graphene of different number of layers produced via CVD on SiO_2/Si substrates and micro-cleaving of HOPG. As the number of layers increased, G peaks became more prominent than the G' (2D) peaks. Broadening and up-shifts of 2D peaks can also be observed as the graphene thickness increases. The ideal I_G/I_{2D} ratio for monolayer graphene is 0.5.

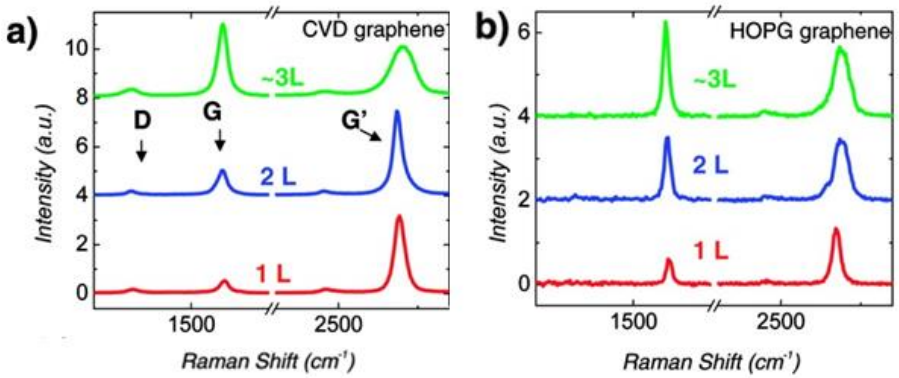

Figure 3.4. Raman spectra of mono-, bi- and tri-layer graphene obtained via (a) CVD on SiO_2/Si substrates and (b) mechanical exfoliation of HOPG [19].

In this work, the structural and electronic characterisations of 2D/3D graphene were carried out on Renishaw 1000 Raman Microscope (UK) equipped with a 514 nm Cobalt diode laser source. Raman spectroscopy tests can be conducted on the same samples prior to or after the SEM tests. Therefore, no further treatment or coating is needed for both tests. At least ten different locations on each graphene sample were examined.

3.2.6 X-ray diffraction (XRD)

XRD enables a quick crystal structure determination [20, 21] and materials' phase identification [22]. The technique works based on Bragg's law described in **Figure 3.5**.

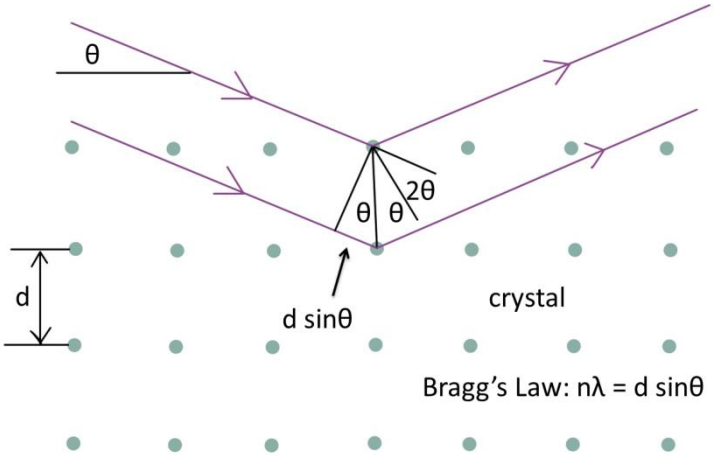

Figure 3.5. X-ray diffraction at Bragg angle θ upon crystal lattice.

Two parallel beams of X-rays reflected by crystal lattice will add up constructively in certain directions to form a diffraction pattern. The direction is associated with the lattice spacing in Bragg's equation:

$$n\lambda = d\ sin\theta;$$

where n is a whole number; λ is the wavelength of incident X-ray; d is the lattice spacing of the tested crystal, and θ is the angle between the crystal plane and the incident X-ray.

Lattice spacing varies from crystal to crystal, thus making the diffraction pattern characteristic. Consequently, by recording the intensities of reflected rays and the corresponding scattering angles, types of crystals can be quickly identified.

The crystal structures of produced 2D/3D graphene were characterised by a Bruker 8 Discover powder diffractometer (U.S.A) with Cu-$K_{\alpha 1}$ radiation. Diffraction profiles were

recorded from 5° to 90° with a step size of 0.02°.

Since this technique requires a traceable amount of powder form samples, only 3D graphene foams were submitted for XRD analysis. 3D graphene foams were intentionally pulverised into fine powders and then attached to the substrates with a smear of Vaseline prior to the analysis.

3.2.7 X-ray photoelectron spectroscopy (XPS)

XPS is a surface-sensitive technique that can be utilised in chemical composition analyses of graphene-related materials [23-25].

The source for non-monochromatic X-rays is usually Aluminium (Al). Similar to EDS, the working principle of XPS also involves ejections of electrons, in this case, from the K shell, followed by an occupation of holes in the K shell by electrons in higher-energy shells. Excessive energy is released as kinetic energies of photoelectrons and can be detected and recorded by an electron energy analyser. The chemical-state-dependent binding energy (BE) of a photoelectron is related to the incident X-ray as well as the measured photoelectron kinetic energy (KE) by a simple equation:

$$BE = h\upsilon - KE - \phi$$

where BE stands for the binding energy of the electron; h is Planck's constant; ν is the frequency of photons; hν stands for the energy of the incident X-ray photons; KE stands for the kinetic energy of electrons detected by the spectrometer, and ϕ stands for the work function of the instrument which can be adjusted as a correction factor.

In our work, Kratos Axis Ultra DLD X-ray photoelectron spectrometer (UK) was used to determine the chemical bonds in the fabricated graphene. In this spectrometer, monochromated Al Kα acted as the X-ray source. The corresponding X-ray photon energy (hν) was 1486.6 eV. The filament current, which decides the number of bombarding electrons, was set to 10 mA, while the voltage applied was set to 15 kV. Besides, the ultrahigh vacuum chamber was kept under a base pressure below 5×10^{-8} millibar (mbar). Samples prepared by suspension deposition on silicon wafers were directly submitted for XPS analysis.

3.2.8 Brunauer-Emmett-Teller (BET) surface area analysis

BET is a powerful tool in determining the surface areas and pore structures of solids.

The specific area of a powder form sample can be determined at an atomic level by calculating the volume of unreactive gas, usually being nitrogen, physically absorbed on the solid surfaces relative to the mass of the sample [26].

In our project, the BET isotherm model was adopted rather than the Langmuir isotherm model. The key difference is that Langmuir isotherm describes the monolayer formation of gas molecules on top of the absorbent surface, whereas BET isotherm describes a multilayer molecule adsorption behaviour. As a result, the former model will tend to exaggerate the measured solid's surface area when multilayers are formed.

During the test, pressure in the sample loaded tube is increased with an increasing amount of gas absorbed on the surface. The relationship between the number of gas molecules absorbed on accessible surfaces and the relative pressure is described by the BET equation:

$$\frac{1}{V_a(\frac{P_0}{P}-1)} = \frac{C-1}{V_m C} \times \frac{P_0}{P} + \frac{1}{V_m C}$$

where V_a is the volume of gas absorbed under standard conditions; P/P_0 is the relative pressure of the adsorbate gas; V_m stands for the volume of gas needed to form a monolayer of gas on all solid surfaces, and C is a dimensionless constant.

The density functional theory (DFT) was used to analyse the pore size distribution in graphene flakes. The model is based upon the entire molecule absorption process, which involves the adsorbate-adsorbent interaction, pore-filling and film formation of the absorbed gas. Therefore, it provides a more accurate approximation to the actual

pore size distribution than the Barrett-Joyner-Halenda (BJH) method, which relates the radius of curvatures in a sample to the pressure. The BJH method works fine for large mesopores when approximating their sizes according to the curvature information, but the error will become very significant for smaller mesopores and micropores.

BET tests were performed on Quantachrome Autosorb Gas Sorption Analyser (U.S.A). The powder samples were prepared by pulverising the 3D graphene foams. In order to remove as many impurities from the powders as possible, powders were further washed in acidic solution and deionised water with ultrasonication prior to the BET measurement. The remaining weight of each washed powder sample is around 0.5 grams. Empty test tubes were first rinsed with ethanol and dried before being weighed using an analytical balance. Then, using a long spatula, powdered samples were delivered to the bottom of the tilted test tubes without contacting the tube surfaces. The weights of loaded powders can be calculated from the differences in test tube weights before and after the samples were loaded. Samples in tubes were then placed in degasser and treated with a cold flow of nitrogen overnight. After degassing, samples were transferred to the BET test chamber and supplied with sufficient liquid nitrogen prior to the absorption-desorption test.

References

[1] Sha, J., Gao, C., Lee, S. K., Li, Y., Zhao, N., & Tour, J. M., 2016. Preparation of three-dimensional graphene foams using powder metallurgy templates. *ACS Nano*, *10*(1), 1411-1416.

[2] Understanding Depth of Analysis, 2013. Available at: https://rockymountainlaboratory.wordpress.com/2013/09/27/understanding-depth-of-analysis/

[3] Hashimoto, A., Suenaga, K., Gloter, A., Urita, K., & Iijima, S., 2004. Direct evidence for atomic defects in graphene layers. *Nature*, *430*(7002), 870-873.

[4] Goldstein, J. I., Newbury, D. E., Michael, J. R., Ritchie, N. W., Scott, J. H. J., & Joy, D. C., 2017. *Scanning electron microscopy and X-ray microanalysis*. Springer.

[5] Nanakoudis, A., *EDX Analysis with SEM: How Does it Work?*. Available at: https://www.thermofisher.com/blog/microscopy/edx-analysis-with-sem-how-does-it-work/

[6] Griffiths, P. R., & De Haseth, J. A., 2007. *Fourier Transform Infrared Spectrometry* (Vol. 171). John Wiley & Sons.

[7] Dresselhaus, M. S., Jorio, A., Hofmann, M., Dresselhaus, G., & Saito, R., 2010. Perspectives on carbon nanotubes and graphene Raman spectroscopy. *Nano Letters*, *10*(3), 751-758.

[8] Ni, Z., Wang, Y., Yu, T., & Shen, Z., 2008. Raman spectroscopy and imaging of graphene. *Nano Research*, *1*(4), 273-291.

[9] Eckmann, A., Felten, A., Mishchenko, A., Britnell, L., Krupke, R., Novoselov, K. S., & Casiraghi, C., 2012. Probing the nature of defects in graphene by Raman spectroscopy. *Nano Letters*, *12*(8), 3925-3930.

[10] Cançado, L. G., Jorio, A., Ferreira, E. M., Stavale, F., Achete, C. A., Capaz, R. B., ... & Ferrari, A. C., 2011. Quantifying defects in graphene via Raman spectroscopy at different excitation energies. *Nano Letters*, *11*(8), 3190-3196.

[11] Mohiuddin, T. M. G., Lombardo, A., Nair, R. R., Bonetti, A., Savini, G., Jalil, R., ... & Ferrari, A. C., 2009. Uniaxial strain in graphene by Raman spectroscopy: G peak splitting, Grüneisen parameters, and sample orientation. *Physical Review B*, *79*(20), 205433.

[12] Gouadec, G., & Colomban, P., 2007. Raman Spectroscopy of nanomaterials: How spectra relate to disorder, particle size and mechanical properties. *Progress in Crystal Growth and Characterization of Materials*, *53*(1), 1-56.

[13] Kaniyoor, A., & Ramaprabhu, S., 2012. A Raman spectroscopic investigation of graphite oxide derived graphene. *Aip Advances*, *2*(3), 032183.

[14] Yang, D., Velamakanni, A., Bozoklu, G., Park, S., Stoller, M., Piner, R. D., ... & Ruoff, R. S., 2009. Chemical analysis of graphene oxide films after heat and chemical treatments by X-ray photoelectron and Micro-Raman spectroscopy. *Carbon*, *47*(1), 145-152.

[15] Ferrari, A. C., & Basko, D. M., 2013. Raman spectroscopy as a versatile tool for studying the properties of graphene. *Nature Nanotechnology*, *8*(4), 235-246.

[16] Ferrari, A. C., & Robertson, J., 2000. Interpretation of Raman spectra of disordered and amorphous carbon. *Physical Review B*, *61*(20), 14095.

[17] Ferrari, A. C., Meyer, J. C., Scardaci, V., Casiraghi, C., Lazzeri, M., Mauri, F., ... & Geim, A. K., 2006. Raman spectrum of graphene and graphene layers. *Physical Review Letters*, *97*(18), 187401.

[18] Lui, C. H., Li, Z., Chen, Z., Klimov, P. V., Brus, L. E., & Heinz, T. F., 2011. Imaging stacking order in few-layer graphene. *Nano Letters*, *11*(1), 164-169.

[19] Reina, A., Jia, X., Ho, J., Nezich, D., Son, H., Bulovic, V., ... & Kong, J., 2009. Large area, few-layer graphene films on arbitrary substrates by chemical vapor deposition. *Nano Letters*, *9*(1), 30-35.

[20] Kabsch, W., 1988. Evaluation of single-crystal X-ray diffraction data from a position-sensitive detector. *Journal of Applied Crystallography*, *21*(6), 916-924.

[21] Warren, B. E., 1990. *X-ray Diffraction*. Courier Corporation.

[22] Dickson, M. J., 1969. The significance of texture parameters in phase analysis by X-ray diffraction. *Journal of Applied Crystallography*, *2*(4), 176-180.

[23] Yang, D., Velamakanni, A., Bozoklu, G., Park, S., Stoller, M., Piner, R. D., ... & Ruoff, R. S., 2009. Chemical analysis of graphene oxide films after heat and chemical treatments by X-ray photoelectron and Micro-Raman spectroscopy. *Carbon*, *47*(1), 145-152.

[24] Fan, Z., Wang, K., Wei, T., Yan, J., Song, L., & Shao, B., 2010. An environmentally friendly and efficient route for the reduction of graphene oxide by aluminum powder. *Carbon*, *48*(5), 1686-1689.

[25] Lin, W. H., Chen, T. H., Chang, J. K., Taur, J. I., Lo, Y. Y., Lee, W. L., ... & Wu, C. I., 2014. A direct and polymer-free method for transferring graphene grown by chemical vapor deposition to any substrate. *ACS Nano*, *8*(2), 1784-1791.

[26] Brunauer, S., Emmett, P. H., & Teller, E., 1938. Adsorption of gases in multimolecular layers. *Journal of the American Chemical Society*, *60*(2), 309-319.

Chapter 4 Growing graphene with ferric chloride ($FeCl_3$) and glucose

4.1 Introduction

As was mentioned in Chapter 2, there are plenty of solid carbon sources and metal/metal salts available to choose from as the starting materials for graphene synthesis. Among these, materials that are cheap, non-hazardous, and with easy access are preferred.

The graphene growth mechanism with the assist of metal catalysts often involves carbon-metal interactions at the surfaces of contact. Therefore, solid carbon sources were usually dissolved in various solvents and mixed with solid metal particles by stir-mixing to achieve a larger carbon-metal contact area. However, agglomerations of metal particles were still frequently observed, causing inhomogeneity in the quality of graphene grown at different locations, impairing the overall electrical and thermal conducting performance of produced graphene.

Compared with pure metal catalysts, metal salts can dissolve more easily in various organic or inorganic solvents, which have provided a promising catalyst option for the syntheses of graphene via catalytic graphitisation with solid carbon sources. Therefore, in the first attempt of our study, glucose was chosen as the solid carbon source, while $FeCl_3$ was chosen as the metal salt catalyst. Diagram of chemical compositions of glucose and $FeCl_3$ are shown in **Figure 4.1**.

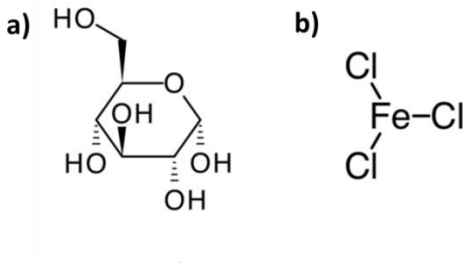

Figure 4.1. Chemical compositions of a) glucose and b) $FeCl_3$.

Glucose and $FeCl_3$ are both common lab chemicals, very low in price, non-hazardous and soluble in water, which means homogeneous mixing of these two chemicals is easy to achieve. Besides, the main by-products of the reactions are predicted to be iron or iron oxides. Iron is a very reactive metal and tends to react with dilute hydrochloric acid following the chemical equations below:

$$Fe(s) + 2HCl(aq) \rightarrow FeCl_2(aq) + H_2(g);$$

$$Fe_3O_4(s) + 8HCl(aq) \rightarrow 4H_2O(l) + FeCl_2(aq) + 2FeCl_3(aq);$$

$$FeO(s) + 2HCl(aq) \rightarrow H_2O(l) + FeCl_2(aq).$$

These reactions can turn all the solid iron by-products into an aqueous form, making the removal of solid iron residues feasible with dilute Hydrogen chloride (HCl).

Iron is also metal in the “Ni system” as carbon has a high solubility in it. Therefore, both under-coverage and over-coverage issues should be taken into consideration when adjusting the experimental parameters, especially the Fe/C ratio.

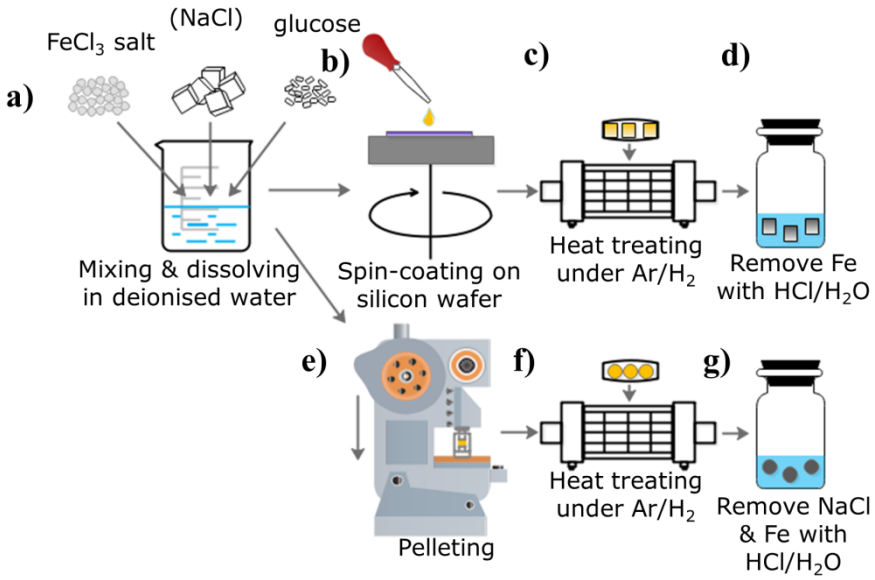

Figure 4.2. Process flow diagram of 2D and 3D graphene synthesis methods used in this chapter. For 2D graphene growth on silicon wafers, a) $FeCl_3$ and glucose were mixed in deionised water. b) Solution was then dispensed onto silicon wafer via spin-coating. c) After being heat-treated in a tube furnace with continuous Ar/H_2 flow, iron residues were removed with dilute hydrochloric acid. 3D graphene was prepared by e) pelleting dried mixture of a) $FeCl_3$, NaCl and glucose followed by a f) heat treatment. g) NaCl and iron residues were also removed with dilute hydrochloric acid.

Figure 4.2 summarised the steps to take in syntheses of 2D graphene on silicon wafers (**Figure 4.2** a)-d)) and free-standing 3D graphene foams (**Figure 4.2** a)& e)-g)). Sodium chloride (NaCl) was only added when preparing solutions for 3D foam growths as it acted as a poreforming agent and a template in a graphene 3D scaffold. Water was evaporated to achieve a homogeneous solid mixture of NaCl, $FeCl_3$ and glucose before the mixture was palletised.

4.2 2D graphene synthesis with ferric chloride ($FeCl_3$) and glucose

4.2.1 Preparation of solutions

One gram (g) of glucose powder was first weighed by an analytical balance and transferred into a beaker. 10 ml of deionised water was then measured by a graduated cylinder and poured into the same beaker. The atomic Fe/C ratio is controlled by adding different amounts of $FeCl_3$ to the glucose solution, as is listed in **Table 4.1**.

Table 4.1. Masses of the metal catalyst and carbon source for each group and the corresponding Fe/C ratios.

Sample Group No.	$FeCl_3$(g)	$C_6H_{12}O_6$(g)	Fe/C ratio
1	1.08 ± 0.01	1.00 ± 0.01	1:5
2	0.77 ± 0.01	1.00 ± 0.01	1:7
3	0.68 ± 0.01	1.00 ± 0.01	1:8
4	0.27 ± 0.01	1.00 ± 0.01	1:20

The beaker was then placed onto a heated magnetic stirrer followed by a continuous stirring with a polytetrafluoroethylene (PTFE) stir bar at 50 °C for 10 minutes. $FeCl_3$ and glucose both dissolved rapidly in water at an elevated temperature. The light brown solution was left to cool before being deposited onto silicon wafers.

4.2.2 Dropping/ spin-coating solutions onto silicon wafers

The samples were first prepared by direct deposition of droplets onto silicon wafers using pipettes.

After access was made available to a spin coater (Laurell WS-650 spin coater), another batch of samples were prepared by spin coating. The spinning accelerated at a rate of 300 revolutions per minute (rpm) from 0 to 300 rpm and was kept at 300 rpm for 5 s,

during which time solutions were deposited onto the silicon wafers with pipettes. The speed then increased to 3,000 rpm at a rate of 1,500 rpm/s and was kept for 15 s. After the samples were oven-dried for 30 min, a uniform thin film formed on the silicon wafer.

4.2.3 Heat Treatment

Silicon wafers deposited with carbon/metal solutions were placed in a ceramic boat. The boat was then pushed to the middle of a tube furnace. All the heat treatments were performed in a Vecstar 5 tube furnace supplied by Vecstar Ltd. A mixed gas flow of 95% Ar and 5% H_2 was introduced into the chamber 10 to 20 min before the heating began in order to sufficiently evacuate the air remaining in the chamber. The gas flow rate was set at 250 standard cubic centimetres per minute (sccm) when evacuating the chamber and 200 sccm throughout the heat treatments.

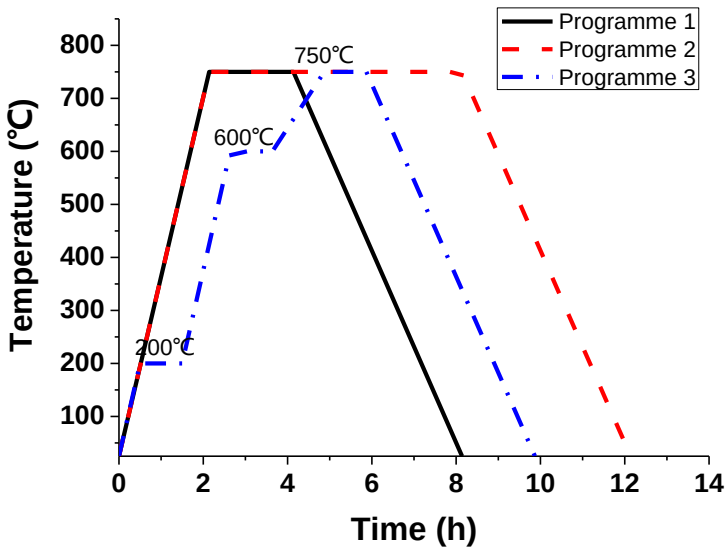

Figure 4.3. Three heating programmes were set up. The temperature was increased from room temperature to 750 °C at a rate of 5.83 °C/min and maintained for 2 h in programme 1 (black) and 6 h in programme 2 (red, dashed). Based on programme 1, in programme 3 (blue, dashed), the increase of temperature was temporarily halted at 200 °C and 600 °C, and resumed after 1 h, respectively.

Three heat-treatment programmes have been set up to investigate the effects of different metal/carbon ratios, soaking time and heating rates in this stage. A schematic diagram of the heat treatment process is provided in **Figure 4.3**.

Programme 1: The temperature first increased at the rate of 5.83 °C per minute from room temperature to 750 °C and was maintained at 750 °C for 2 h before the furnace was cooled down to room temperature.

Programme 2: It had the same heating and cooling conditions as programme one, except that the temperature was maintained at 750 °C for 6 h instead of 2 h.

Programme 3: The temperature first increased at the rate of 5.83 °C per minute from room temperature to 200 °C and was maintained at 200 °C for 1 h. Then, the temperature was further raised from 200 °C to 600 °C at the same rate and maintained at 600 °C for 1 h. The temperature was again raised at the rate of 5.83 °C per minute from 600 °C to 750 °C and was maintained for 1 h before power was removed. The furnace was then allowed to cool down to room temperature.

As no cooling system was installed with the furnace, all the samples were gradually cooled down to room temperature in a continuous gas flow atmosphere.

4.2.4 Initial material characterisation

After the furnace was cooled to room temperature, the ceramic boat was taken out by a tong. Annealed samples were then characterised without further treatment.

4.2.4.1 Uniformity of the graphene film grown

Two different methods of dispensing the solutions onto silicon wafer were explored: (1) simply releasing a single droplet onto the surface by pipette and (2) depositing a thin film of the solution onto silicon wafer via spin coating.

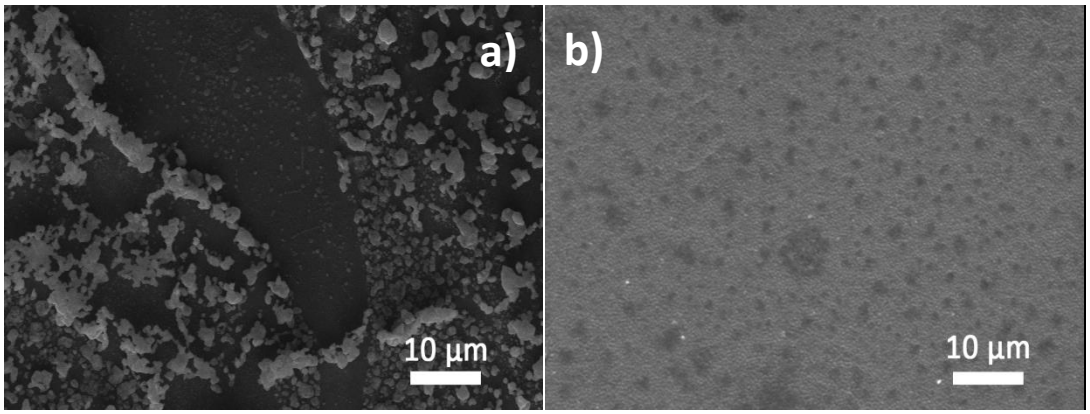

Figure 4.4. Medium magnification (5,000x) SEM images showing the surfaces of 2D graphene grown on Si substrates with ferric chloride and glucose (Fe/C atomic ratio = 1: 7). The Fe/C solution was deposited a) directly with a pipette or b) using a spin-coater.

Synthesised with the same solution (Fe/C atomic ratio = 1: 7) and heat treatment programme (programme 1), the surface of the sample prepared from the droplet (**Figure 4.4** a)) appears to be less uniform than that prepared by spin-coating (**Figure 4.4** b)) in the images captured by SEM. The former surface shows a typical pattern of "coffee ring", which usually appears during the liquid evaporation process. This is because the edge of a droplet on a surface evaporates faster than its centre. As a result, a flow is induced from centre to edge, constantly bringing the solutes to the edge, resulting in a thicker edge and a thinner centre [1]. That can explain the appearance of particles of different sizes and shapes in **Figure 4.4** a). On the other hand, the sample surface prepared by spin-coating is relatively smooth. Only small particles of comparable sizes are observed under the same magnification.

To conclude, spin-coating can effectively reduce particle agglomeration and avoid the "coffee ring effect" that occurs as the liquid drops evaporate. Surfaces of spin-coated samples are more uniform and more controllable. When agglomeration is present, it will raise the bar for sample characterisation as the sample's properties or characteristics may vary by location. Therefore, all the sample preparations that involve solution deposition onto a flat surface will be carried out on spin coaters.

4.2.4.2 Effects of different heat treatment programmes

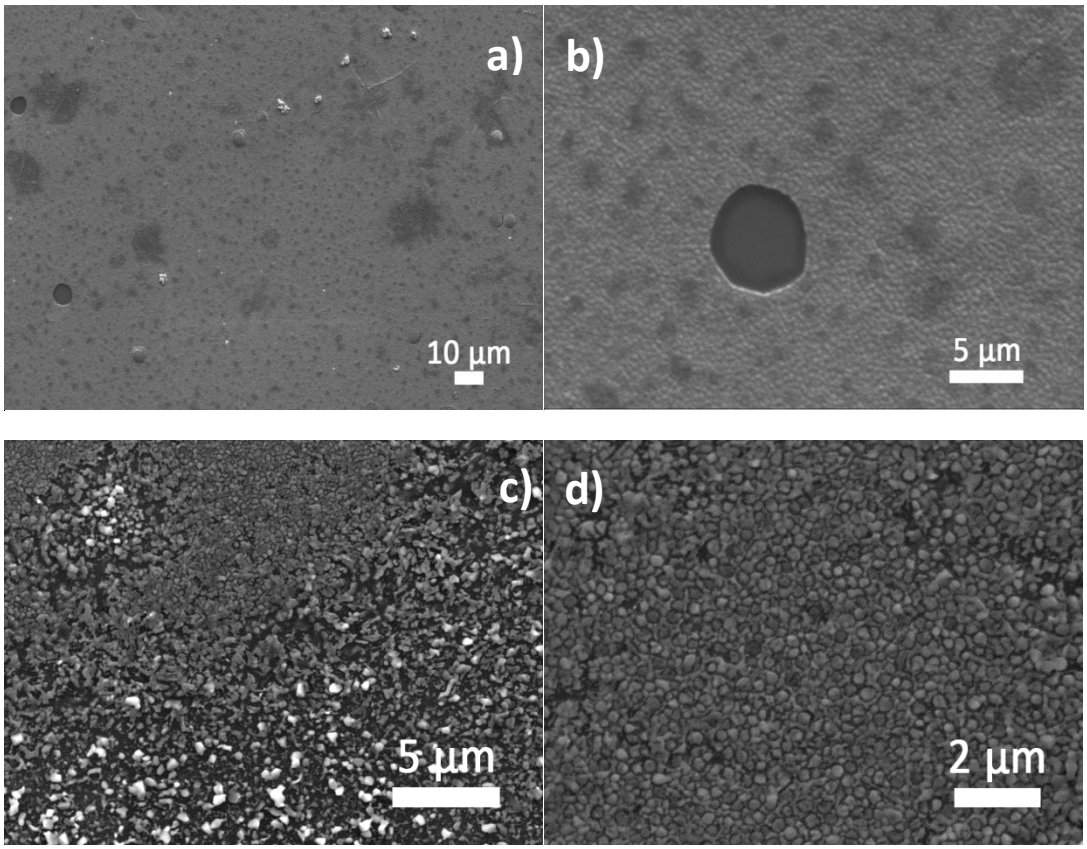

Figure 4.5. SEM images showing the surfaces of 2D graphene grown with spin-coated ferric chloride and glucose (Fe/C atomic ratio = 1: 5) on silicon wafers. The samples were treated with a a) & b) single-step heating programme1 and a c) & d) multi-step heating programme 3, respectively.

The samples in **Figure 4.5** a) & b) and **Figure 4.5** c) & d) were prepared by spin-coating from the same solution with a Fe/C ratio of 1:5. The only difference is that the sample

in **Figure 4.5** a) & b) went through heat treatment programme 1, which involves a single-step heating cycle and the second group of samples went through heating programme 3, which involves multiple steps.

The single-step heat treatment resulted in a smoother surface but with random holes which are assumed to be formed when the gas bubbles burst. In the meanwhile, multi-step heat treatment resulted in a less uniform surface with the appearance of particles of different sizes. However, the surface was fully covered, and no visible hole was observed.

4.2.4.3 Burst blister marks observed on samples surfaces

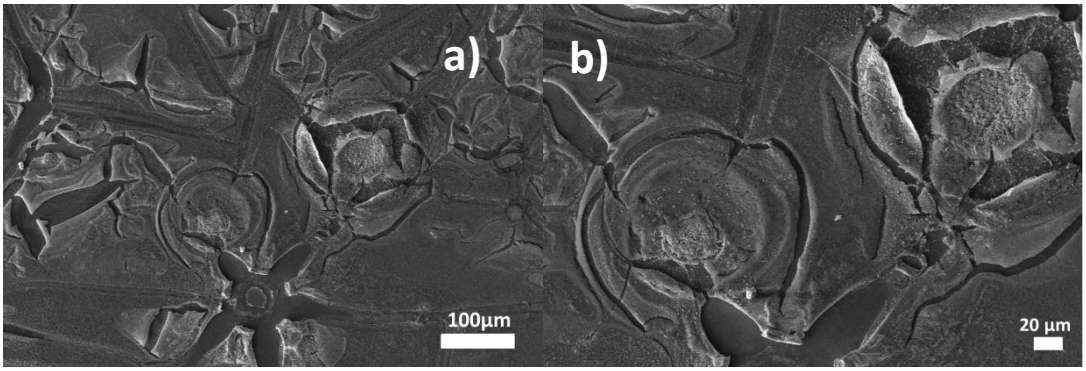

Figure 4.6. Low magnification a) 500x, b) 1000x SEM images showing the surfaces of 2D graphene grown with spin-coated ferric chloride and glucose (Fe/C atomic ratio = 1: 20) on silicon wafers. The samples were heat-treated with a single-step heating programme 1.

Marks that appeared to be left by burst blisters were observed on the surface of samples prepared with a low Fe/C ratio (1: 20) in **Figure 4.6**. Chemical equations that describe the reactions taking place during the heat treatment are listed below:

$$6FeCl_3(s) + C_6H_{12}O_6(s) \rightarrow 6FeCl_2(s) + C_6H_6O_6(s) + 6HCl(g)$$

(reduction of glucose by $FeCl_3$);

$$2\,FeCl_3(s) + H_2(g) \rightarrow 2\,HCl(g) + 2\,FeCl_2(s)$$

(reduction of $FeCl_3$ by hydrogen).

Gaseous HCl was produced in both reductions of $FeCl_3$ and glucose. The gas is highly caustic, so it seems possible that when the HCl gas molecules trapped underneath the graphene film try to escape, they will crack the film and leave a mark of burst blister behind.

Another assumption is made that when the Fe/C ratio is high, glucose will tend to react with the Fe in its vicinity. In contrast, when the Fe/C ratio is low, one Fe atom will interact with several glucose molecules. Excessive glucose molecules will turn to hydrogen molecules in the gas flow instead and directly release gas molecules such as H_2O. In this case, the number of blisters can be decreased by increasing the Fe/C ratio or slowing down the reactions by reducing the heating rate or adopting multi-step heat treatment.

4.2.4.4 Chemical composition of bright particles on sample surfaces

The bright particles observed in SEM results were further analysed by EDS and Raman. Contrary to expectation, the surface topography of samples prepared with different Fe/C ratios (1:7 in **Figure 4.4**, 1:5 in **Figure 4.5** and 1:8 in **Figure 4.7**) did not significantly differ in SEM images.

In **Figure 4.7** a), a typical SEM image of an unwashed sample is displayed. And **Figure 4.7** b) is the EDS spectrum obtained after two scans over the selected area were averaged.

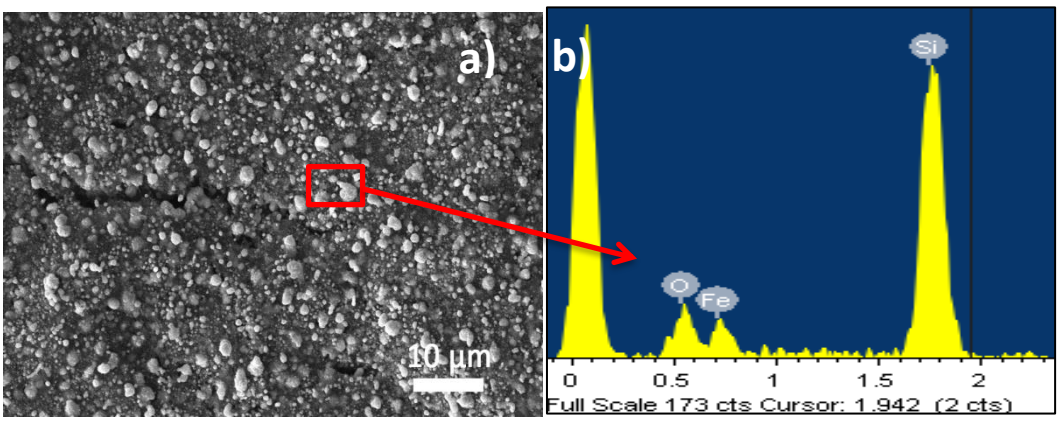

Figure 4.7. a) SEM image of the unwashed sample (Fe/C atomic ratio = 1:8) on the silicon substrate and b) EDS spectrum of the highlighted area.

The Si peak is the most prominent in the spectrum, with relatively weak Fe and O peaks. There was no carbon peak identified. This might be associated with the large reaction volume involved in EDS analysis. The incident X-ray used in this technique has a high accelerating voltage, so it can reach deeper regions below the surface and interact with all the atoms along its way. It is likely that EDS X-ray has penetrated through the carbon layer easily because 1) carbon layer is thin, 2) carbon atoms are light and not sufficient to 'stop' the X-ray by absorbing all its energy. A large proportion of the X-ray energy was absorbed by the heavier silicon atoms below the surface, causing a significant amount of silicon-related signals to be released and detected. From this point of view, EDS integrated into Ultra 55 SEM is not an ideal tool to identify or quantitatively analyse the chemical composition of graphene grown on silicon wafers.

Table 4.2. Chemical composition of the bright particles highlighted in **Figure 4.7** a) by energy-dispersive X-ray spectroscopy (EDS) analysis

Element	Weight %	Atomic %
O	14.60	26.10
Si	59.56	60.66
Fe	25.84	13.24
Totals	100.00	

However, EDS still provided us with some helpful information on iron particles. According to the spectrum in **Figure 4.7** b) and the chemical composition of the scanned area listed in **Table 4.2**, the atomic percentages for Fe and O are 13.24% and 26.10%, respectively. The atomic ratio of Fe/O is 1:2. Thus an empirical formula of FeO_2 (iron dioxide) can be deduced. Nevertheless, this oxide form of iron can only be stabilised under ultra-high pressure and temperature and does not exist under normal conditions [2]. A plausible interpretation of the results is that the oxygen atoms detected did not entirely originate from oxides of iron. Native silicon dioxide (SiO_2) will naturally form at the silicon wafer surface when the wafer is exposed to oxygen in the air. However, it is unfeasible to estimate the exact amount of oxygen contained in the protective SiO_2 layer as the thickness of that layer is unknown. Other than the silicon dioxide, the oxygen may also belong to the functional groups attached to the graphene surface during growth, indicating the formation of defective graphene instead of pristine graphene.

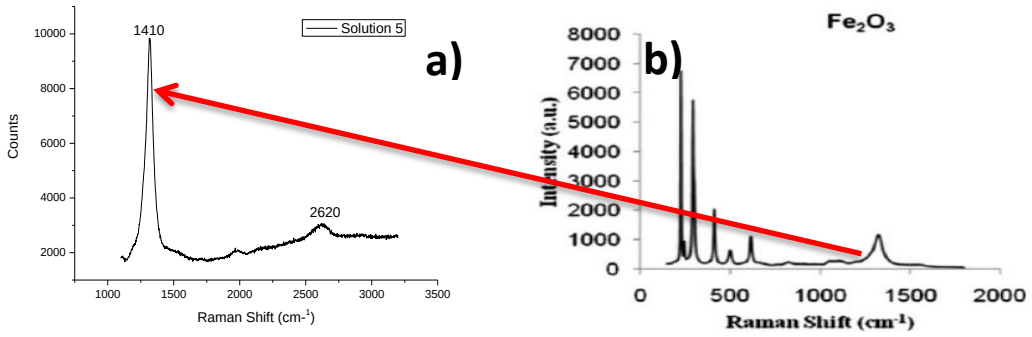

Figure 4.8. Raman Spectra of a) unwashed sample (Fe/C atomic ratio = 1:8) prepared with heat treatment programme 1 on the silicon substrate and (b) Fe_2O_3 in reference [3].

The same sample was further characterised by Raman spectroscopy after being analysed by EDS. Its spectrum in **Figure 4.8** a) shows a sharp peak around 1410 cm^{-1}. A comparison was made with the Raman spectrum of iron oxide (III) (Fe_2O_3) presented in Glasscock's work (**Figure 4.8** b)) [3]. The position overlap of the characteristic peak

indicates that the big, bright particles observed on the sample surface might be Fe_2O_3 instead of FeO_2.

The peak at 1410 cm^{-1} in **Figure 4.8** a) is so intense that other peaks are dwarfed. As a result, only a weak peak at 2620 cm^{-1} can be observed, corresponding with the 2D peak resulting from structural stacking in graphene-related materials.

Overall, both EDS analysis and Raman spectroscopy confirmed that the large particles on the surface are iron oxide instead of $FeCl_3$, which implied a successful reduction of $FeCl_3$ during the annealing at high temperature with the presence of reducing gas H_2. The reduced particles of iron could then act as irregular-shape substrates for graphene growth.

4.2.5 Sample cleaning

Since it was verified by the results of SEM and Raman analyses that iron oxides were produced after the annealing. Compared with carbon atoms, Fe atoms are considerably heavier and intend to interact with other chemicals as well as the incident beams used in several characterisation techniques more strongly [4]. That usually leads to high background in the data achieved in such techniques though the graphene covered under these particles is the actual material of interest. Hence, it is crucial to remove these iron oxide particles to get a clean carbon surface. As was discussed in Chapter 4.1, iron and its oxides can all react with dilute hydrochloric acid, forming gases, water and aqueous iron salts. A rinse with water can further remove the salts.

Samples, together with their silicon substrates, were soaked in 20ml of 20% hydrochloric acid. The 20% acid was prepared by slowly and carefully adding 540 ml of 37% HCl to 460 ml of distilled water with constant swirling to ensure the acid was evenly mixed.

The acidic solution was refilled and changed every day to provide the sample with sufficient HCl to react with until no evident impurity particles could be seen at the graphene surface in the SEM images. This acid washing process mostly lasted one to two weeks.

No external stimulus or force was applied at first. However, it was noticed that some graphene flakes would naturally fall off the silicon wafers after some time of acid washing. It can be a consequence of the iron depletion between the graphene layer and the silicon surface. A detailed mechanism is illustrated in **Figure 4.9**. With an increased amount of iron residues dissolved in dilute hydrochloric acid, gaps and holes were left in between graphene/graphene and graphene/silicon surfaces, which may result in a separation of graphene layers as well as the graphene falling off the silicon substrate.

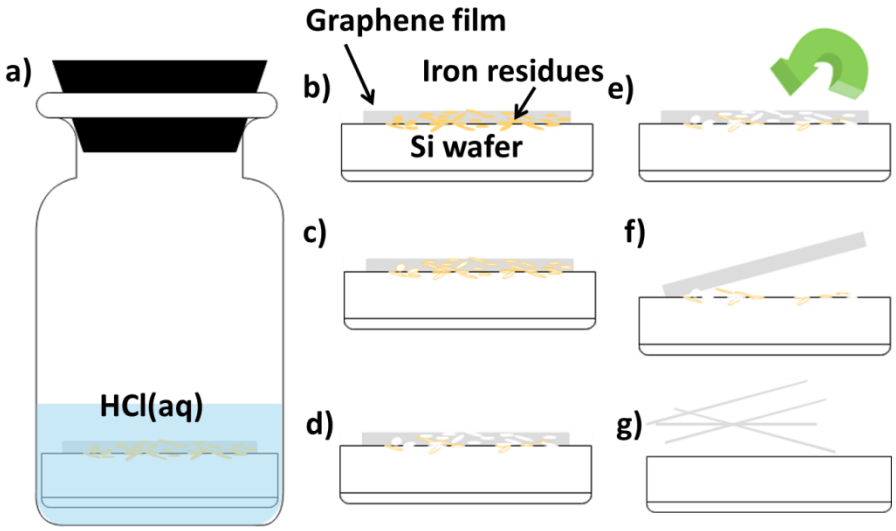

Figure 4.9. Schematic diagram of the iron residues dissolution and graphene film falling off processes. a) Sample was placed in a hydrochloric acid solution for iron oxide particles removal. b) A close-up image of the graphene film grown on top of the silicon wafer with residues distributed in between graphene layers and the surface between Si and graphene. c) & d) Residues gradually dissolved in HCl solution. e) & f) Holes were left in between graphene/graphene and graphene/Si surfaces, causing the thin graphene layer to detach from the Si substrate. g) Graphene film fully detached from the substrate and separated into thinner layers.

Since graphene flakes were now dispersed in the acidic solution after falling off the substrate, ultrasonication was applied to accelerate the removal of residues and further open the gaps between graphene layers to obtain graphene with improved purity and decreased thickness.

Dilute hydrochloric acid was changed and refilled through pump filtration followed by a rinse with deionised water. This process was repeated several times before the washed graphene was finally dispersed in deionised water and deposited onto silicon wafers for further characterisation.

4.2.6 Characterisation of further cleaned samples

4.2.6.1 Effects of sample cleaning with hydrochloric acid

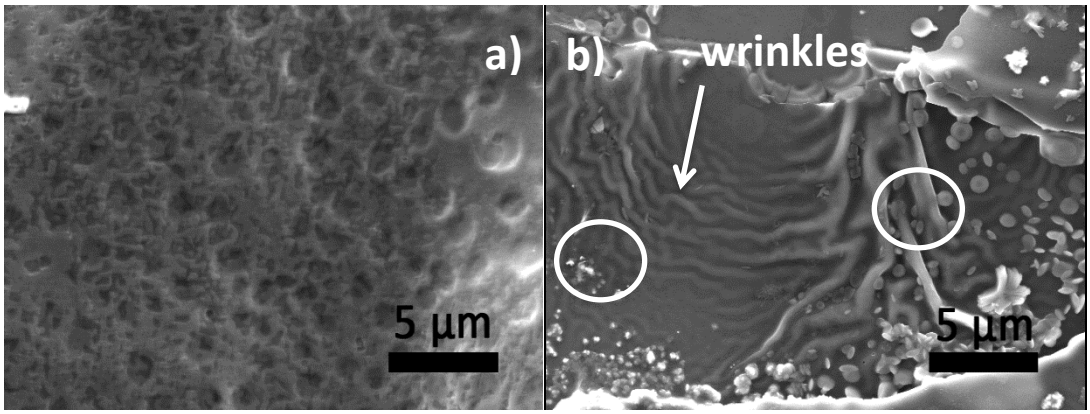

Figure 4.10. a) & b)SEM images of samples (Fe/C atomic ratio = 1:8) prepared with heat treatment programme 1 after being washed in dilute hydrochloric acid with ultrasonication.

After ultrasonication facilitated washing in hydrochloric acid, a substantial amount of the iron oxides have been dissolved and removed, leaving some pits on the surface, as shown in **Figure 4.10** a). It seems unfeasible to remove all the iron oxide particles remaining in the film for the following reasons:

i) Some of the particles may be stuck in between the wrinkles observed in **Figure 4.10** b). Graphene is impermeable and has made it difficult for the residue particles and the aqueous HCl to reach each other.

ii) Graphene might have been functionalised by Fe [5, 6], which implies that graphene and Fe can be conjugated rather than just physically attached.

iii) In common with the first reason, due to the complex morphology of the graphene surface, even if the iron oxides were fully dissolved, the derived $FeCl_2$/$FeCl_3$ salts could still be trapped in the structure and transformed into white solids after water solvent evaporated

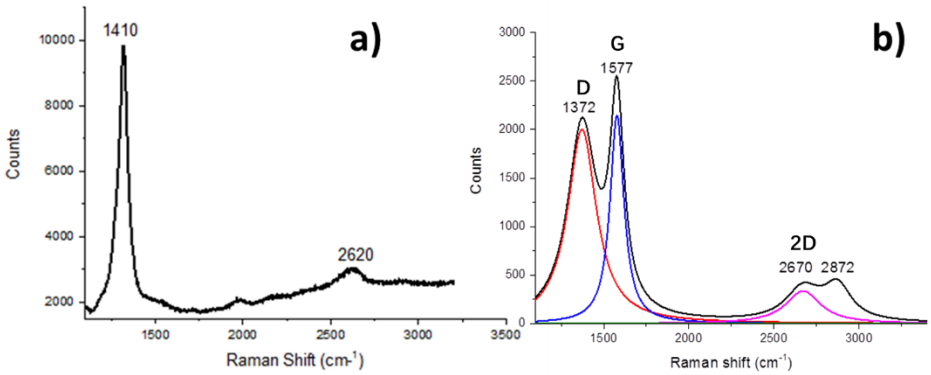

Figure 4.11. Raman spectra of samples (Fe/C atomic ratio = 1:8) prepared with heat treatment programme 1 a) before and b) after being washed in dilute hydrochloric acid with ultrasonication. The D peak (red), G peak (blue) and 2D peak (pink) in the second spectrum were fitted with Lorentzian function.

Raman spectra of the same sample showed a significant difference before (**Figure 4.11** a)) and after (**Figure 4.11** b)) the sample was washed in dilute hydrochloric acid.

The spectrum of the unwashed sample was dominated by a sharp peak around 1410 cm^{-1}, which is associated with the presence of Fe_2O_3.

The characteristic graphene-related peaks were observed after the sample was

washed. The first peak at around 1370 cm^{-1} is a D band that reflects the density of defects (can be vacancy type defects, impurity atoms, grain boundaries, flake edges, or functional groups). The high intensity of the D band indicates the presence of a large number of defects in the plane.

The second peak at 1577 cm^{-1} is the G band which indicates the presence of sp^2 bonds and is related to in-plane vibrations of sp^2 carbons.

The 2D peak at 2670 cm^{-1} is a D peak overtone and indicates the stacking order in graphitic materials, while the peak at 2870 is another defect-related D+D' peak.

Table 4.3. Key parameters of D, G, 2D and D+D' peaks in the fitted Raman spectrum curve (**Figure 4.10** b)) obtained from the sample (Fe/C atomic ratio = 1:8) prepared with heat treatment programme 1 after being washed by dilute hydrochloric acid with ultrasonication.

Curve name	Centre	Width	Height	% Gaussian	Type	Area	ChiSq
Curve 1	1372.12	205.036	2000.09	0	Lorentzian	644170	1.01E-08
Curve 2	1577.61	99.1496	2147.43	0	Lorentzian	334449	
Curve 3	2670.8	249.875	336.45	0	Lorentzian	132058	
Curve 4	2872.54	198.816	350.491	0	Lorentzian	109458	

The intensity ratios I_D/I_G and I_G/I_{2D} of the washed sample can be calculated with the parameters regarding D, G and 2D peaks provided in **Table 4.3**:

$$I_D/I_G = 2000.09/2147.43 \approx 0.93;$$

$$I_G/I_{2D} = 2147.43/336.45 \approx 6.38$$

The ratio I_D/I_G reflects the quality of graphene, and it increases as defect density in graphene increases. A ratio of 0.93 is not comparable to that in pristine graphene obtained via mechanical exfoliation [7, 8] or liquid phase exfoliation [9]. But it is still superior to that obtained via GO reductions [10, 11], which is generally greater than 1.

The high I_G/I_{2D} ratio suggests that the number of layers in synthesised graphene is

relatively large, which is in accordance with the observations in SEM images.

4.3 3D graphene synthesis with ferric chloride ($FeCl_3$) and glucose

4.3.1 Pellets preparation

The 3D structure in graphene foams was fabricated by using pellets of carbon/metal mixture instead of films on silicon in the case of 2D graphene growth. In most literature reviewed in Chapter 2, metal or metal salt particles were directly made the body of 3D foams. Namely, in order to make a ten cubic decimetre (dm^3) graphene foam, approximately ten dm^3 of metal catalyst will be used in the fabrication. However, that does not seem to be adaptable when shapes of large dimensions are desired.

In our work, sodium chloride (NaCl) was added to the carbon/metal mixture and acted as a template as well as a pore former in the process of 3D foam fabrication. Just as glucose and $FeCl_3$, NaCl is inexpensive, non-hazardous and accessible to almost every lab. It is also easy to remove with water after the foam synthesis is completed.

Table 4.4. Masses of NaCl, metal catalyst and carbon source for each group and the corresponding Fe/C ratios.

Sample Group No.	NaCl(g)	$FeCl_3$(g)	$C_6H_{12}O_6$(g)	Fe/C ratio
1	1.00 ± 0.01	5.42 ± 0.01	1.00 ± 0.01	1:1
2	1.00 ± 0.01	1.08 ± 0.01	1.00 ± 0.01	1:5
3	1.00 ± 0.01	0.54 ± 0.01	1.00 ± 0.01	1:10
4	1.00 ± 0.01	0.27 ± 0.01	1.00 ± 0.01	1:20
5	1.00 ± 0.01	0.11 ± 0.01	1.00 ± 0.01	1:50

1 g of NaCl powder and 1g of glucose were weighed and dissolved in 10 ml of deionised water. The atomic Fe: C ratio (ranging from 1:1 to 1: 50) was still controlled by adding various amounts of $FeCl_3$ to the solution, as listed in **Table 4.4**. The solvent was evaporated before the mixture was cold-pressed into a spherical pellet of 1cm in

diameter, around 0.7 to 1 cm in height, for samples in groups 2 to 4 and around 3cm for samples in group 1.

4.3.2 Heat Treatment

The annealing of 3D samples was carried out at the same heating conditions as for 2D samples. In addition, programmes were set up for single- and multi-step annealing.

4.3.2.1 Effect of single-step and multi-step heat treatment

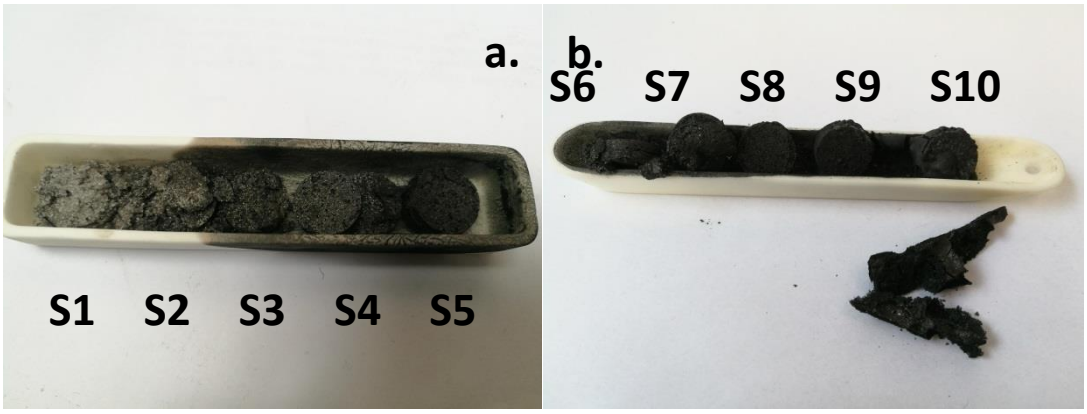

Figure 4.12. Photo images of pellets prepared with different Fe/C atomic ratios (from left to right in each boat: 1:1; 1:5; 1:10; 1:20; 1:50) after heat-treated under programme 1 (S1-S5) and programme 3 (S6-S10).

Pellets that annealed under programme 1 (**Figure 4.12** a)) turned into powders during this process. Sample 5 was the only one that still maintained its pellet shape, but it also turned into powder when a lab spoon was used to pick it up. The powder scraps of different samples were mixed at surfaces of contact and could not be separated.

The powderisation has resulted from the single-step, rapid heating in programme 1. As discussed in Chapter 4.2.4.3, during the heating, samples will release gases including H_2O from pyrolysis of glucose and dehydration of $FeCl_3 \cdot 6H_2O$, and HCl from the reduction of $FeCl_3$.

When the temperature was raised up to 750 °C directly, all the reactions took place within a short time with a vast amount of gases escaping from the pellets all at once. Thus, the template was broken even before graphene was formed.

On the contrary, programme 3 has given each reaction at different temperatures sufficient time, so the gases were released gradually. In **Figure 4.12** b), the edges of some samples were still powdered, but the samples all maintained the pellet shape, and they can easily be picked up by hand without being crushed.

Samples obtained through heat treatment programme 3 were further processed and characterised.

4.3.2 Initial material characterisation

4.3.2.1 Chemical compositions of powders obtained straight after heat treatment

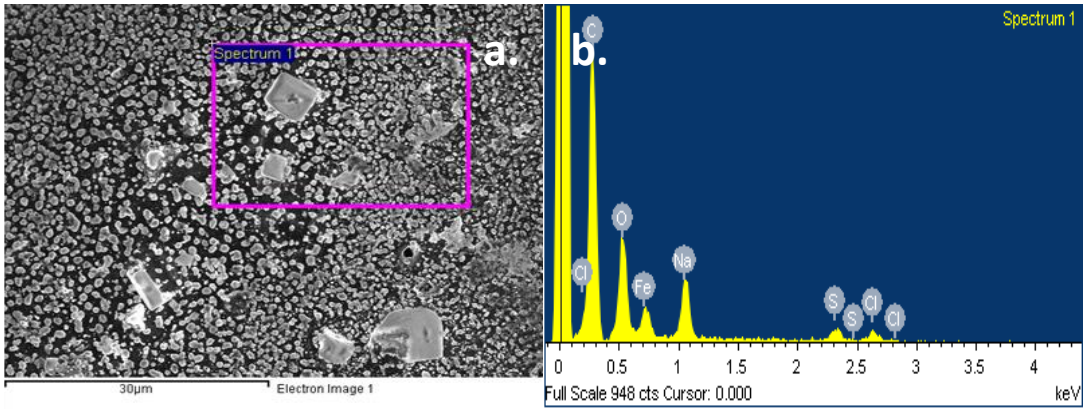

Figure 4.13. a) SEM image of Fe/C atomic ratio = 1: 10 sample surface after multi-step heat treatment. b) EDS spectrum of the selected area marked in a).

In **Figure 4.13** a), a few large cubic crystals surrounded by smaller particles can be observed. Judging from the shapes of the crystals, the cubic particles are believed to be NaCl crystals while, in accordance with previous findings, the smaller bright

particles surrounding NaCl should be oxides of iron. The EDS spectrum further confirmed this in **Figure 4.13**. Without the strong background peaks originated from Si/SiO_2 wafers, a clear, prominent peak from carbon could be detected.

Detailed element composition information is provided in **Table 4.5**. It should be noticed that, since the sample was mounted to the SEM test stub by an adhesive carbon tape, the content of the carbon detected was not solely resulted from the graphene synthesised.

Table 4.5. Chemical composition of the area highlighted in **Figure 4.13** a) by energy-dispersive X-ray spectroscopy (EDS) analysis

Element	Weight (%)	Atomic (%)
C	60.37	74.95
O	12.44	11.59
Na	10.79	7.00
Cl	13.54	5.69
Fe	2.87	0.77
Totals	100.00	

The ratio of atomic percentages of Na to Cl was approximately 5:4, indicating the composition of NaCl. Furthermore, the high concentration of O (atomic % = 11.59), compared with that of Fe (0.77%), indicated that except for iron oxides formed as particles in the body of graphene foam, the graphene might also have been doped with oxygen.

4.3.3 Pellets washed with hydrochloric acid

The pellets were directly put into 100 ml of 20% hydrochloric acid to remove sodium chloride, iron and iron oxides. The pellets soon collapsed into tiny pieces in the acid.

The samples were then left dispersed in acid and stirred in a magnetic stirrer for 24 h to facilitate the dissolution of iron products and NaCl. After 24 h, the solutions were pump filtered, followed by a deposition of solution onto silicon wafers as well as TEM copper grids in preparation of samples for various characterisations. The rest of the samples were oven-dried at 60 °C.

4.3.3.1 Morphology and chemical composition analyses of samples washed in hydrochloric acid.

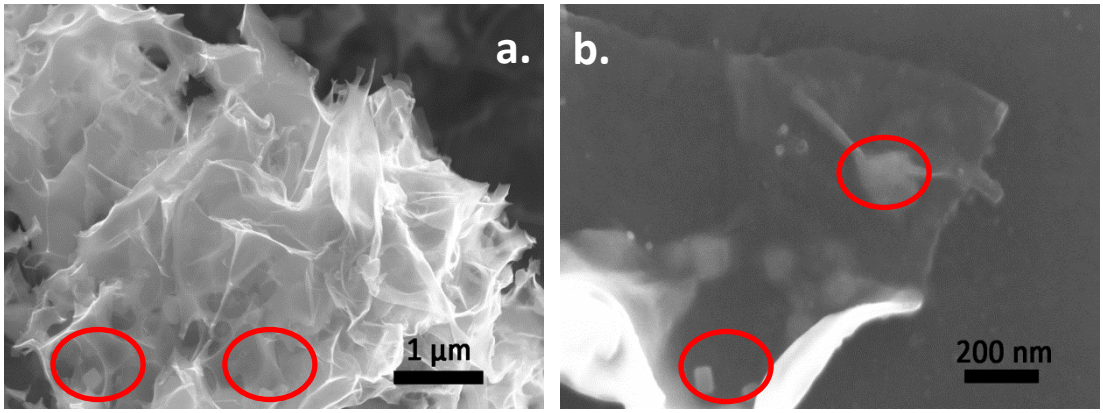

Figure 4.14. SEM images of the collapsed pellet (Fe/C atomic ratio = 1:20, multi-step heat-treated) washed in hydrochloric acid. a) showed a foam structure of the 3D graphene and b) highlighted residues covered under or inside a thin graphene membrane.

Although the pellets (Fe/C atomic ratio = 1:20, multi-step heat-treated) soon collapsed into tiny pieces during the acid washing process, the pieces still maintained a porous 3D structure as demonstrated in **Figure 4.14** a). The thin membrane is highly transparent to the electron beam, and through the thin membrane, some cubic particles can be spotted wrapped inside.

Figure 4.14 b) showed an ultra-thin edge of a flake under SEM. Again, bright particles were observed lying beneath the thin membrane.

The composition of the bright particles trapped in synthesised 3D graphene foam was confirmed to be NaCl by EDS spectra in **Figure 4.15**. However, there was no evidence which indicated the presence of iron oxides. Therefore, hydrochloric acid is highly effective for removing iron by-products.

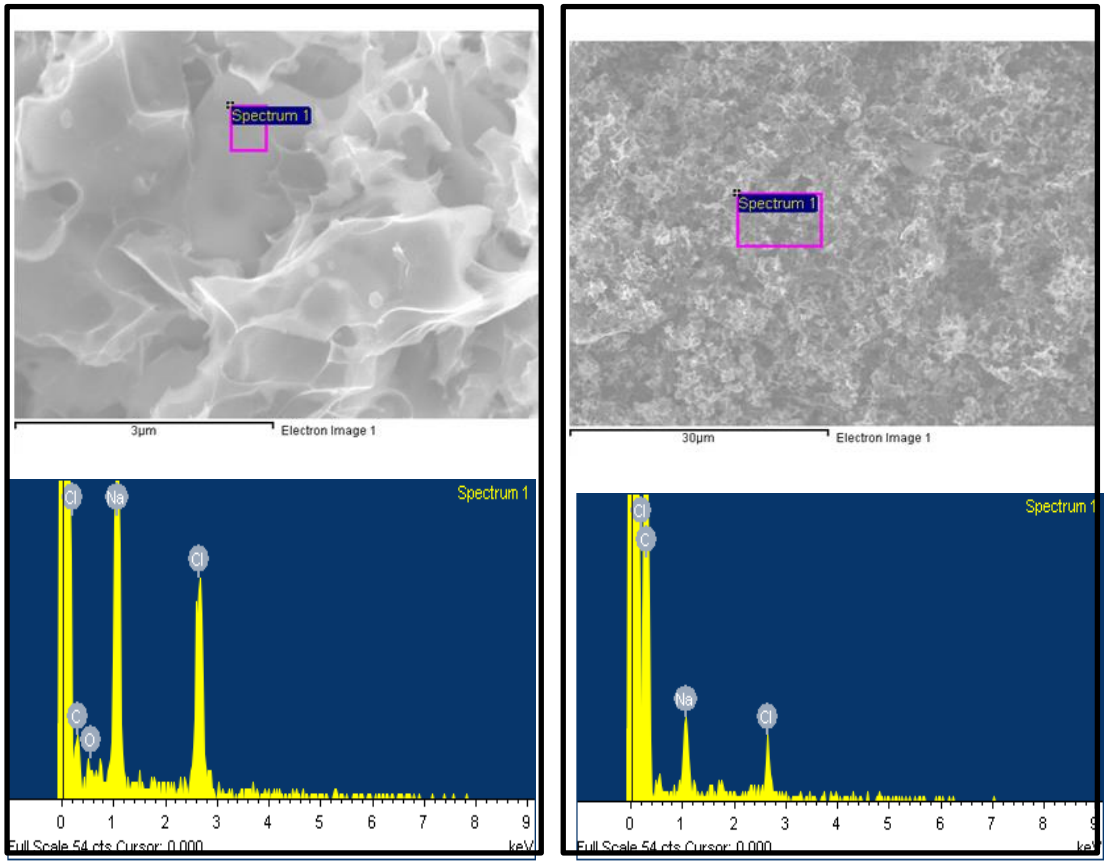

a. b.

Figure 4.15. SEM images and corresponding selected area EDS spectra of the pellets (Fe/C atomic ratio = 1:20, multi-step heat-treated) washed in acid.

4.3.5 Further sample cleaning with deionised water followed by sample characterisation

Since a traceable amount of NaCl was still observed and detected after the cleaning with hydrochloric acid, samples were given a further cleaning in 100 ml of deionised water repeatedly. Same stirring, pump filtering and refilling procedures were adopted. EDS, combined with SEM analysis, was employed to monitor the progress of sample

cleaning. These procedures were repeated until most NaCl and iron residues were removed.

4.3.5.1 Morphology and chemical composition analyses of samples washed with hydrochloric acid and deionised water

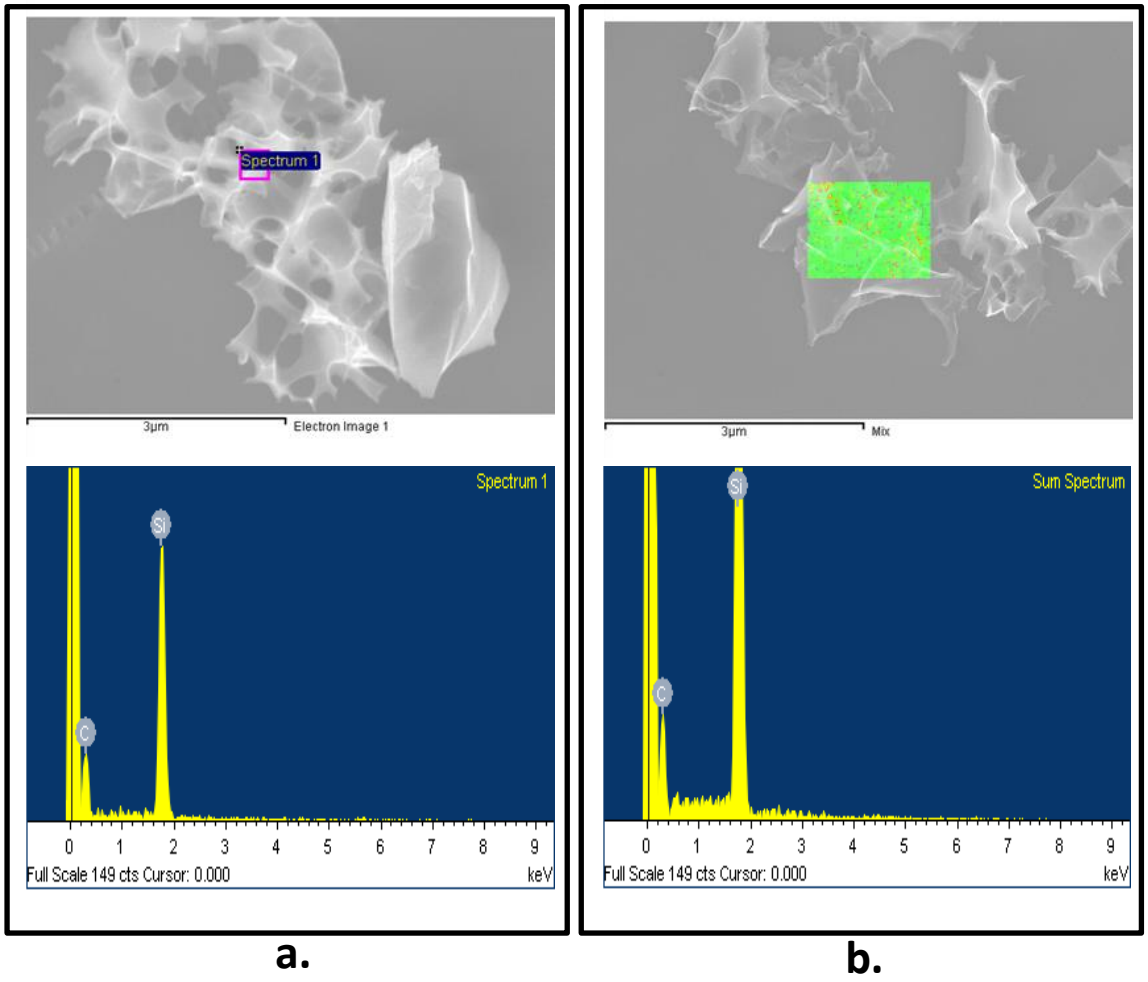

Figure 4.16. SEM images with the corresponding a) selected area EDS spectrum and b) EDS map of the 3D foam (Fe/C atomic ratio = 1:20, multi-step heat-treated) washed in hydrochloric acid and deionised water.

According to the data presented via the selected area EDS spectrum and EDS map in

Figure 4.16, after repeated washing in deionised water, only carbon could be detected on the silicon wafer, which indicated that a substantial amount of sodium chloride

residue had been removed.

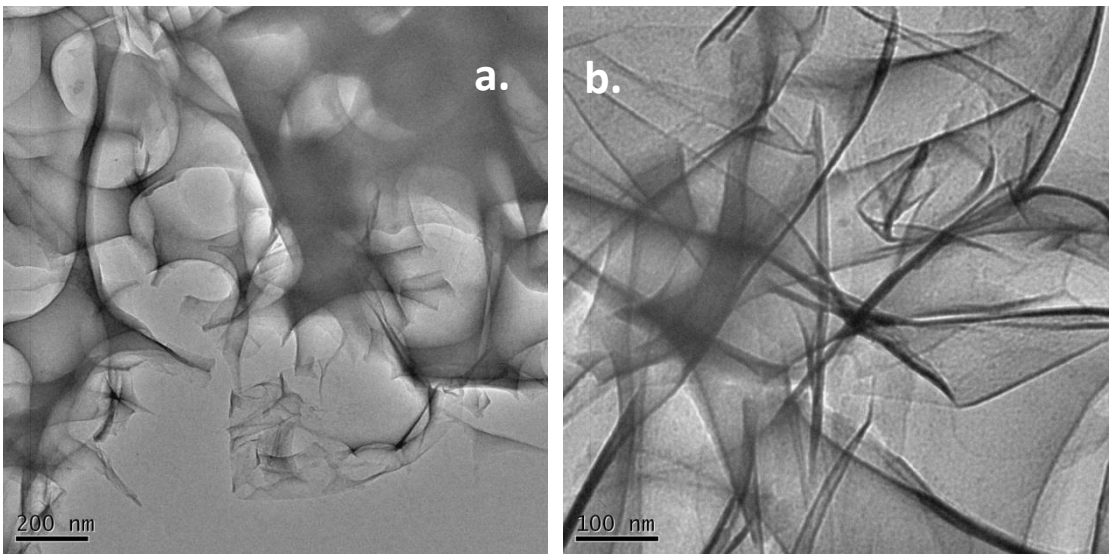

Figure 4.17. High-resolution TEM images of the 3D foam (Fe/C atomic ratio = 1:50, multi-step heat-treated) washed in hydrochloric acid and deionised water.

The TEM images in **Figure 4.17** a) confirmed the interconnected porous structure of 3D graphene foam obtained after the annealing and washing. In addition, the membrane was thin and highly transparent, indicating a low number of layers in the fabricated graphene. Besides, no evident residue of NaCl or iron oxides was spotted.

4.3.5.2 Crystal structure determination of samples washed with hydrochloric acid and deionised water

The crystal structure of the powdered 3D foam was analysed by XRD. **Figure 4.18** b) depicts different shapes of the XRD patterns recorded for graphite (black), GO (red) and graphene (blue) materials [12].

The sharp, intense peak at $2\theta = 26.4°$ in graphite has resulted from the diffraction of its (002) planes. The corresponding lattice spacing is calculated to be 0.34 nm according to Bragg's Law. XRD pattern for GO usually shows a lower intensity characteristic peak around $2\theta = 11°$ from diffractions in (001) planes with an expanded

lattice spacing of 0.8 nm. The 2θ = 26.4° peak is related to the diffraction of X-ray by lattice perpendicular to the carbon basal plane. Therefore, single-layer graphene gives little to no signal in its XRD pattern.

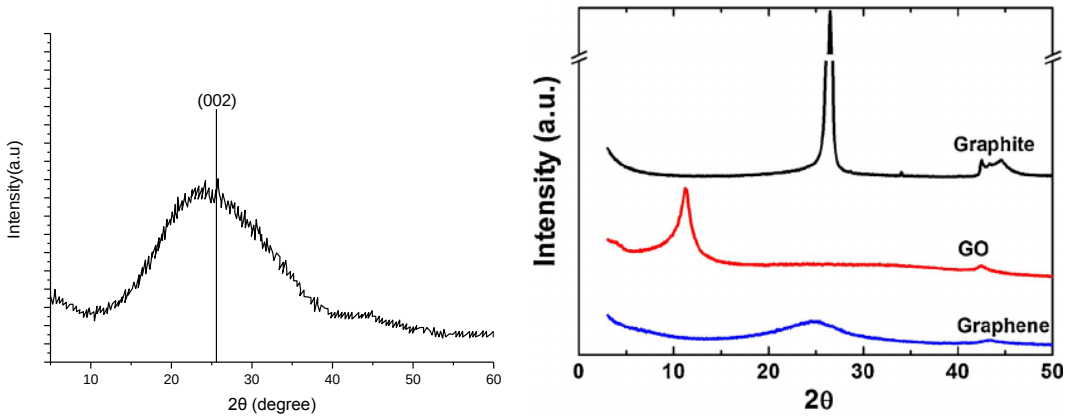

Figure 4.18. a) XRD pattern obtained from powdered 3D foam (Fe/C atomic ratio = 1:10, multi-step heat-treated) washed in hydrochloric acid and deionised water. b) XRD patterns of graphite (black), GO (red), and graphene (blue) compared in Johra's paper [12].

The 2θ peak recorded for the washed powdered 3D foam was around 24.5° (**Figure 4.18** a)), indicating an average interlayer spacing of 0.36 nm, which is slightly larger than the lattice spacing in graphite. The increased spacing may result from the out-of-plane defects on graphene sheets due to doping with oxygen, which agrees with the findings in EDS analysis (see Chapter 4.3.2.1). In addition, the evident shape and intensity of the peak revealed a stacking structure in the synthesised 3D graphene, which is consistent with the result of Raman analysis (see Chapter 4.2.6.1).

Samples prepared with different Fe/C ratios were all analysed by XRD. The average 2θ positions and corresponding lattice spacing were calculated and summarised in **Table 4.6**. Plots of the crystal information against the Fe/C ratios were made (**Figure 4.19**).

Table 4.6. Table of average lattice spacing for samples prepared with various Fe/C atomic ratios calculated from the average 2θ positions recorded in XRD patterns.

Fe/C atomic ratio	average 2θ (degree)	average lattice spacing(nm)
1:1	25.7	0.355
1:5	24.8	0.367
1:10	24.5	0.371
1:20	22.6	0.401
1:50	21.5	0.420

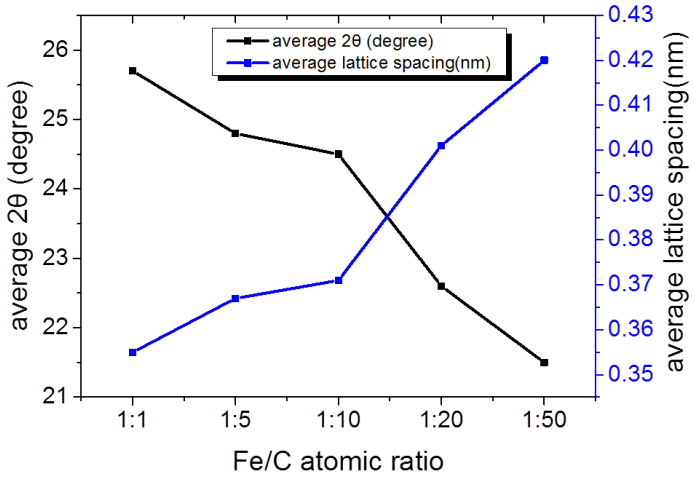

Figure 4.19. Plots of average lattice spacing and average 2θ positions against Fe/C atomic ratios derived from **Table 4.6**.

As the concentration of carbon increased, the 2θ position was shifted to a lower angle, leading to an increase in graphene's lattice spacing. Namely, as more carbon was added to the starting material, the interlayer distance was enlarged, the more expanded the graphene became.

4.3.5.3 Structural information about samples washed with hydrochloric acid and deionised water

Raman spectra were acquired for the samples treated under a multi-step heating

programme. After baseline subtraction and curve fitting with the Lorentzian function (as illustrated in **Figure 4.11** b)) were done, information of the characteristic D, G, 2D peaks was recorded for each spectrum. Multiple spectra were acquired for each sample at 30 randomly chosen locations at least. After taking averages of the data, the curves were normalised and stack-plotted in **Figure 4.20**.

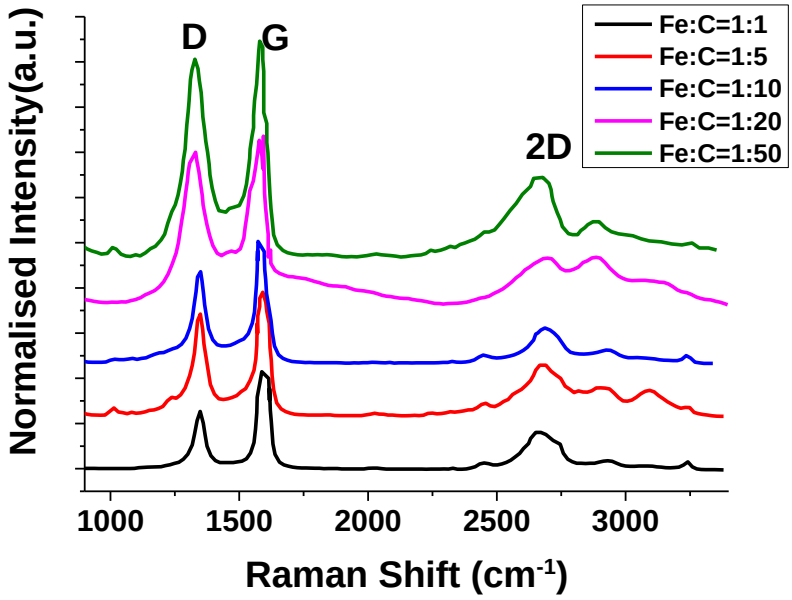

Figure 4.20. Average normalised Raman spectra of samples prepared with various Fe/C atomic ratios.

The intensity ratios for samples prepared with different Fe/C contents were summarised in **Table 4.7** and plotted against the Fe/C ratio in **Figure 4.21**.

The I_D/I_G ratios obtained in 3D graphene samples are slightly lower than the ratio previously obtained in 2D graphene, indicating a lowered defect density achieved in 3D graphene. In addition, the I_G/I_{2D} ratio is also decreased from ~6 (for 2D graphene) to ~3 (for 3D graphene), indicating a decreased number of graphene layers.

Table 4.7. Table of average I_D/I_G and I_G/I_{2D} ratios for samples prepared with various Fe/C atomic ratios.

Fe/C atomic ratio	average I_D/I_G	average I_G/I_{2D}
1:1	0.869	2.431
1:5	0.895	3.201
1:10	0.913	3.162
1:20	0.949	3.019
1:50	0.936	2.583

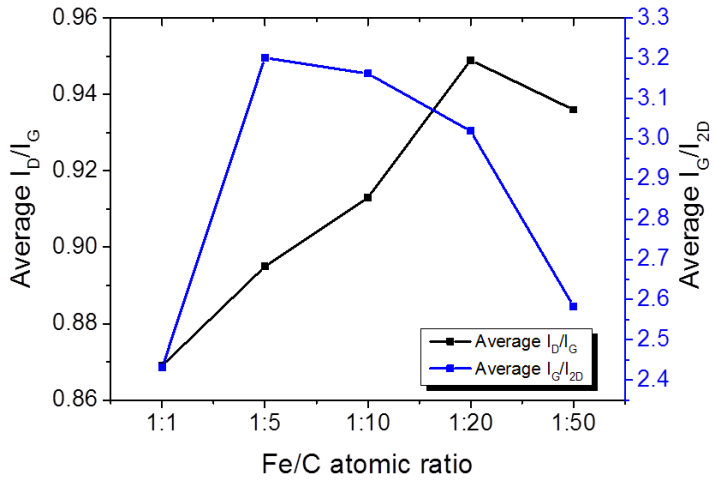

Figure 4.21. Plot of I_D/I_G and I_G/I_{2D} ratios against Fe/C atomic ratios derived from **Table 4.7**.

As the concentration of carbon in the starting material increased, the intensity ratio I_D/I_G also increased, indicating that more defects were appearing in the graphene plane. In the meanwhile, the intensity ratio I_G/I_{2D} first increased when the ratio of Fe to C changed from 1:1 to 1:5 but continued to go down when more carbon was added. Namely, the number of layers in the produced graphene was first increased and then decreased.

In summary, when the ratio of Fe/C varied from 1: 5 to 1: 50, as the carbon concentration increased, thinner graphene with more defects was produced. And when the Fe/C ratio changed from 1:1 to 1:5, graphene produced became thicker and

more defective.

4.4 Discussion of the results

In this chapter, the routes of fabricating 2D/3D graphene via catalytic graphitisation of glucose with $FeCl_3$ were introduced and explored in detail.

2D graphene film and 3D graphene foam were successfully synthesised with glucose as the solid carbon source and ferric $FeCl_3$ as the metal salt catalyst. NaCl was also introduced in 3D graphene fabrication, acting as a template for the porous foam structure.

The samples were further cleaned and characterised with various techniques, including SEM, EDS, TEM, Raman and XRD.

In 2D graphene synthesis, spin-coating was a practical approach to reduce agglomerations of precursors on flat surfaces, leading to more consistent growth of 2D graphene.

Single-step heat treatment resulted in a smoother surface with random holes, while multi-step heat treatment resulted in a less uniform but fully covered surface.

With closer observation, burst blister marks were found at the surface of samples which were annealed with a single-step heat treatment programme. The marks were believed to be left by gas molecules produced during the reaction when they escaped. These cracks impaired the structural integrity of graphene, which led to a significant drop in graphene's fracture toughness. It was later verified in the process of 3D graphene fabrication, as the samples annealed under a single-step heating programme all collapsed during the heat treatment. In contrast, the samples annealed under a multi-step heating programme all maintained their shapes throughout the annealing.

The generation of iron oxides was confirmed by EDS and Raman analyses. This implied

a successful reduction of $FeCl_3$ during the annealing. The reduced particles of iron could act as catalysts as well as irregular-shaped substrates for graphene growth. After a sample cleaning with dilute hydrochloric acid, most iron oxide particles were effectively removed, but some residues were still observed and detected trapped in graphene wrinkles or enclosed by graphene.

The products showed features that are characteristic of graphene in terms of their molecular vibrational mode. However, there was also evidence for the presence of defects in produced graphene, which might be associated with the oxygen detected. The content of defects in the synthesised products is comparable to but still lower than the content of defects measured in reduced graphene oxide. 2D graphene layers produced this way were thick, which is reflected by the EM images as well as the high values of I_G/I_{2D} ratios in Raman spectra.

In the process of 3D graphene fabrication, all the samples that were heat-treated with the single-step programme collapsed after the treatment, while all the samples that went through the multi-step programme survived the heat treatment and maintained the pellet shape.

Sample cleaning in dilute hydrochloric acid was followed by a second-round cleaning in deionised water to remove both iron oxide and NaCl.

The porous structure of the fabricated 3D graphene was confirmed by microscopy. The interconnected graphene membrane was thin, highly transparent, indicating a relatively low number of stacked layers.

A lower I_G/I_{2D} ratio achieved in Raman analysis also demonstrated that graphene synthesised in 3D foams was generally thinner than the 2D graphene grown on silicon wafers. Besides, no residue of NaCl or Fe was spotted or detected.

The graphitic structure of 3D foams was confirmed by XRD, with a broad (002) peak

present around 2θ = 21.5° to 2θ= 25.7°. The lattice spacing was increased when carbon concentration in starting material was increased.

Raman data showed us that, generally, when more carbon was added to the starting material, more defects were introduced, and the graphitic stacking structure was gradually lost with one exception when the I_G/I_{2D} increased with the increase in C/Fe ratio from 1:1 to 5:1, which indicated that the number of graphene layers was increased or the stacking structure was enhanced.

Taking all the evidence presented into consideration, here, we propose a possible mechanism of graphene growth with glucose and ferric chloride via graphitisation.

At high temperatures, with the assistance of reducing gas H_2 in the reaction chamber, $FeCl_3$ can be reduced to Fe and act as a 'Ni system' catalyst for glucose.

Carbon atoms in glucose near the surface of Fe particles will give up their original bonds with H or O and be absorbed by Fe. However, Fe can only absorb a certain amount of carbon. Therefore, when the carbon concentration reaches the maximum, to the excessive carbon, the catalytic effect of Fe is lost.

Carbon atoms that diffused into Fe will precipitate onto the Fe surface and form a membrane around Fe particles, upon cooling. Since the particles are cold-pressed into pellets, surfaces of Fe particles may touch, leading the carbon atoms to form an interconnected structure inside the pellet. When the amount of Fe is sufficient and no excessive glucose is present, high-quality graphene with low defect density can be obtained.

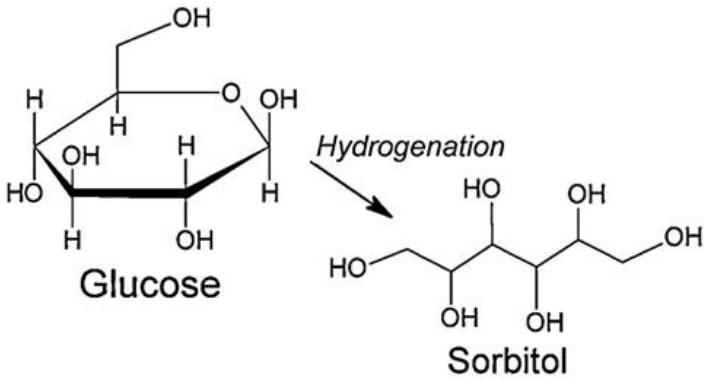

Figure 4.22. Schematic of glucose hydrogenation [13].

As carbon concentration increases, even though H_2 can also help reduce the glucose, it can only convert the aldehyde group (-CHO) in glucose to a primary hydroxymethyl ($-CH_2OH$) group, -OH will stay attached to carbon [13].

A schematic diagram of graphene growth at Fe surface with excessive glucose is shown in **Figure 4.23**. Upon cooling, excessive glucose may take up the sites where the absorbed carbon tends to precipitate, blocking some 'paths' for carbon to diffuse, thus leaving 'holes' in the graphene grown. Thus, as the number of graphene layers increases, the number of vacancy-type defects detected will also increase since such vacancies will appear in each graphene layer as the growth continues. However, graphene may override the glucose and form a layer over it when the graphene is thicker than the dimensions of these glucose molecules. From then on, since the maximum number of vacancy-type defects is reached, the detected defect density will be decreased.

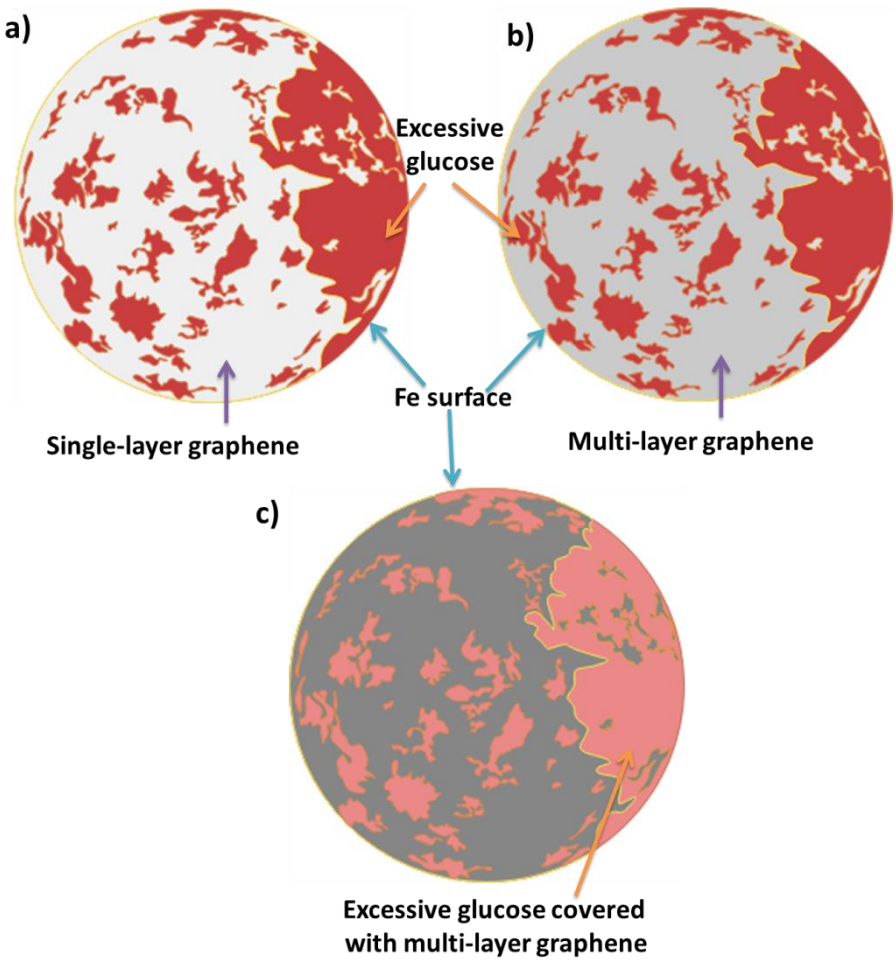

Figure 4.23. Schematic diagram of graphene growth at Fe surface with the presence of excessive glucose. Excessive glucose (red) at Fe surface has blocked the path for some carbon atoms to precipitate. Therefore, graphene (grey) will only grow within the uncovered regions. With the increase of precipitated carbon atoms, a) single-layer graphene (light grey) turns into b) multi-layer graphene (slightly darker grey). c) As the graphene layer gets thicker (dark grey), it may override the glucose and form a layer over glucose (muddy red).

Moreover, the excessive molecules and groups at metal surfaces may further interact with the precipitated carbon, especially when the number of precipitated layers is still low.

As reviewed in Chapter 2.1.3, single-layer graphene exhibits high activity at irregular sites such as its edges, defective sites, and wrinkles. In our case, the iron surface can be regarded as a bent substrate. Depending on each iron particle's size and surface

morphology, the extent of bending may vary, but that will always cause distortions in synthesised graphene, which can also make the surface of graphene more active.

This proposed interpretation can explain the shifts in XRD peaks and changes in intensity ratios of Raman peaks.

As the carbon concentration increases, there will be more excessive glucose hindering the growth of graphene on iron surfaces. More molecules or groups will interact with the synthesised graphene, forming an increased number of defects on the graphene membrane and opening up the interlayer spacing of graphene by intercalating or doping. As a result, the (002) related lattice spacing measured in XRD increased as more carbon was added. In addition, the stacking structure was also gradually lost as intercalation went on, causing a decrease in I_G/I_{2D} ratio. These interactions will all increase the defect density in graphene; hence, an increased I_D/I_G was also measured. The exception in the downward trend of I_G/I_{2D} ratio may occur when the carbon concentration was insufficient at the beginning, where the growth may suffer an under-coverage issue at some locations and result in a low I_G/I_{2D}.

References

[1] Deegan, R.D., Bakajin, O., Dupont, T.F., Huber, G., Nagel, S.R. and Witten, T.A., 1997. Capillary flow as the cause of ring stains from dried liquid drops. *Nature*, *389*(6653), pp.827-829.

[2] Streltsov, S. S., Shorikov, A. O., Skornyakov, S. L., Poteryaev, A. I., & Khomskii, D. I., 2017. Unexpected 3+ valence of iron in FeO 2, a geologically important material lying “in between” oxides and peroxides. *Scientific Reports*, *7*(1), 1-6.

[3] Glasscock, J. A., Barnes, P. R. F., Plumb, I. C., Bendavid, A., & Martin, P. J., 2008. Structural, optical and electrical properties of undoped polycrystalline hematite thin films produced using filtered arc deposition. *Thin Solid Films*, *516*(8), 1716-1724.

[4] Mos, Y. M., Vermeulen, A. C., Buisman, C. J., & Weijma, J., 2018. X-ray diffraction of iron containing samples: The importance of a suitable configuration. *Geomicrobiology Journal*, *35*(6), 511-517.

[5] Razmjooei, F., Singh, K. P., Bae, E. J., & Yu, J. S., 2015. A new class of electroactive Fe- and P-functionalized graphene for oxygen reduction. *Journal of Materials Chemistry A*, *3*(20), 11031-11039.

[6] Kim, B. J., Lee, D. U., Wu, J., Higgins, D., Yu, A., & Chen, Z., 2013. Iron-and nitrogen-functionalized graphene nanosheet and nanoshell composites as a highly active electrocatalyst for oxygen reduction reaction. *The Journal of Physical Chemistry C*, *117*(50), 26501-26508.

[7] Rao, F. B., Almumen, H., Fan, Z., Li, W., & Dong, L. X., 2012. Inter-sheet-effect-inspired graphene sensors: design, fabrication and characterization. *Nanotechnology*, *23*(10), 105501.

[8] Ferralis, N., 2010. Probing mechanical properties of graphene with Raman spectroscopy. *Journal of Materials Science*, *45*(19), 5135-5149.

[9] Nuvoli, D., Valentini, L., Alzari, V., Scognamillo, S., Bon, S. B., Piccinini, M., ... & Mariani, A., 2011. High concentration few-layer graphene sheets obtained by liquid phase exfoliation of graphite in ionic liquid. *Journal of Materials Chemistry*, *21*(10), 3428-3431.

[10] Sher Shah, M. S. A., Park, A. R., Zhang, K., Park, J. H., & Yoo, P. J., 2012. Green synthesis of biphasic TiO_2–reduced graphene oxide nanocomposites with highly enhanced photocatalytic activity. *ACS Applied Materials & Interfaces*, *4*(8), 3893-3901.

[11] Gong, Y., Li, D., Fu, Q., & Pan, C., 2015. Influence of graphene microstructures on electrochemical performance for supercapacitors. *Progress in Natural Science: Materials International*, *25*(5), 379-385.

[12] Johra, F. T., Lee, J. W., & Jung, W. G., 2014. Facile and safe graphene preparation on solution based platform. *Journal of Industrial and Engineering Chemistry*, *20*(5), 2883-2887.

[13] Kupiainen, L., Ahola, J., & Tanskanen, J., 2011. Kinetics of glucose decomposition in formic acid. *Chemical Engineering Research and Design*, *89*(12), 2706-2713.

Chapter 5 Growing graphene with polyacrylonitrile (PAN) and copper (Cu)

5.1 Introduction

In our previous study of growing graphene with ferric chloride ($FeCl_3$) and glucose, both 2D and 3D graphene were successfully synthesised with a simple and straightforward procedure. However, though the quality of as-synthesised graphene is comparable to that of typical rGO products, it is believed some adjustments can still be made to achieve higher quality 2D/3D graphene via catalytic graphitisation of solid carbon sources.

The limitations of our previous study are demonstrated below:

i) Iron salt was used as the metal catalyst. It is a “Ni system” catalyst in which carbon has high solubility. This implies that the quality, more specifically, the number of layers of graphene obtained through the heat treatment, primarily depends on the cooling rate. However, the cooling rate is not to be controlled with our Vecstar 5 tube furnace, as there is no cooling system installed with this equipment. That might have been the direct cause of the multi-layer graphene structure, which was confirmed through characterisations. To tackle this problem, we decided to exploit the mechanism under the other category of catalytic graphene growth, by using Cu as the catalyst instead of Fe because graphene grown on flat 2D copper substrates is usually self-limited to be one-atom thick. It can be a test for the feasibility of adapting this method to 3D graphene fabrication. Cu with different particle sizes (420 µm, 180 µm and 1 µm) were used in the following experiment.

ii) The graphene foams fabricated in the previous study had low toughness, which

has led to an easy fracture. It is believed that the gas molecules produced during the heat treatment will break the structure when they try to escape. This time, we attempt to solve the problem by substituting the carbon source in the starting material. PAN, being the most common precursor used in the carbon fibre industry for its superior stability and strength, was chosen to be the solid carbon source for our following study. According to Manocha's work, published in 1996, after being thermally pre-oxidised at low temperatures (usually 180 °C ~270 °C), PAN will exhibit high yield and superior mechanical properties [1]. Pre-oxidised PAN may enable the pellets to maintain their shapes during the heat treatment. That can also benefit the graphitisation process, as it will make the carbon source and the metal catalyst to be in better contact. Also, since PAN degrades before melting, it can be treated at rather high temperatures.

5.2 Reselecting materials for graphene growth

As described in the last section, PAN and Cu have been selected as the solid carbon source and metal catalyst for catalytic graphene growth. Still trying to take advantage of the material's liquid form in pursuit of better dispersion, a simple solubility test was performed in order to find a suitable organic solvent for PAN. In the test, 0.5 g of PAN was added to 10 ml of acetone, chloroform, DMF, and anisole, respectively. The solutions were heated to 50 °C and stirred in a magnetic stirrer for several hours. Observations were made afterwards, and DMF was the only solvent that dissolved PAN within 2 hours. As a result, DMF was chosen to be the solvent for PAN in the next step of sample preparation.

5.3 Adjusted fabrication routes

Since the starting materials were changed, the mechanism behind the graphene

growth was also altered. The procedures should be tailored to support the graphene synthesis with PAN and Cu specifically.

5.3.1 Mixing and pelletising of materials

Half a gram of PAN was first dissolved in 10 ml of DMF. The solution was then mixed with 1 g of NaCl and 1 g of Cu of various particle sizes (420 µm, 180 µm and 1 µm). The particles of Cu and NaCl were all wrapped by the PAN/DMF solution and formed a gel-like mixture. Without removing the solvent, the particles, covered with viscous carbon precursor, were directly cold-pressed into a pellet under a pressure of 10 megapascals (MPa) for 10 minutes. DMF was then removed by drying in the oven at 60 °C for several hours until the samples were thoroughly dried.

5.3.2 Pre-oxidation of PAN

Pellets were thermally oxidised in air at 270 °C for 2 h. The heating rate was 5 °C per minute. The pre-oxidation was carried out in High-Temperature Laboratory Oven – LHT (Carbolite Gero Ltd., UK).

5.3.3 Removal of sodium chloride

NaCl has a melting point of 801 °C, which is lower than the intended heat treatment temperatures for the graphitisation of PAN at the next step of this experiment. Therefore, NaCl was opted to be removed before the high-temperature treatment.

NaCl was removed by dissolving the pellets in deionized water. The deionized water was refilled frequently for two days. The pellets were then dried in an oven again at 60 °C for several hours. By this stage, pre-oxidation of the interconnected PAN in pellets should have already stabilised the pellet structure. Therefore, even if the pore-forming template NaCl was removed, the pellets still maintained their shapes.

5.3.4 Heat treatment

All the heat treatments were performed in a Vecstar 5 tube furnace with a mixed gas flow of 95% Ar and 5% H_2. The gas flow rate was set at 200 sccm throughout the heat treatment. Samples were gradually cooled down to room temperature with a continuous flow of Ar/H_2 to avoid the occurrence of oxidation in this stage.

The variables introduced were: 1) graphitisation temperature (900 °C and 1000 °C); 2) graphitisation time (1 h and 2 h); and 3) heating programmes (single-step and multi-step). Details of the heating programmes are given below:

Programme 1: the temperature was increased at a rate of 5 °C per minute from room temperature to 900 °C or 1000 °C and was maintained for 1-2 h for graphene growth before the furnace was cooled down to room temperature.

Programme 2: The temperature was first increased at a rate of 5 °C per minute from room temperature to 200 °C and was kept at this temperature for 1 h. The temperature was then raised from 200 °C to 600 °C at the same rate and was maintained for another hour before being brought to 900 °C or 1000 °C again, at the rate of 5 °C per minute. After a 1 h or 2 h growth of graphene, the power supply for the furnace was shut down, and samples were cooled to room temperature.

5.3.5 Copper removal

Copper residues in the pellets were removed by first immersing the pellets in 500 ml of 1 mol $FeCl_3$/ 10% HCl water solution for 2 days and then in 10 % HCl solutions for another two days in order to remove the Fe produced in the previous step. The 10 % HCl was prepared by slowly and carefully adding 270 ml of 37% HCl to about 500 ml of distilled water in a volumetric flask with constant swirling to ensure the acid was evenly mixed. Then more distilled water was added until the level just reached the

one-litre mark on the flask. Finally, 162.204 grams of anhydrous $FeCl_3$ was dissolved in the diluted acid.

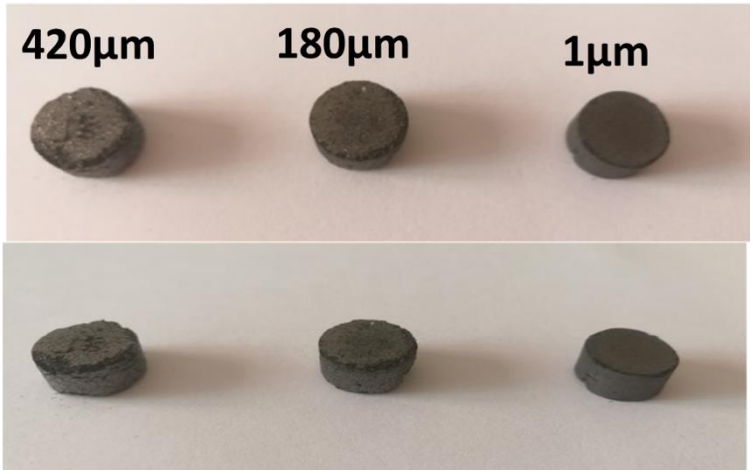

Figure 5.1. Photo images of washed samples prepared with 420 µm (left), 180 µm (middle) and 1 µm (right) Cu particles. All three samples were produced after single-step heat treatment at 1000 °C for 2 h.

Unlike the 3D products synthesised with glucose and $FeCl_3$, the structure of most graphene foams produced with PAN and Cu did not collapse throughout the washing (**Figure 5.1**). Therefore, ultrasonication was not involved in this step, so unnecessary damage to the synthesised products was avoided. However, that has also made the removal of residues more challenging than before. This is because reactions between metal particles and ions only occur when they are in contact, which requires the ions in solution to travel or permeate through the micro-porous and macro-porous structures in graphene foam to reach the wrapped metal particles. Therefore, the washing process in this synthesis took far more time than in the previous study.

The reactions involved can be described by the following chemical equations:

$$3\,Cu(s)\ +\ FeCl_3(aq)\ \rightarrow\ Fe(s)\ +\ 3\,CuCl(aq);$$

$$Fe\ (s)\ +\ 2\,HCl\ (aq)\ \rightarrow\ FeCl_2(aq)\ +\ H_2\ (g).$$

The process was repeated 3-5 times until the majority of the copper residues were removed. Pellets were then dried in an oven at 60 °C. After this process, samples were ready for characterisation.

Photo images in **Figure 5.1** also provided surface morphological information about the synthesised graphene foams. After being thoroughly cleaned with iron chloride and hydrochloric acid, the samples maintained substantially the same shape. From left to right, samples were prepared with smaller and smaller Cu particles. And the foam showed an increased ability to resist structural damage during the washing when Cu particle size decreased.

Three samples collapsed during the washing. They were prepared with: 1) 420 μm copper, single-step heat treatment at 1000 °C; 2) 180 μm copper, single-step heat treatment at 1000 °C; and 3) 420 μm copper, multi-step heat treatment at 1000 °C.

Proposed explanations were made upon the evidence above:

i) Different chemical reactions usually take place when different conditions are met. In terms of temperature-sensitive reactions, when the temperature is gradually increased, they should occur in succession, split by the different temperature ranges preferred by each individual reaction. However, when the heating is rapid and no pause is made, it allows several reactions to initiate within a short time. As observed and studied in our previous work on the synthesis of graphene with glucose and ferric chloride, the gases released during the heat treatment played an important role in deciding the sample's structural and mechanical properties. If reactions that involve the release of gases all occur at once, a large number of gas molecules will be produced within a short time. The porous structured foam can be viewed as a container or cage for the gas molecules. With the increased gas concentration, gas molecules will hit the 'walls' around them more frequently and violently. As a

result, the gas molecules will crack some surfaces, and, as was reviewed in Chapter 2.1.3, cracked graphene will experience a rapid brittle fracture at significantly lower stress. In another way, when multi-step heat treatment is employed, fewer reactions will occur at the same time, which allows gas molecules to find more mild ways to escape, the structures of samples can be efficiently preserved.

ii) When the Cu particles used are too large, Cu particles will interconnect with each other and become the framework of the foam structure. Therefore, when Cu is removed during the washing step, the essential supporting structure is also removed, the foam will collapse rapidly.

The interpretation above implies that the risk of sample collapsing may be reduced by using smaller Cu particles and running the heat treatment with multi-step programmes.

5.4 Results

5.4.1 Morphological and chemical analyses

5.4.1.1 Influence of heat treatment temperature

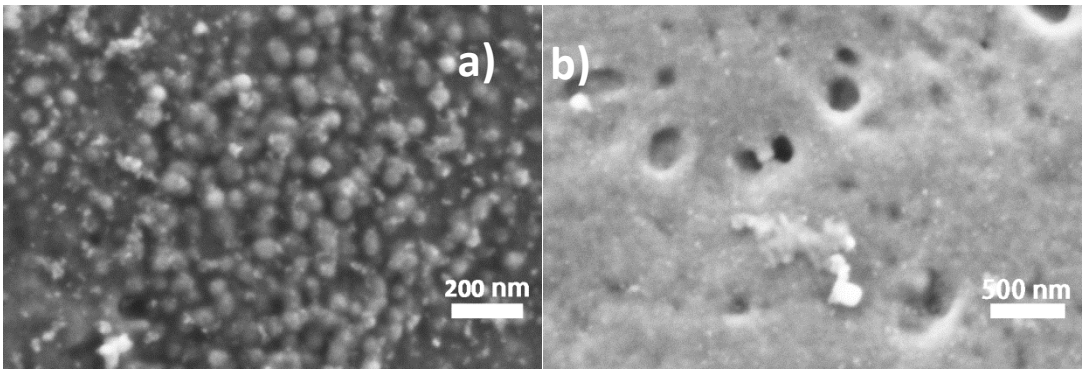

Figure 5.2. SEM images of sample surfaces. Samples were prepared with 180 µm Cu, multi-step heat treatment at a) 900 °C and b) 1000 °C for 2 h.

Figure 5.2 shows the surfaces of two samples imaged under SEM. Both samples were prepared with 180 µm Cu and heat treatment programme 2 for 2 h. The heat treatment temperature was 900 °C for the sample in **Figure 5.2** a) and 1000 °C for the sample in **Figure 5.2** b).

Higher heat treatment temperature has resulted in a smoother sample surface. Grains with diameters around 100 nm can be observed on the surface of the sample, which was heat-treated at a lower temperature. Point scans were performed on SEM-EDS to identify the elemental composition of the particles.

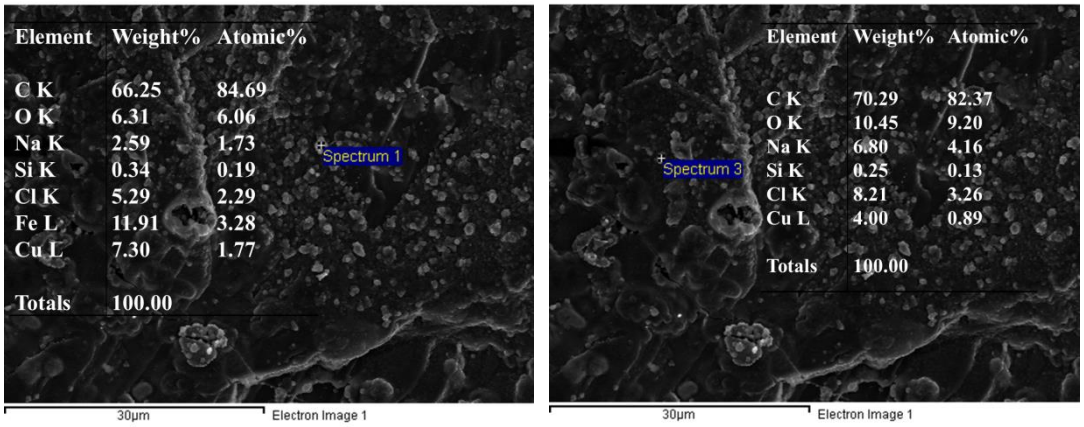

Figure 5.3. EDS point scan images and chemical composition tables of bright particles on the surface of the sample in **Figure 5.2**a).

According to the point scan results displayed in **Figure 5.3**, the dominant element detected was carbon. It suggests that most of the impurities, such as NaCl crystals and Cu particles have been sufficiently removed, and the rough surface in **Figure 5.3** a) is more likely to be a result of patched graphene domains rather than residues. With further heating, the domains will grow and finally merge with other domains in the vicinity to form a more extensive, patched domain. This graphene formation mechanism is in agreement with the mechanism of CVD graphene growth on Cu substrates [2]. It can be interpreted that, at 1000 °C, more energy was provided to the system than at 900 °C, which effectively accelerated the reactions as well as domain growths on copper surfaces. As a result, larger domains were formed at higher temperatures, and a smoother surface was obtained.

Figure 5.4 compares the D peaks and G peaks of the Raman spectra acquired for these two samples. As the heat treatment temperature increases, an increase of G peak relative to the D peak occurs.

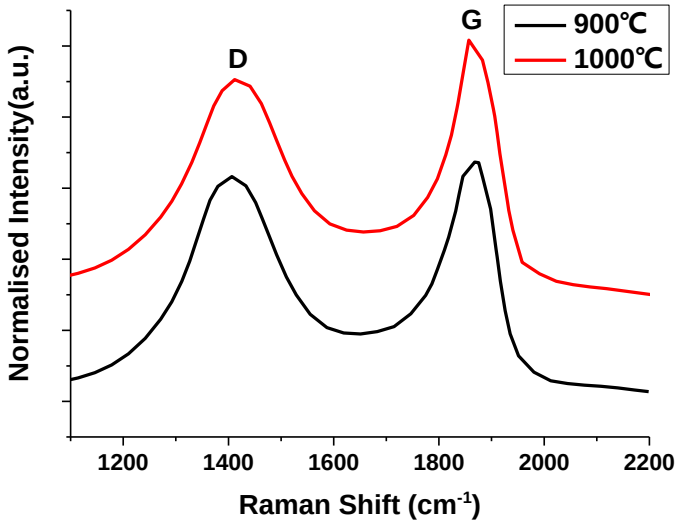

Figure 5.4. Raman spectra of samples prepared with 180 µm Cu, multi-step heat treatment at 900 °C (black) and 1000 °C (red) for 2 h.

Table 5.1. Summary of the key fabrication parameters and Raman spectra I_D/I_G ratios of samples in **Figure 5.2**.

Copper size (µm)	Programme	Temperature (°C)	Time (h)	I_D/I_G
180	2	900	2	0.969
180	2	1000	2	0.872

Table 5.1 lists the key parameters for samples in **Figure 5.2** and the correspondent I_D/I_G ratios calculated from the Raman spectral data of these samples. As the temperature increased, I_D/I_G decreased, indicating a higher graphitisation level and lower defect density. The I_D/I_G ratio is also related to domain size in graphene. When domain size decreases, more 'edges' will appear within the area of a Raman scan, resulting in a higher defect density and larger I_D/I_G ratio.

5.4.1.2 Influence of heat treatment programme

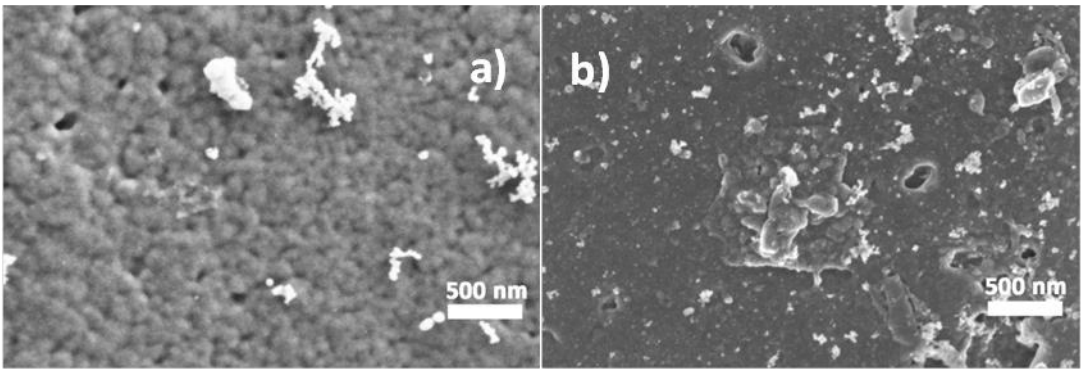

Figure 5.5. SEM images of sample surfaces. Samples were prepared with 1 µm Cu, a) single-step heat treatment or 2) multi-step heat treatment at 1000 °C for 1 h.

Figure 5.5 compared the samples obtained with single-step heat treatment (**Figure 5.5** a)) and multi-step heat treatment (**Figure 5.5** b)). The two samples were both made with 1 µm copper particles and synthesised at 1000 °C for 2 h. Single-step heat treatment has resulted in a rough surface with clearer and smaller graphene domains. In the meanwhile, the dwells in multi-step heat treatment may have granted the domains more time to absorb energy from the system and grow in size.

Table 5.2. Summary of the key fabrication parameters and Raman spectra I_D/I_G ratios of samples in Figure **Figure 5.5**

Copper size (µm)	Programme	Temperature (°C)	Time (h)	I_D/I_G
1	1	1000	1	0.874
1	2	1000	1	0.979

The I_D/I_G ratio summarised in **Table 5.2** showed that, when multi-step heat treatment was performed, the defect density of the produced graphene was increased. However, the SEM images of multi-step heat-treated samples showed a smoother surface. Therefore, other factors that influenced the defect density level in the latter sample, except for its domain size, need to be further investigated.

5.4.1.3 Influence of copper particle size

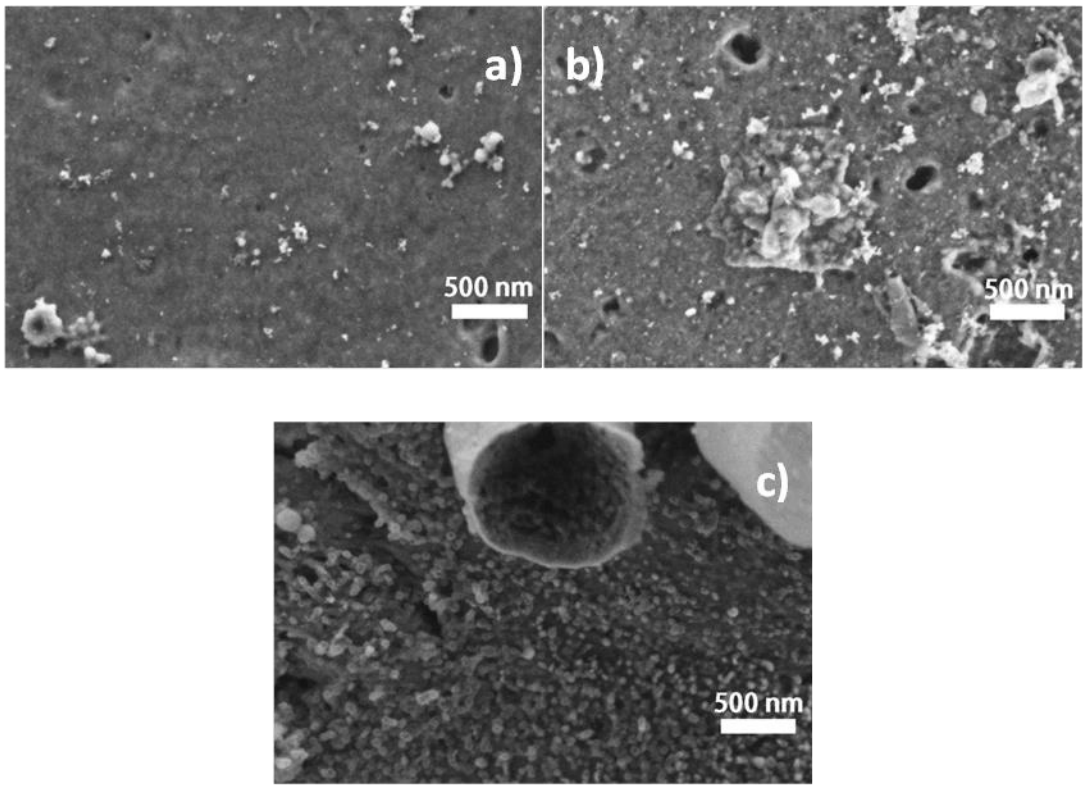

Figure 5.6. SEM images of samples prepared with a) 420 µm, b) 180 µm and c) 1 µm copper particles. The samples were all heat treated with programme 2 at 1000 °C for 2 h.

Figure 5.6 compared the sample surfaces prepared with different sized Cu particles. The samples were all heat treated under programme 2 at 1000 °C for 2 h. The first two samples were prepared with 420 µm (**Figure 5.6**a)) and 180 µm (**Figure 5.6** b)) Cu particles had similar smooth surface structures. However, as the Cu size decreased to 1 µm (**Figure 5.6** c)), a rough surface covered by nano-sized domains was achieved.

The Raman parameters in **Table 5.3** indicated that the defect density was the lowest in the 180 µm copper sample. Thus, the Raman data, together with SEM images, implied that 180 µm was the best catalyst size among the three for achieving less-defected larger-domain graphene.

Table 5.3. Summary of the key fabrication parameters and Raman spectra I_D/I_G ratios of samples in **Figure 5.6**

Copper size (μm)	Programme	Temperature (°C)	Time (h)	I_D/I_G
420	2	1000	2	0.913
180	2	1000	2	0.872
1	2	1000	2	0.905

5.4.1.4 Influence of soaking time

Samples in **Figure 5.7** were all treated with programme 2 at 1000 °C. Samples in **Figure 5.7** a) and **Figure 5.7** b) were prepared with 180 μm Cu particles, while samples in **Figure 5.7** c) and **Figure 5.7** d) were made up with 1 μm Cu particles. Samples on the left were heat-treated for 1 h, while samples on the right were treated for 2 h.

For the 180 μm Cu samples, longer heat treatment time granted the sample larger graphene domains and a smoother surface, which is in accordance with the assumption we made about the connection between the energy input and domain growth. However, when the sample with smaller copper catalysts was heat-treated for a longer time, the domain sizes in graphene was decreased, which is the opposite of our assumption. In Schwarz's work [3], a reappearance of graphene domains was observed upon cooling. They have attributed this phenomenon to the presence of internal energy.

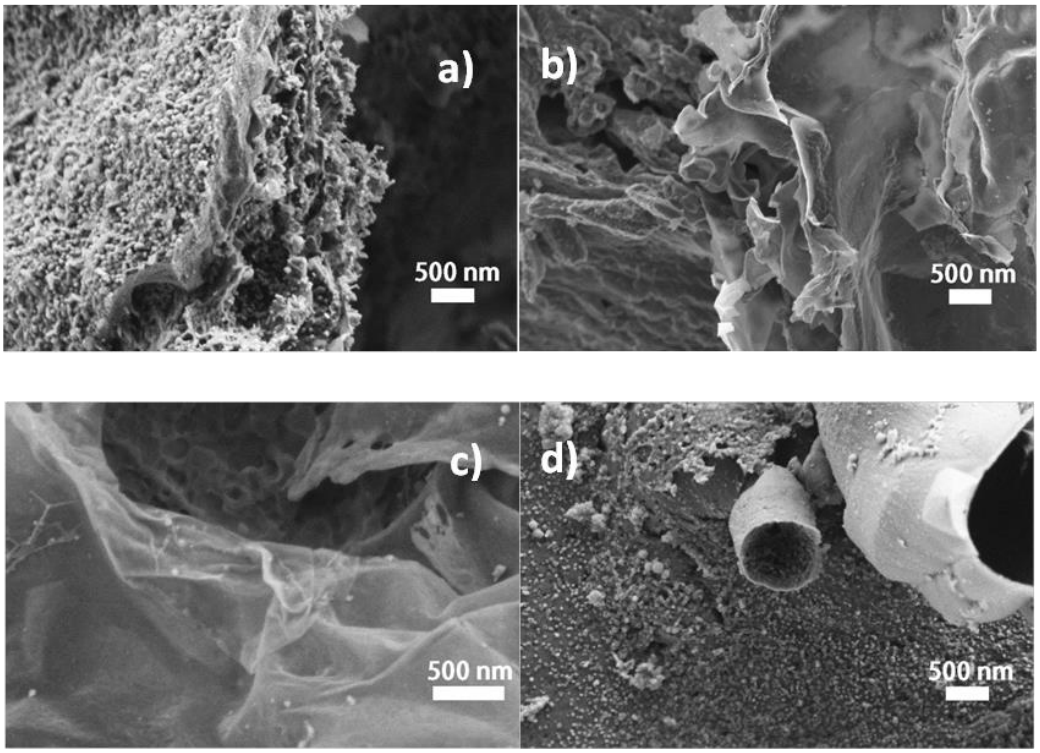

Figure 5.7. SEM images of sample surfaces. Key parameters for each sample are: a) 180 µm Cu, 1000 °C, programme 2, 1 h; b) 180 µm Cu, 1000 °C, programme 2, 2 h; c) 1 µm Cu, 1000 °C, programme 2, 1 h; and d) 1 µm Cu, 1000 °C, programme 2, 2 h.

The values of I_D/I_G ratio summarised in **Table 5.4** indicated that longer heat treatment would result in less-defected structure in graphene for both 180 µm copper samples and 1 µm copper samples.

Table 5.4. Summary of the key fabrication parameters and Raman spectra I_D/I_G ratios of samples in **Figure 5.7**

Copper size (µm)	Programme	Temperature (°C)	Time (h)	I_D/I_G
180	2	1000	1	0.953
180	2	1000	2	0.872
1	2	1000	1	0.979
1	2	1000	2	0.905

5.4.2 Internal structural information

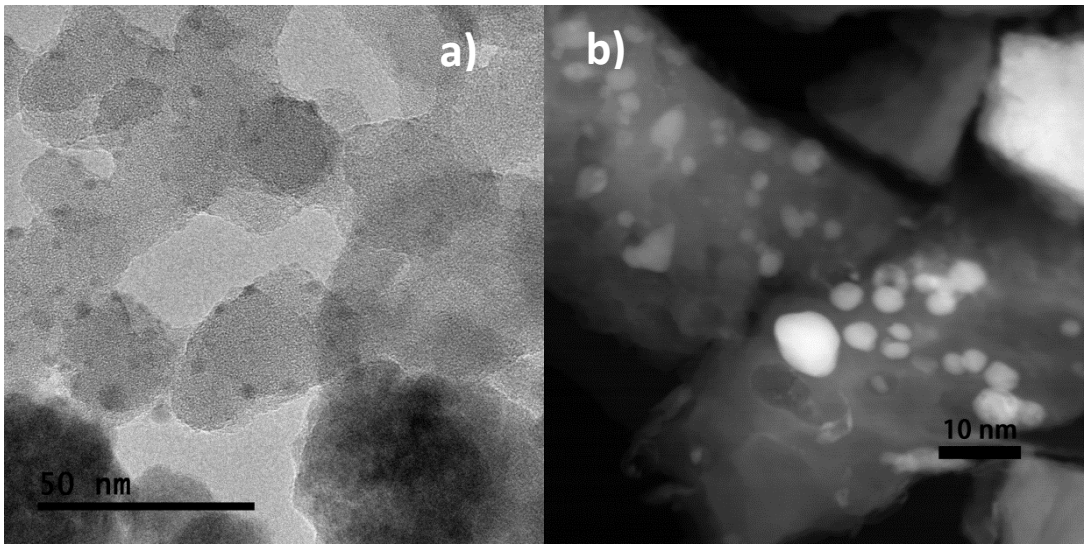

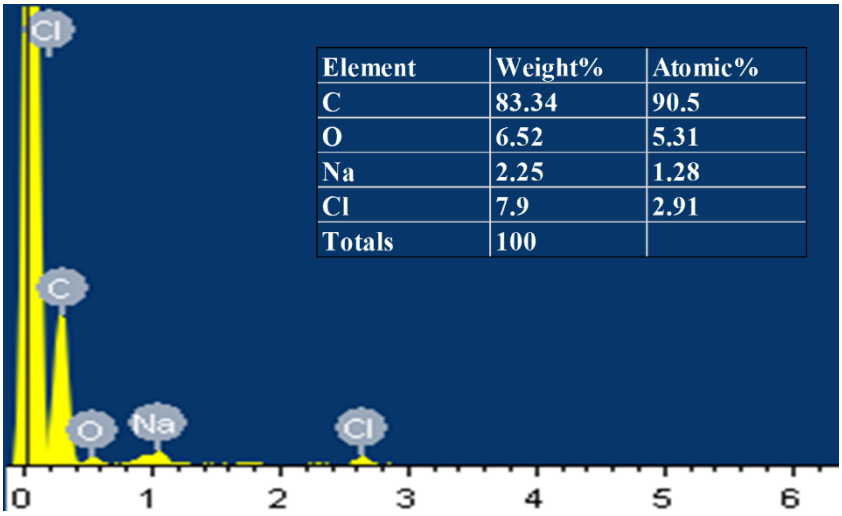

Element	Weight%	Atomic%
C	83.34	90.5
O	6.52	5.31
Na	2.25	1.28
Cl	7.9	2.91
Totals	100	

Figure 5.8. a) TEM and b) dark-field images of the sample prepared with 180 µm Cu at 1000 °C for 1 h with programme 2. c) EDS spectrum with the elemental composition analysis of the bright region in b).

Figure 5.8 a) confirmed the porous structure of a cleaned sample. The sample was prepared with 180 µm copper at 1000 °C for 1 h heat treatment under programme 2.

The dark-field image in **Figure 5.8 b)** highlighted some bright particles that remained in the structure. The EDS spectrum in **Figure 5.8 c)** further confirmed that the residues are NaCl nanoparticles wrapped in carbon shells. Although the samples have been

washed several times by deionised water, it was still not feasible to completely remove the salt and copper residues.

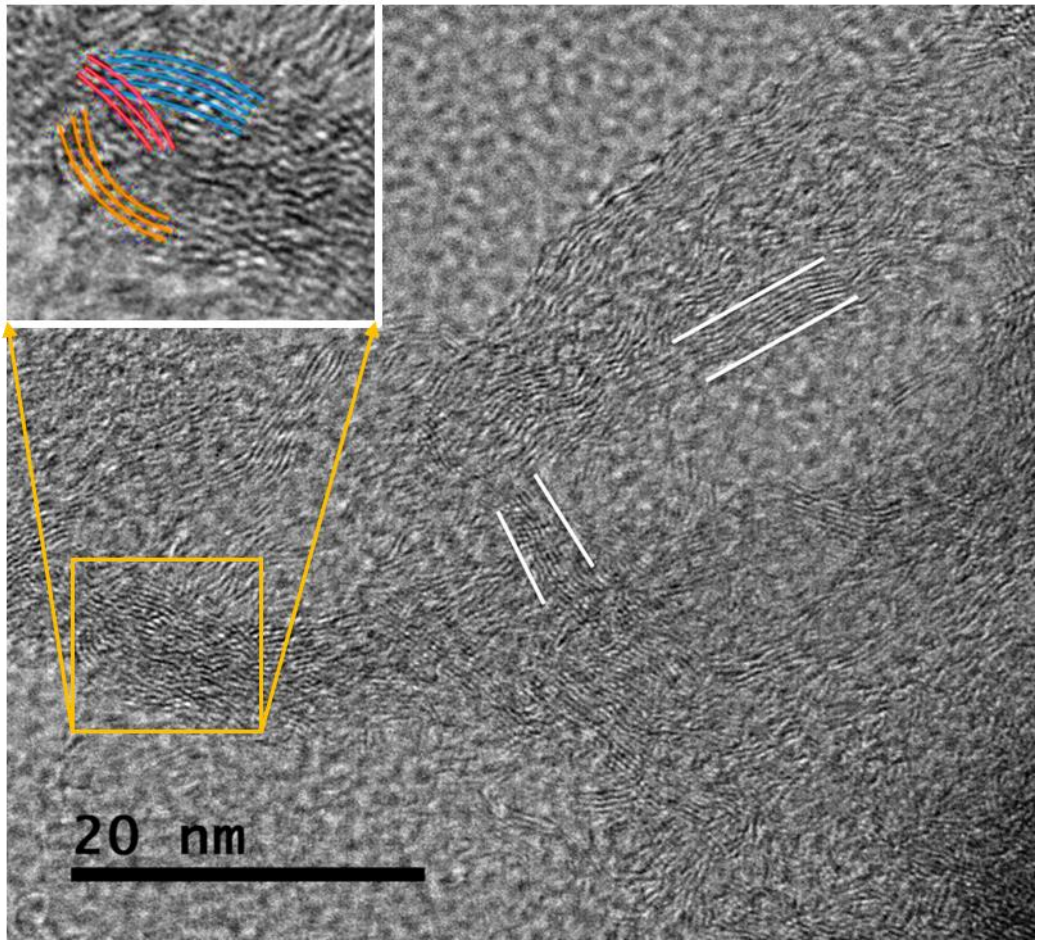

Figure 5.9. High magnification TEM image of the sample prepared with 180 μm copper at 1000 °C for 1 h with programme 2. The image in the top-left corner is an enlargement of the framed region below it.

When turning the magnification to as high as 960 K times, the lattice fringe pattern of graphene can be seen clearly, surrounding a pore structure (**Figure 5.9**). The fringe of a graphene flake resembles the fore-edge of a book. When there are several books randomly stacked in 3 dimension, the fore-edges of some books next to each other may merge and make them look like one thicker book. As is marked in the enlarged image, even though the fringes are all closely packed, the subtle differences in the shapes and directions of curvatures can still distinguish the flakes from each other. Therefore, when trying to determine the number of layers of one graphene flake

through high-resolution TEM images, the principle is to search for a set of closely aligned parallel curves. We found the fringes of at least two flakes and marked them with white lines through this method. The thicknesses were found to be around 7-8 graphene layers.

The fringes were further analysed by a line profile (**Figure 5.10**). From 0 to 1.8 nm in the line profile, there are five fringes in total. So each layer is about 0.36 nm thick, which corresponds to the spacing in bi-layer and tri-layer graphene.

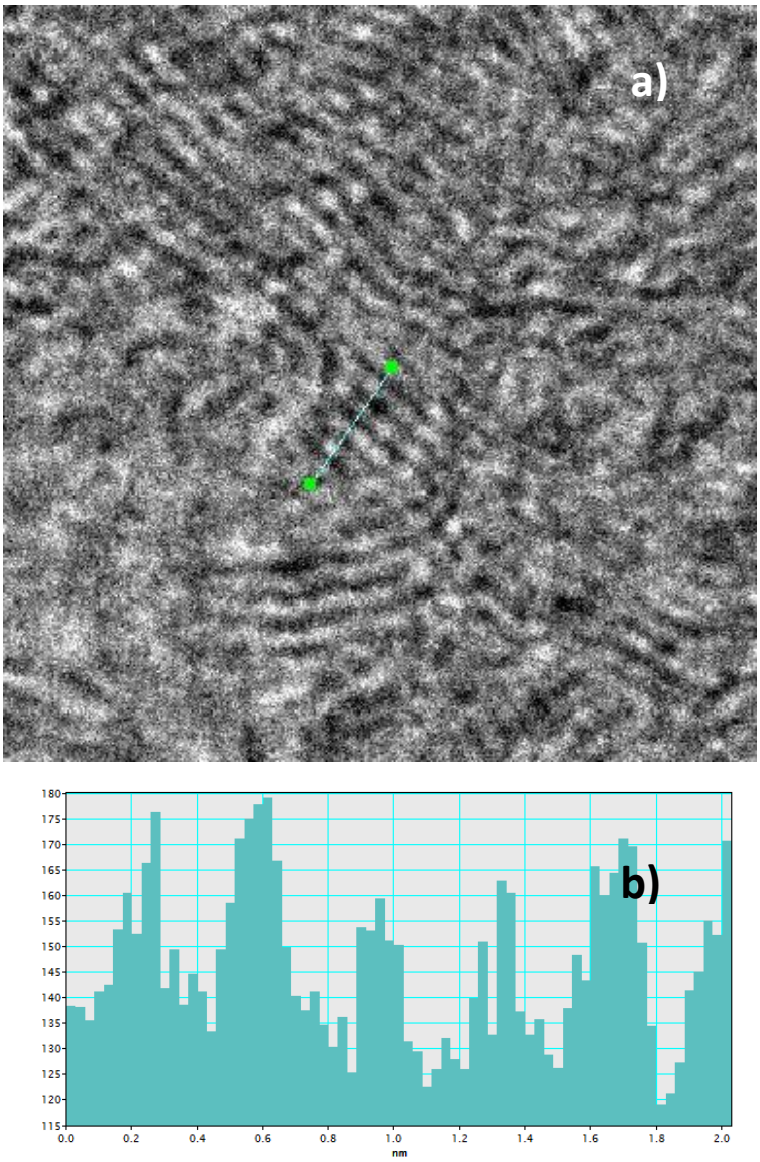

Figure 5.10. a) Enlarged TEM image of **Figure 5.9** and b) line profile of the blue line in a).

5.4.3 Chemical information

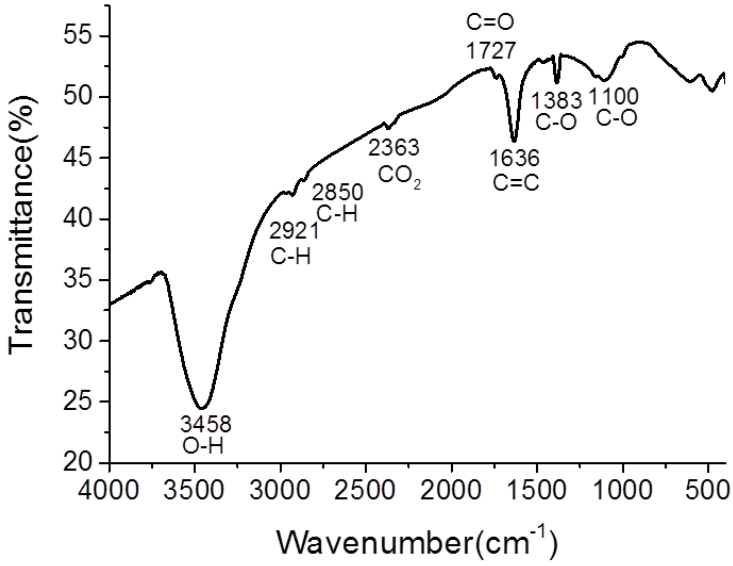

Figure 5.11. FTIR spectrum of graphene foam synthesised with 180 µm Cu at 1000 °C for 1 h with programme 1.

Figure 5.11 is a plot of the FTIR spectrum of a collapsed graphene foam. The most significant band at 3458 cm^{-1} is due to the O-H stretching vibration resulting from the water absorption [4]. 2921 cm^{-1} and 2850 cm^{-1} bands corresponded to $=CH_2$ asymmetric and symmetric stretching, respectively [5]. A tiny peak at 2363 cm^{-1} is caused by the absorption of CO_2 from the atmosphere [6]. The second significant peak at 1636 cm^{-1} corresponds to the sp^2 C=C bond expected from graphene [7]. Oxygen-containing functional groups can be revealed by the C=O and C-O bands around 1727 cm^{-1}, 1383 cm^{-1} and 1100 cm^{-1} [6].

In conclusion, the O-H group and CO_2 have mainly resulted from the moisture and CO_2 in the atmosphere; C=C bonds which should be attributed to the hybridized sp^2 bonds in the planes of graphene, are also detected, and C-O is the main functional group attached to the graphene, while there are also small traces of $=CH_2$ and C=O groups in the sample.

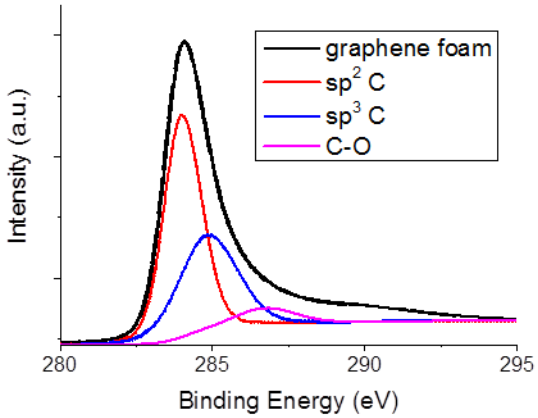

Figure 5.12. C1s XPS spectrum of graphene foam synthesised with 180 µm Cu at 1000 °C for 1 h with programme 2.

A C1s XPS spectrum of synthesised graphene foam was displayed in **Figure 5.12**. The sp^2 C peak dominated the spectrum with a high concentration of 58.7%, indicating a successful formation of in-plane covalent bonds among carbon. The sp^3 C had a concentration of 35.7%, followed by a 5.6% C-O group.

The concentration ratio of sp^2 C/ sp^3 C is 1.64, indicating that the majority of the carbon in synthesised foam was bonded to other carbon by a hybridised sp^2 bond, which is characteristic of graphene. The tiny trace of C-O may have been introduced during the liquid washing process, and its presence is in accordance with the FTIR result.

5.4.4 Surface area and pore distribution

Figure 5.13 is the N_2 sorption isotherm of the graphene foam. The curve shows type IV isotherm characteristics, which indicate that the material is mesoporous with pore diameters between 2-50 nm [8]. A hysteresis loop appears within the relative pressure range of 0.4 to 1.0. The calculated specific surface area is as large as 610 m^2/g, which is 2-3 times that of typical rGO materials.

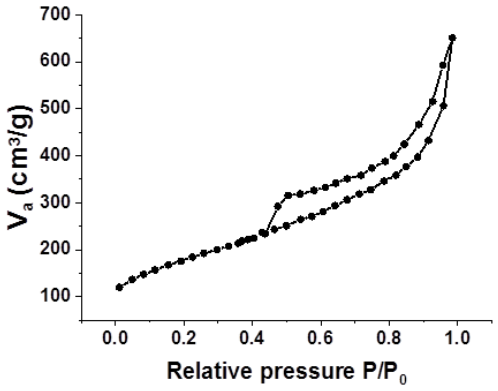

Figure 5.13. Nitrogen (N_2) sorption isotherm of graphene foam synthesised with 180 µm Cu at 1000 °C for 1 h with programme 1.

The collapsed graphene foam prepared with 180 µm Cu particles and heat treatment programme 2 for 2 h at 1000°C was sent for BET surface area and pore distribution analyses.

The pore size distribution curve in **Figure 5.14** demonstrated that most pores in the material are 12 nm in diameter with some smaller pores of 6 – 10 nm. That is in accordance with the TEM results in Chapter 5.4.2.

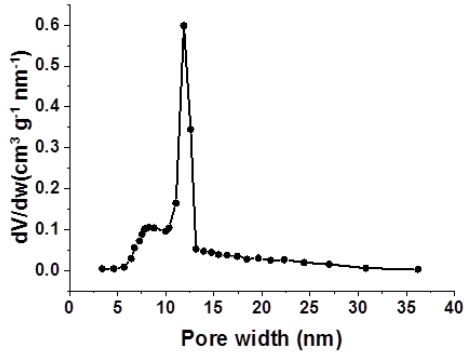

Figure 5.14. The pore distribution curve of graphene foam synthesised with 180 µm Cu at 1000 °C for 1 h with programme 1.

5.5 Discussion of the results

3D porous graphene foam has been fabricated with a successful catalytic graphitisation of PAN at 900-1000 °C under atmospheric pressure. The catalysts were Cu particles of few to hundreds of microns. Changes in heat treatment temperature, soaking time and programme all affected the surface morphology of synthesised graphene.

Generally, higher heat treatment temperature and longer soaking time are expected to provide more energy to the system in order to accelerate graphene growth. However, for the samples prepared with 1 μm Cu particles, a reappearance of domains was observed when the soaking time was increased from 1 h to 2 h.

In terms of the effect of the Cu particle size, it was found that among the samples prepared with 1 μm, 180 μm and 400 μm Cu particles, the ones synthesised with 180 μm Cu particles displayed a smooth surface structure while exhibited the least defect density. 400 μm Cu particles sometimes would lead to a sample collapse when the interconnected Cu framework was removed during the acid washing.

Functional groups attached to the synthesised graphene were mainly C-O, $=CH_2$ and C=O, which was confirmed by both FTIR and XPS analyses.

The synthesized graphene foam has a large specific surface area of 610 m^2/g, and the pores inside the material are mostly 12 nm in diameter.

Attention was drawn to the domain structure observed on sample surfaces, as the domain size is usually regarded as a key indicator of graphene quality in copper-assisted graphene growth.

In **Figure 5.8**, the interconnected structure of graphene foam was confirmed. It can also be found that the particle-like graphene is mainly 50 nm in size, with holes and

gaps of comparable sizes surrounding the graphene 'particles'.

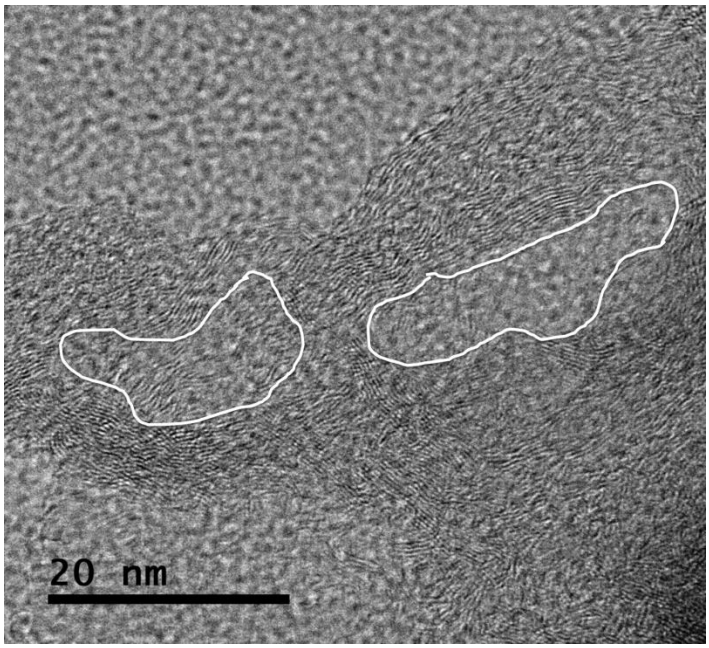

Figure 5.15. Same TEM image as in **Figure 5.9** with in-plane 'hole' structure marked.

The graphene membrane in **Figure 5.15** has two irregular-shaped holes in its plane, whose sizes are both around 20 nm. These holes cannot be the 'capsules' for Cu or NaCl particles. By 'capsule', it means there was a membrane that enclosed a particle inside and popped open when the particle was removed. Since NaCl and Cu particles are all of micron sizes, the holes in **Figure 5.15** are too tiny for these particles. Instead, the holes are more likely to be non-nucleated domains on a vast copper particle surface, as is illustrated in **Figure 5.16**.

Unlike Ni substrates, where the growth of graphene was carried out layer by layer, the growth of graphene on Cu substrate was done by filling patches. Therefore, as more graphene nucleates on Cu particle surfaces, more edges and vacancies will be introduced to the structure. Even though the growth has successfully transformed amorphous sp^3 carbon into covalent sp^2 carbon, which was confirmed by XPS analysis, the appearance of a strong D peak in Raman spectra can still occur. Therefore, the defects exhibited by D peaks in Raman spectra are rather structural than chemical.

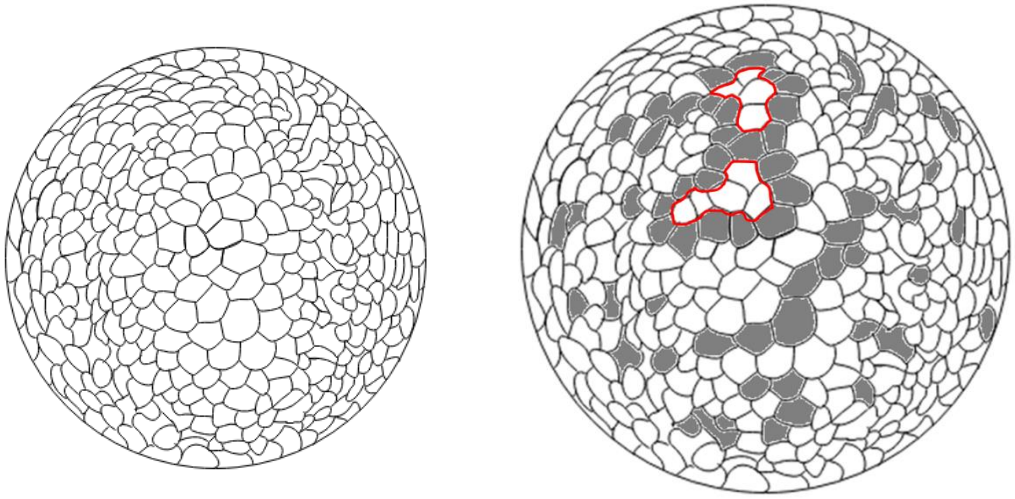

Figure 5.16. Schematic diagram of a) a micron-sized Cu particle covered with nano-sized domains and b) 'holes' (red lines) enclosed by graphene (dark grey) grown from its neighbouring domains.

It is also found that the reaction might be suffering a carbon under-coverage issue since:

i) The examined graphene membrane surfaces are not intact, with holes and graphene domains both of nano-scale observed.

ii) If the catalytic copper surface is fully covered, additional heating should not further change the sample's morphology or chemistry since the growth should be self-limited.

References

[1] Manocha, L. M., Bhatt, H., & Manocha, S. M., 1996. Development of carbon/carbon composites by co-carbonization of phenolic resin and oxidised PAN fibers. *Carbon*, *34*(7), 841-849.

[2] Mattevi, C., Kim, H., & Chhowalla, M., 2011. A review of chemical vapour deposition of graphene on copper. *Journal of Materials Chemistry*, *21*(10), 3324-3334.

[3] Schwarz, D., Henneke, C., & Kumpf, C., 2016. Towards functionalization of graphene: in situ study of the nucleation of copper-phtalocyanine on graphene. *New Journal of Physics*, *18*(2), 023034.

[4] Zhu, C., Guo, S., Fang, Y., & Dong, S. (2010). Reducing sugar: new functional molecules for the green synthesis of graphene nanosheets. *ACS Nano*, *4*(4), 2429-2437.

[5] Yang, H., Li, F., Shan, C., Han, D., Zhang, Q., Niu, L., & Ivaska, A. (2009). Covalent functionalization of chemically converted graphene sheets via silane and its reinforcement. *Journal of Materials Chemistry*, *19*(26), 4632-4638.

[6] Shen, J., Li, T., Long, Y., Shi, M., Li, N., & Ye, M. (2012). One-step solid state preparation of reduced graphene oxide. *Carbon*, *50*(6), 2134-2140.

[7] Marcano, D. C., Kosynkin, D. V., Berlin, J. M., Sinitskii, A., Sun, Z., Slesarev, A., ... & Tour, J. M. (2010). Improved synthesis of graphene oxide. *ACS Nano*, *4*(8), 4806-4814.

[8] Barron, A. R. (2015). Physical Methods in Chemistry and Nano Science.

Chapter 6 Conclusion and future work

6.1 Conclusion

In this study, 2D/3D graphene fabrication has been explored on the basis of catalytic graphitisation of solid carbon sources.

In the first part of the study, glucose and $FeCl_3$ were selected to be the solid carbon source and metal salt catalyst, respectively, for graphene synthesis. Moreover, in the fabrication of 3D graphene foam, NaCl was introduced as a template for 3D porous structures.

Spin-coating was verified to be an efficient way of uniformly dispensing Fe/C solutions onto Si substrates for homogeneous 2D graphene growth.

By controlling the heat treatment parameters such as time, temperature and programme, samples of various properties and characteristics were obtained.

The results of multiple characterisations such as SEM and TEM images, EDS, Raman and XRD spectra, were then analysed to understand the effects of different parameters on the products.

A successful reduction of $FeCl_3$ during the annealing was suggested by the Raman and EDS results. Besides, the products showed characteristics of graphene-related materials but with a presence of defects.

Focusing on the variance in chemical structures of synthesised graphene, a mechanism of graphene growth from glucose, onto the iron salt template, was proposed in Chapter 4.4.

The second part of this study investigated a polymer/metal-based graphene synthesis. Adjustments were made in the fabrication route so it can be adapted to growing

graphene with PAN and Cu particles. The solvent was changed to DMF, allowing PAN to be dissolved and dispersed between Cu and NaCl particles.

A pre-oxidation of PAN was carried out at 270 °C in order to strengthen the mechanical structure of the 3D foams. Most samples prepared this way have maintained their shapes and did not collapse throughout all the treatments.

Again, heat treatment conditions were kept under control during the graphene synthesis.

The 3D graphene foam fabricated showed a graphitised multi-layer structure under TEM imaging. The number of graphene layers observed was typically 7~8, with an average lattice spacing of 0.36 nm.

XPS spectra demonstrated that the majority of carbon atoms in the product are covalently bonded to other carbon atoms, with a high sp^2 C concentration of 58.7%.

The 3D graphene foam synthesised in this study possesses a large specific surface area of 610 m^2/g and a mesoporous structure with considerable 12 nm pores.

After the samples were treated under different conditions, the variance in graphene domain size aroused our interest, and extensive analysis was conducted focusing on the factors that may influence the formation and growth of graphene domains. A model of graphene growth on a 3D Cu substrate with nano-scale domains was designed to better understand the mechanism behind this domain guiding 3D graphene growth.

6.2 Future work

In our study of growing graphene with $FeCl_3$ and glucose, we suspected that the high defect density is resulted from an excess of carbon, compared with the metal catalyst, in samples. Hence, if we intend to continue this study and test our assumptions, samples should be prepared at lower carbon concentrations, and the results are to be compared with the previous findings.

In the second study, it was also brought up that the defects detected and measured by the D peak in Raman spectra may be resulted from the presence of large quantities of nano-sized domains. It was also inferred that the reaction may have suffered an under-coverage of carbon. To solve the under-coverage issue, more carbon can be added in the preparation step by increasing the concentration of the PAN solution. It may also be possible to alter the nano-sized domain structure by improving the surface conditions of Cu. For example, a chemical washing or a pre-heat of the copper particles may result in cleaner particle surfaces with larger-sized domains.

Also, there was no conclusion made upon the influence of different heat treatment conditions on the products' properties or qualities because the evidence was not sufficient. Therefore, an extended temperature range should be investigated to see its effect on graphene growth. That may also help us to better understand the growing mechanism behind it.

Besides, graphene synthesised with Cu has exhibited a well-ordered structure, indicating that Cu is a good candidate for the role of the metal catalyst in 3D graphene fabrication. The salts of copper should also be investigated. Just as the $FeCl_3$ used in our first study, if the copper salt can be sufficiently reduced to copper during the reaction, it may also be a good catalyst candidate.